LABORATORY EXPERIMENTS INVESTIGATING ENTRAINMENT BY DEBRIS FLOWS

A THESIS

SUBMITTED TO THE FACULTY OF THE UNIVERSITY OF MINNESOTA BY:

DELANEY MOBERLY

IN PARTIAL FULFILLMENT OF THE REQUIRMENTS FOR THE DEGREE OF MASTERS OF SCIENCE

UNDER THE SUPERVISION OF PROFESSOR KIMBERLY HILL

NOVEMBER, 2015

Acknowledgements

I must gratefully acknowledge my advisor, Kimberly Hill, for her knowledge, assistance, guidance, and encouragement throughout this process. I am also grateful for the input from my committee members. I want to thank my husband, David, for his support and love, as well as my parents and family. This thesis would not have been possible without all of you.

Table of Contents

List of Tables iv

List of Figures v

Chapter 1: Introduction and Background 1

I. Previous Laboratory Experiments 3

II. Previous Field Studies 6

III. Previous Models 8

Chapter 2: Experimental Methods 12

I. Introduction 12

II. Experimental Setup 12

II A. Debris Flow Flume 12

II B. Particles 15

II C. Instrumentation 15

III. Experimental Procedures 16

III A. Preparation for Reproducibility 16

III B. Run Procedure 18

IV. Experimental Conditions 20

V. Entrainment Mechanisms 24

Chapter 3: Digital Image Analysis of the Flow and Entrainment Processes 25

I. Raw Data Processing 25

II. Eulerian Fields and Issues of Spatial/Temporal Resolution 28

III. General Behavior of Flow 29

IV. Entrainment 34

V. Top of Flowing Layer 39
VI. Dense vs Full Flowing Layer 41
Chapter 4: Experimental Results: Entrainment Rate and Associated Mechanisms 44
I. Net Erosion 44
II. Variability 45
III. General Entrainment Results 46
III A. Angle Dependence and Bead Size 47
III B. Volume/Breadth Dependence 49
III C. Aspect Ratio Dependence 52
III D. Initial Position Dependence 54
IV. Representative Cases 58
V. Shear Stress 59
VI. Velocity Fluctuations 62
VII. Discussion 70
VII A. Boundary Conditions 70
VII B. Shear Stress 71
VII C. Granular Temperature 73
Chapter 5: Summary and Outlook 78
Bibliography 81
Appendix 85
I. Definition of Symbols 85

List of Tables

Table 1: Location of Sensors and High-Speed Camera 14
Table 2: Properties of Zirconium Silicate Particles as provided by Quackenbush 15
Table 3: Summary of Angle of Inclination Experiments 22
Table 4: Summary of Aspect Ratio Experiments 23
Table 5: Relevant Parameters for Experiments Performed for this Thesis for Comparison with Results Described by Farin et al. (2014) and Mangeney et al. (2010) 23
Table 6: Summary of Experimental Conditions for Four Representative Cases 58

List of Figures

Figure 1: Experimental Setup for Farin et al. (2014) and Mangeney et al. (2010)..... 4
Figure 2: Experimental Setup for Egashira et al. (2001) Flume Experiments..... 5
Figure 3: Schematic of Debris Flow Velocity Profiles from Iverson 2012. 10
Figure 4: Sketch of Debris Flow Flume..... 14
Figure 5: Example Setup of Experimental Flume..... 16
Figure 7: Close Up of Experimental Setup with Grid Paper for Unit Conversion. 20
Figure 8: Raw Data Processing..... 26
Figure 9: Spatial Resolution Testing..... 29
Figure 10: Example Debris Flow Experiment at IP1..... 30
Figure 11:Solid Fraction and Horizontal Velocity versus Vertical Distance, 1 Second into the Experiment..... 30
Figure 12: Solid Fraction at 0.5, 1, 2 Seconds into the Experiment 31
Figure 13: Horizontal and Vertical Velocity Profile at 0.5, 1, 2 seconds into the Flow... 31
Figure 14: Horizontal, Vertical, and Cross Correlated Velocity Fluctuation Profiles at 0.5, 1, 2 Seconds into the Flow..... 32
Figure 15: Granular Temperature and Reynolds Stress Profile at 0.5, 1, 2 Seconds into the Flow. 33
Figure 16: Linear-log Plot of the Horizontal Velocity Data and the Natural Logarithmic Fit at 1 Second into the Flow. 36
Figure 17: Relating the Bottom of Flowing Layer with the Top of the Flowing Layer.. . 36
Figure 18: Normalized Entrainment Height 37
Figure 19: Various Time Averages for Entrainment Rate. 38
Figure 20: Solid Fraction versus Vertical Distance 1 Second into the Flow. 40
Figure 21: Exponential Fit and Linear Fit of Solid Fraction Profile..... 41
Figure 22: Comparison of the Dense and Full Flowing Layers of Time after Start of Flow.. 43
Figure 23: Average Granular Temperature and Average Reynolds Shear Stress over Time. 43

Figure 24: Instantaneous Entrainment Rate and Net Erosion for Experiments at IP1 with 0.8 mm Particles..... 45
Figure 25: Variabilty In Experiments - Normalized Depth of Entrainment, and Entrainment Rate over Time after Front Arrival. 46
Figure 26: Normalized Depth of Entrainment, and Entrainment Rate over Time after Front Arrival for Experiments with 0.8 mm Particles.. 48
Figure 27: Normalized Depth of Entrainment, and Entrainment Rate over Time after Front Arrival for Experiments with 2 mm Particles.. 48
Figure 28: Normalized Depth of Entrainment, and Entrainment Rate over Time after Front Arrival for Experiments with Different Particle Sizes 49
Figure 29: Normalized Depth of Entrainment, and Entrainment Rate over Time after Front Arrival for Experiments with Aspect Ratios of 0.27..... 50
Figure 30: Normalized Depth of Entrainment, and Entrainment Rate over Time after Front Arrive for Experiments with Aspect Ratios of 0.30..... 51
Figure 31: Normalized Depth of Entrainment, and Entrainment Rate over Time after Front Arrival for Experiments with Aspect Ratios of 0.45..... 51
Figure 32: Normalized Depth of Entrainment, and Entrainment Rate over Time after Front Arrival for Experiments with Aspect Ratios of 0.50..... 52
Figure 33: Normalized Depth of Entrainment, and Entrainment Rate over Time after Front Arrival for Experiments with Volume/Breadth Ratios of 0.021. 53
Figure 34: Normalized Depth of Entrainment, and Entrainment Rate over Time after Front Arrival for Experiments with Volume/Breadth Ratios of 0.028 53
Figure 35: Normalized Depth of Entrainment, and Entrainment Rate over Time after Front Arrival for Experiments with Volume/Breadth Ratios of 0.034. 54
Figure 36: Normalized Depth of Entrainment, and Entrainment Rate over Time after Front Arrival for Experiments with Initial Positions 1 and 2 55
Figure 37: Mangeney et al. (2010) Entrainment Depth as a Function of Time after Front Arrival Measured at x=0.90m. 56
Figure 38: Farin et al. (2014) Entrainment Depth and Velocity Profiles at Different Points along the Debris Flow Flume for the Case of θ=23°, V/B=0.028 m^2, and A_r=0.30. 57

Figure 39: Entrainment Rate as a Function of Time after Start of Flow for Four Representative Cases 59
Figure 40: Shear Stress versus Time after Front Arrival for Representative Cases. 60
Figure 41: Normalized Depth of Entrainment versus Shear Stress, Entrainment Rate for Representative Cases. 60
Figure 42: Entrainment Rate versus Average Shear Stress over the First Half-Second of the Denser Flow. 61
Figure 43: Granular temperature and Reynolds stress as they Vary with Time after the Front Arrival. 62
Figure 44: Parametric Plots of Entrainment Rate versus Average Granular Temperature and Average Reynolds Stress..... 63
Figure 45: Normalized Entrainment Depth, Entrainment Rate, Average Granular Temperature, over Time after Front Arrival for Various Length Scales 64
Figure 46: Thickness of Dense Flowing Layer in Terms of Number of Bead Diameters from Time after Front Arrival..... 65
Figure 47: Normalized Entrainment Depth over Time after Front Arrival, Entrainment Rate, Average Granular Temperature over Time of Decreasing Entrainment Rate for various Length Scales, and Entrainment Rate versus Average Granular Tempearture for various Length Scales over Time of Decreasing Entrainment Rate for Case 1..... 66
Figure 48: Normalized Entrainment Depth over Time after Front Arrival, Entrainment Rate, Average Granular Temperature over Time of Decreasing Entrainment Rate for various Length Scales, and Entrainment Rate versus Average Granular Tempearture for various Length Scales over Time of Decreasing Entrainment Rate for Case 2..... 67
Figure 49: Normalized Entrainment Depth over Time after Front Arrival, Entrainment Rate, Average Granular Temperature over Time of Decreasing Entrainment Rate for various Length Scales, and Entrainment Rate versus Average Granular Tempearture for various Length Scales over Time of Decreasing Entrainment Rate for Case 3..... 68
Figure 50: Normalized Entrainment Depth over Time after Front Arrival, Entrainment Rate, Average Granular Temperature over Time of Decreasing Entrainment Rate for

various Length Scales, and Entrainment Rate versus Average Granular Tempearture for various Length Scales over Time of Decreasing Entrainment Rate for Case 4..... 69
Figure 51: Calculated and Measured Entrainment Rate versus Average Granular Temperaturefor Case 1 Averaged over Several Bead Diameters 75
Figure 52: Calculated and Measured Entrainment Rate versus Average Granular Temperaturefor Case 2 Averaged over Several Bead Diameters 75
Figure 53: Calculated and Measured Entrainment Rate versus Average Granular Temperaturefor Case 3 Averaged over Several Bead Diameters 76
Figure 54: Calculated and Measured Entrainment Rate versus Average Granular Temperaturefor Case 4 Averaged over Several Bead Diameters 76

Chapter 1: Introduction and Background

Debris flows are rapid gravity-driven events involving mixtures of boulders, gravel, sand, fine particles, and water (e.g., Iverson, 1997; Takahashi, 2007) that present a well-known hazard in mountainous areas around the world. They can cause disruptions and damage to property as well as loss of life (Hungr et al., 2005; Hussin et al., 2012). Debris flows are initiated on high slopes, where they can form when water meets fragmented rock, or rock and sediment is destabilized by other means and begins to flow down the mountain, entraining more mass as they go (Berger et al., 2011; Iverson, 1997; Iverson et al., 2011; Mangeney, 2011; McCoy et al., 2012, 2013). Debris flows have the ability to increase from the original mobilized mass by factors of 10-50 times by volume due to entrainment (Hussin et al., 2012). For example, the 1990 Tsing Shan debris flow in Hong Kong began as a relatively small slip of 400 m^3 and enlarged to 20,000 m^3 by entraining colluvium from the bed in its path (King, 1996, as cited by Hungr et al., 2005). These flows have the ability to destroy everything in their path (Takagi et al., 2011), making them a phenomenon of particular interest for hazard planning and mitigation efforts. There is evidence that the frequency of debris flows and hazards associated with them are increasing in association with changes in macro and micro climate and in land use, resulting in modification in rainfall patterns and changes in local sediment supply (e.g., Pierce et al., 2004; Stoffel and Beniston, 2006; Jomelli et al., 2009; Floris et al., 2010; Jakob and Friele, 2010). Thus, there is an increasing need for models that can mechanistically account for the manner in which physical parameters give rise to certain debris flow behaviors.

Debris flows are composed of water, rock and soil, the exact details of which evolve as a debris flow travels downslope. The general behavior of debris flows is somewhere in between that of debris floods – where high water discharges carry large volumes of sediment and fluid shear stresses play a dominant role in the dynamics -- and dry avalanches – where particle-particle interactions dominate the dynamics (McCoy et al., 2012) As debris flows travel down steep slopes, they can scour down to the bedrock and

entrain material in their way (Hungr et al., 2005; Yohannes et al., 2012). Much of the erosion occurs at the front or snout of the flow (Berger et al., 2011; Iverson et al., 2011). The flowing mass transfers its momentum and kinetic energy to the static bed below (Mangeney et al., 2010), and in doing so, increases the momentum and speed of the bed material. Entrainment is suspected to play a major part in the dynamics of debris flows; not only does the debris flow add momentum to bed material, but, depending on the nature of the flow and the conditions surrounding it, the entrainment of material can either increase or decrease flow velocity and extent of deposition (Mangeney, 2011). With a better understanding of the mechanics of debris flows, tools to more accurately predict the size and impact of debris flows can be developed for the safety of people, property, and ecosystems.

Due to the destructive nature of debris flows, it can be difficult to measure the mechanics of a full scale flow (Berger et al., 2011; McCoy et al., 2013; Farin et al., 2014). A variety of approaches have been taken to overcome this obstacle (Iverson and Vallance 2001; and Rickenmann et al., 2003). Some have instrumented debris flow channels in the field (e.g. Berger et al., 2011; Hürlimann et al., 2003; McCoy et al., 2012 & 2013). Iverson et al. (2011) have performed large-scale debris flows under controlled conditions in a large-scale outdoor flume. Others have conducted a variety of experiments at the laboratory scale to examine the mechanics of debris flows and related granular flows (e.g. (Capart and Young, 1998; Fraccarollo and Capart, 2002; Mangeney et al., 2010; Takagi et al., 2011; Yohannes et al., 2012; Farin et al., 2014).

Despite all of the work done so far, there is still a need for a deeper understanding of the mechanics behind debris flows. Entrainment, in particular, is an area of interest that has grown significantly. Entrainment is the process by which the loose material in the path of a debris flow is picked up and becomes a part of the flow (Iverson et al. 2011; Farin et al. 2014). This increase in the mass of the flow can play a major role in defining the magnitude of a debris flow (Mangeney et al. 2010; McCoy et al. 2012). As such, it has been the subject of much interest in the scientific community. Currently, there is no consensus on the mechanics behind entrainment in debris flow settings.

As evidenced by the many different theories about entrainment rates, there are a number of common factors that influence entrainment, including the angle of inclination (Bouchaud et al., 1994; Tai and Kuo, 2008; Mangeney et al., 2010), which is associated with increasing erosion at higher slopes. Pore pressures (Berger et al., 2011; Iverson et al., 2011) are important in their effect on the internal stresses of the flow. The water content in the debris flow supply and bed plays a large role in the rate and depth of entrainment (Mangeney et al. 2010; Berger et al. 2011; Iverson et al. 2011). Shear stresses on the bed also have been proposed to affect entrainment rates in a number of different ways (Capart and Young, 1998; Fraccarollo and Capart, 2002; Iverson, 2012).

In this chapter, we briefly review recent research performed to understand entrainment behaviors in the laboratory and in the field.

I. Previous Laboratory Experiments

Laboratory-scale experiments allow the most systematic variation of parameters such as particle size, boundary roughness, and debris flow volume. Additionally, they allow for more detailed measurements of dynamics such as flow velocities, boundary stresses and concentrations. While the scaled down size leads to difficulties, particularly with multi-phase flows of water and particles, the ability to control and manipulate variables such as water content, size of particles, or the angle at which the experiment is performed can help build a model framework for understanding the larger scale effects, as many recent experiments have shown.

Farin et al. (2014) and Mangeney et al. (2010) performed laboratory experiments to investigate the influence of entrainment on mobility (flow speed and momentum) of debris flows via the run-out distances. They performed experiments in a 3 m long flume with Plexiglas walls at two different spacings: 10 cm or 20 cm apart. The base of the channel was roughened by gluing a layer of the particles used in the experiment to the base. A reservoir of particles, which contains particles for bed preparation or the debris flow supply (depending on the stage of the experiment), could be released from rest at the

upper end of the channel. They performed experiments over two different types of beds: erodible beds and non-erodible beds. The experiments over erodible beds are of most relevance to the work we describe here. To prepare the erodible, these authors used the method proposed by Pouliquen (1999). Specifically, they release a mass of particles from the reservoir and allow it to reach a steady state thickness after the particles stop moving. In this case, the thickness of the erodible bed arises naturally from the internal rheology of dense flows, and, in particular, the thickness of the erodible bed is a function of the angle of inclination. The set-up is pictured in Figure 1 below. The particles used were primarily glass, with a diameter, d, of 0.6 - 0.8 mm, bulk density, ρ, of 2.5 kg/L, angle of repose, θ_R, of 23° ±0.5°, and avalanche angle, θ_L, of 25° ±0.5°.

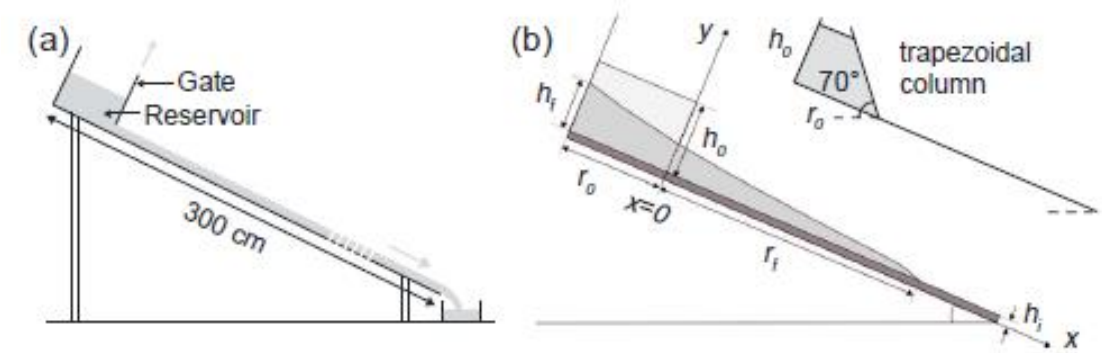

Figure 1: Experimental setup for Farin et al. (2014) and Mangeney et al. (2010) Distance downstream of the gate opening was x, r_o and h_o refer to the length and height of the supply respectively, h_f was the height of the flow, and h_i was the initial bed thickness.

Once they had prepared the bed, they prepared an additional mass of particles in the reservoir, released the particles onto the erodible bed, measured details of the entrainment and other dynamics during the flow, and then measured the runout after the flow had stopped. They reported primarily on dynamics during the flow and details of the run-out. During the flow, they also saw that different distinct phases exist: first a spreading phase with high velocities followed by a slower thinner flow in a propagation phase. They found details of the run-out were closely related to the boundary conditions of the supply

as well as entrainment during the flow, but they did not report on details of the entrainment process itself.

Egashira et al. (2001) used a slightly different set-up to study the effect of sediment size on entrainment (see Figure 2 below). Specifically, they performed experiments in a 12 m long, 10 cm wide flume with an erodible bed on a downstream section only. They prepared their erodible bed in two sections: (1) an upstream "equilibrium bed" and (2) the primary downstream erodible bed. The first part was prepared with a surface slope equal to the equilibrium slope, defined by Egashira et al. (2001) according to the angle at which no net erosion occurs. The second part was prepared so that its surface angle of inclination is the same as that in the flume. They used a 10 cm "stopper" to separate the "equilibrium bed" from the downstream section of erodible bed, which has the same surface slope as the experimental flume. Their primary concern was the effect on the erosion of the bed due to changing the particle size of the flow relative to that of the bed. They reported measurements of the net erosion only (not instantaneous erosion rates). They found that increasing particle size of the flow relative to the particle size in the bed could increase erosion rate.

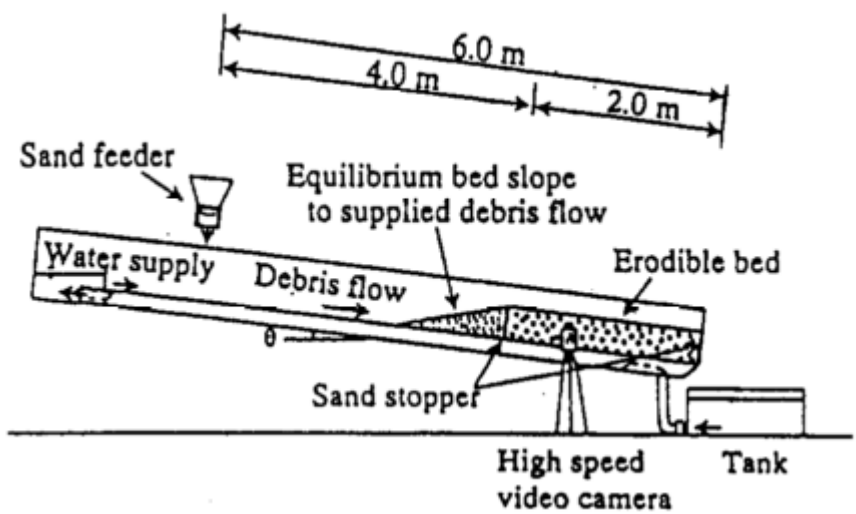

Figure 2: Experimental setup for Egashira et al. (2001) flume experiments

Papa et al., (2004) investigated the influence of bed sediment size on erosion rate in saturated debris flows on a similar experimental flume. They found that if both bed and flow particles were of the same size distribution, erosion rates monotonically increased with increasing particle size.

We note the so-called equilibrium slope discussed by Egashira et al. (2001) is also referred to in the literature as a “neutral angle,” or the angle to which a debris flow will naturally return after significant perturbation such as a shearing flow. If the bed is at an angle higher than the neutral angle, a debris flow will entrain material until the slope reaches the neutral angle; if the bed is at the neutral angle, a debris flow will be neither net erosional or net depositional, and if the bed is at an angle less than the neutral angle, a debris flow will deposit material until the slope is at the neutral angle.

Laboratory experiments are limited by issues of scale and materials best-suited to simulate debris flows. For example, Takagi et al (2011) found that the shape of particles used is important to shallow granular flows such as laboratory-scale debris flow experiments. Iverson (1997) discussed the importance of scaling considerations particularly in the context of particle-fluid flows, where scaling is of particular concern. To minimize such scaling issues, some have performed full-scale experiments (e.g., Iverson et al. 2012) and some have performed measurements of real debris flows in the field.

II. Previous Field Studies

Both laboratory experiments and field scale studies provide valuable insight to the overall behavior and detailed mechanics behind debris flows. Full scale events provide opportunities to measure basal forces, pore pressures, entrainment rates, and other qualities with real debris materials and a platform to test the viability of theories under large-scale conditions typical of real debris flows.

Recent monitoring stations have been built around active debris flow sites such as Acquabona Creek in the Dolomites in the Italian Eastern Alps (Berti et al., 1999),

Illgraben channel in the Swiss Alps (Berger et al, 2011), and Chalk Cliffs study basin in the Sawatch Range, Colorado, USA (McCoy et al., 2012). These have provided relevant field data for this problem. Berti et al. (2000) used flow height sensors, load cells, and fluid pore pressure sensors buried in the channel bed. They found that by entraining particles, the debris flow progressively increased in solid concentration of the flow. Additionally, their data indicated that the scour rate was proportional to local slope gradient. Berger et al. (2011) found that entrainment rate increased with average and fluctuating stresses and demonstrated that the fluctuations and entrainment rate was particularly well-correlated with the highly fluctuating granular front. However, data obtained by McCoy et al. (2012) are not in agreement with these measurements. A more in-depth look at what might bring about these differences is warranted.

Other field studies focused on the importance of fluid content in the debris flow and bed in entrainment rates. For example, McCoy et al. (2012) saw that the entrainment rates appeared to change once the underlying surface was wet, and hypothesized that the rate of infiltration was a rate limiting process for debris flows with a dry bed based on their instrumentation of Chalk Cliffs in Colorado. Iverson et al. (2011) found evidence of a positive feedback loop, where wet bed experiments had higher pore pressures that led to more scour at the base, which resulted in lower basal friction, which would further encourage scour. Conversely, Iverson et al. (2012) found that experiments with lower volumetric water contents in the bed had lower pore pressures, less basal scour and material entrained, and much smaller momentum gains. Mangeney (2011) discussed some of the general conclusions one can draw from these field studies. In particular, her investigations supported Iverson et al's (2011 & 2012) conclusions that suggested that a higher water content in the bed would increase entrainment and speed, so long as the water content was high enough.

Iverson et al. (2011) proposed that when the bed material had a higher water content, the flow momentum would grow and that the flow momentum would decrease at lower water content. By estimating the local forces affecting momentum in the system, they observed that momentum from the flowing layer was transferred to the erodible bed, but the

momentum of the flowing layer also increased as basal friction was reduced to almost nothing in the case of wetter bed sediments. Pore pressures in wet bed sediments rapidly increased as the debris flow front arrived to liquefy the bed.

Full scale studies such as these are particularly useful for effects that are difficult to capture in the laboratory. However, they are plagued with issues such as reproducibility and control over experimental parameters. In this thesis, we focus on dynamics in dry granular flows, so we do not review these effects associated with different concentrations in detail. Instead we focus on the detailed measurements we can make in the laboratory and their implications for flows in the field. Since variable fluid effects have been shown to be significant, it is likely that our results are most applicable for conditions where fluid content is unchanging. We consider some existing hypotheses for entrainment rate in this light.

III. Previous Models

There are a number of different ideas about how entrainment happens and what physical laws govern it. For example, Capart and Young (1998) believe that the velocity of the interface between moving and stationary particles (or entrainment rate $\dot{e}$) relative to the material is proportional to the difference between the instantaneous particle flux and the equilibrium flux of particles under steady, uniform conditions. This is related to a capacity-limited view of a debris flow, which relies on the assumption that the debris flow grows until it reaches some equilibrium condition. In Capart and Young (1998), the expectation was that there was some neutral particle flux for a given set of boundary conditions at which there is no net flux of material from debris flow. When the system is below capacity, the instantaneous flux will be greater than the neutral flux, resulting in the entrainment of particles.

Others support this proposal that the entrainment rate should depend on the condition of the bed. For example, Egashira et al. (2001) described a neutral angle to which a bed of particles returned after being disturbed. They saw how this neutral angle could govern the

net (or total) erosion of a bed over which a debris flow moved. Bouchaud et al. (1994) and Tai and Kuo (2008) proposed a similar framework, though they proposed that the entrainment rate is proportional to the difference between the angle of inclination and the angle of *repose* of the material. The difference is subtle, as the angle of repose can refer to a range of angles between the maximum angle of stability and a minimal angle of relaxation. Still, the ideas are similar. In either case, if the entrainment rate, $\dot{e}$, depends on the difference between the instantaneous angle of inclination of a bed, θ, and the neutral angle, θ_n, (or angle of repose), one could write:

$$\dot{e} \sim \theta - \theta_n \qquad 1$$

The framework of an entrainment rate depending on the angle of repose is similar to the idea of an excess shear stress governing entrainment rates. As the difference between the angle of inclination and angle of repose increases, the shear stresses in the system and the entrainment rate also increase. Tai and Kuo (2008) proposed a framework based on these parameters and suggested that entrainment rate should be linearly proportional to the product of the thickness of the flowing layer and the sine of the difference in the two angles. They reasoned that a thicker flowing layer would cause more shear stress at the interface between flowing and stationary particles and theoretically bring more particles into motion.

Fraccarollo and Capart (2002) asserted that there is a “mechanical link” between the shear stress in the bed and the entrainment rate, but it is more complicated than a simple expression of excess shear stress implies. They suggested that two sets of dynamics are important in setting the shear rate: (1) they suggested the entrainment rate is proportional to the jump in shear stress across the interface of motion, and (2) they suggested that the entrainment rate depended inversely on the increased momentum of the bed material as it is entrained into the flow. Iverson (2012) had a similar model framework, in which the entrainment rate depended on the excess boundary shear stresses (see equation 2), as well as the basal flow velocity, or, using variables pictured in Figure 3.

$$\dot{e} = E = \frac{\tau_{1_{bot}} - \tau_{2_{top}}}{\rho(v_{1_{bot}} - v_{2_{top}})} \qquad 2$$

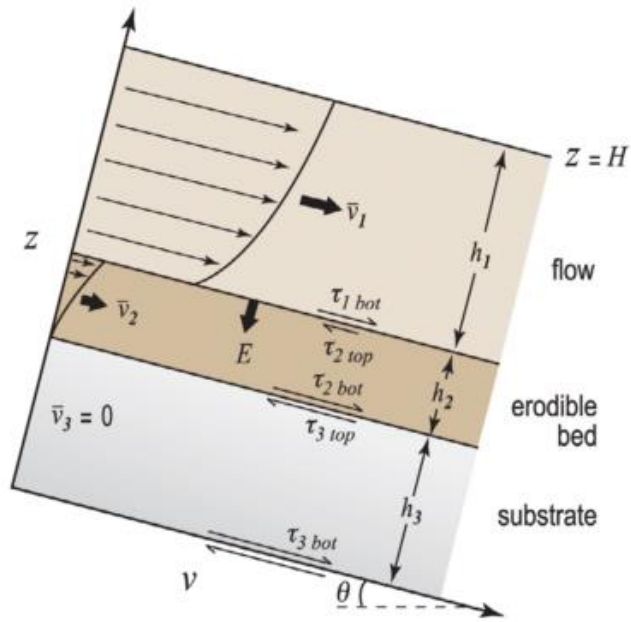

*Figure 3: Schematic of debris flow velocity profiles from Iverson 2012. The top layer is the flowing layer, with velocity profile and associated average velocity, $\overline{v_1}$, the middle layer is the erodible bed, with velocity profile and associated average velocity $\overline{v_2}$, and the bottom layer is the substrate, with average velocity $\overline{v_3}$=0. The rate at which the interface between the two layers moves is the entrainment rate, indicated by **E** in this image, and called $\dot{e}$ in this text. Shear rates between the various layers are indicated by τ and the appropriate subscripts.*

In this expression, the velocities and shear stresses refer to those just above (subscript, "1_{bot}") and just below (subscript, "2_{top}") the interface between the flow and the quasi-static erodible bed.

To summarize this brief introduction, throughout the literature, several researchers have provided evidence and theory that support several different controls on erosion rates associated with debris flows. Historically, these have included external controls such as particle size and boundary conditions to underlying controls such as stress and velocity fluctuations in the flow. As described in this thesis, we are investigating entrainment by debris flows and the associated mechanisms behind it using laboratory scale experiments and high-speed video. We developed a method to analyze the high-speed video and use it to measure entrainment with sub-particle accuracy as well as to provide other quantities proposed to be associated with entrainment such as shear stress, granular temperature,

and Reynolds stress. We use this information to characterize the debris flow in general and to investigate possible relationships between entrainment rate and quantities such as shear stress or granular temperature. The boundary conditions for some experiments are similar to those in the work by Mangeney et al. (2010) and Farin et al. (2014). As such, we also compare the experimental setups and associated data.

The rest of the thesis is arranged as follows: In Chapter 2 we review the experimental setup used, a comparable set of experiments, the experimental procedures and a summary of the experiments performed. In Chapter 3 we explain the digital analysis methods used to analyze the various experiments. Chapter 4 details the observed results within our data, and how our results compare with other published results. Finally, Chapter 5 discusses and summarizes the findings.

Chapter 2: Experimental Methods

I. Introduction

For this project, we used a laboratory scale flume to simulate debris flows in a controlled environment. This flume allows for a reservoir of particles to be released over a rigid bed and then to flow over an erodible section whose surface is inclined at the same angle as that of the rigid bed surface. We recorded the flow using high-speed, high-resolution video and analyze dynamics associated with entrainment using programs written for MATLAB. This chapter reviews the experimental methods and procedures used. Analysis of data is covered in the following chapter.

II. Experimental Setup

II A. Debris Flow Flume

The experimental setup consisted of a 3 m long flume with Plexiglas walls spaced 7.6 cm apart. We considered the flume sufficiently narrow that the nature of the dynamics is pseudo 2-dimensional. That is, the particles traveled primarily in one direction (the *x-direction*, as in Figure 4), and entrainment happened normal to this direction (in the *y-direction*). For this description, we considered x=0 to be the far upstream point of the flume.

The bed of our experimental flume consists of two main sections. Approximately one half of the bed (x = 0 to x = 1.83 m) is a rigid, non-erodible bed. The second part (from x = 1.83 m to x = 3m) has a false bottom that can be removed to reveal a deeper cavern. For all the experiments performed in this thesis, we filled the cavern with particles to create an erodible bed with loose bed materials whose surface was initially at the same height and angle as the surface of the non-erodible bed. Also, for all the experiments performed in this thesis, an initially static supply of particles is released from one of two positions at

the upstream end of the bed and allowed to flow first down the rigid bed and then over the erodible bed.

There were two points of potential release of the supply, which we called *IP1* and *IP2* (short for "initial positions 1 and 2"). In both cases, the positioning of the supply was facilitated by hinged gates. At the upstream end, a hinged gate was placed at x=0.36 m to create a space to store the supply of particles for a debris flow prior to the release. A second hinged gate was placed at x=1.83 m to allow for a secondary release point for a debris flow. This is referred to as initial position two, or *IP2*.

To increase bed-particle shearing and reduce slipping, we installed sandpaper on the bottom of the rigid bed section from x = 0.61 to x = 1.83 m (indicated as L_{rough} in Figure 4). The sandpaper was CAMI grit size 36, which has an average particle diameter of 0.53 mm. Immediately downstream of the rigid bed (x=1.83 m), the base of the flume drops down by 7.62 cm at a 90 degree angle to allow for the creation of an erodible bed. Since we filled this erodible section to the surface of the non-erodible bed for all experiments, throughout this thesis we refer to this initial bed height as H_b (≅7.6cm) We refer to the length of the erodible section as $L_{erodible}$ (≅1.2m). The erodible section ends with a wall at x≅3m, and the flow exits the flume through a rectangular opening with cross-sectional area equal to that over the non-erodible bed.

The flume may be inclined from 0 to 45 degrees. To facilitate this, the flume was attached to a hinge on the downstream end, and a long pole on the upstream end. We raised the flume with the help of a pulley system, and we measured the angle of inclination with a digital level with a precision of ± 0.2 degrees. A sketch of the flume is shown in Figure 4.

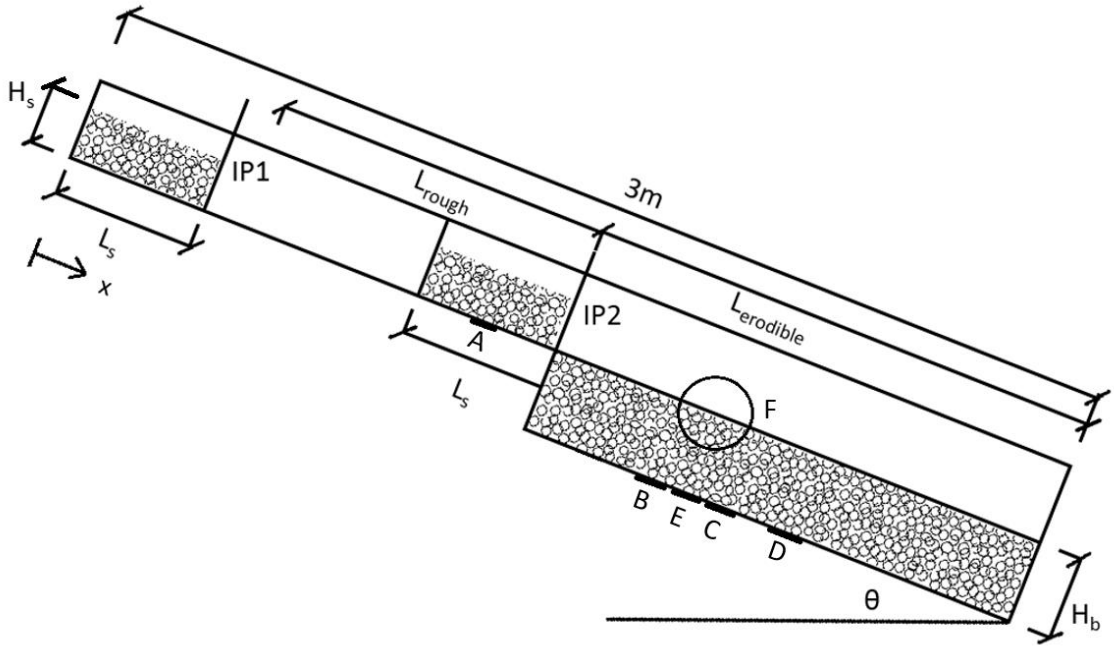

Figure 4: Sketch of debris flow flume. IP1 and IP2 refer to release points for the supply of a debris flow. H_s and L_s are the height and length, respectively, of the debris flow supply, and H_b is the initial height of the erodible bed. All dimensions are given in the text and in Table 1.

As indicated in Figure 4, the flume was also outfitted with a number of sensors to allow for the measurement of basal fluid pressure and basal forces. Four basal fluid pore pressure sensors were placed along the center of the flume at points A-D, locations given in Table 1. These were used primarily in the case of experiments involving fluid. A basal force plate was placed at E. The high-speed camera recorded in the area indicated by the circle at F. It should be noted that, for each experiment the exact location of the high-speed camera changed, but it remained centered near x = 2.23 m.

Table 1: Location of Sensors and High-Speed Camera

	A	B	C	D	E	F
measuring device	pore pressure	pore pressure	pore pressure	pore pressure	basal force plate	high-speed camera
x [m]	1.58	2.04	2.29	2.44	2.23	2.23

II B. Particles

We used spherical particles to model the material in the debris flow. This simplification is common in laboratory scale debris flow research (Yohannes et al 2012, Mangeney et al. 2010, Farin et al. 2013). Zirconium silicate particles were chosen for their opaque color (which allowed for particle tracking) as well as for their density. A summary of the zirconium bead properties is given below in Table 2. Bulk and material densities were provided by the manufacturer, Quackenbush Co., Inc, for type QBZ-58A zirconium silicate. The coefficient of restitution for these particles was 0.91.

Table 2: Properties of Zirconium Silicate Particles as provided by Quackenbush

	2 mm Diameter	0.8 mm Diameter
Bulk Density* [kg/m^3]	2460	2410
Material Density [kg/m^3]	4100	4100
Color [ ]	White	Blue

*This quantity depends on the preparation of the sample and was provided by the manufacturer. For the 2mm particles, the number indicates a solid fraction = 0.60, and for the 0.8 mm particles, the number indicates a solid fraction = 0.59. We consider the difference between the 2mm and 0.8mm beads given by the manufacturer negligible.

II C. Instrumentation

For the results discussed here, we used a high-speed camera video (with resolution up to 1024 x 1024 at a frame rate of 1000 frames per second). In addition to the high speed camera, a series of sensors were attached to the flume, as mentioned in the previous section. The four sensors shown in Figure 5 measure the basal fluid pressure in the rigid and erodible sections of the flume. A basal force plate was also added to measure the normal force on the bottom of the erodible bed, as seen in Figure 5. In order to relate time information from the sensors and video, the pore pressure sensors were electronically linked with the high-speed camera. This connection allowed us to remotely trigger the camera using the software for the pore pressure sensors. The timing of the basal force plate was related to that of the pore pressure sensors by making a distinct tap on the side of the flume prior to each experiment.

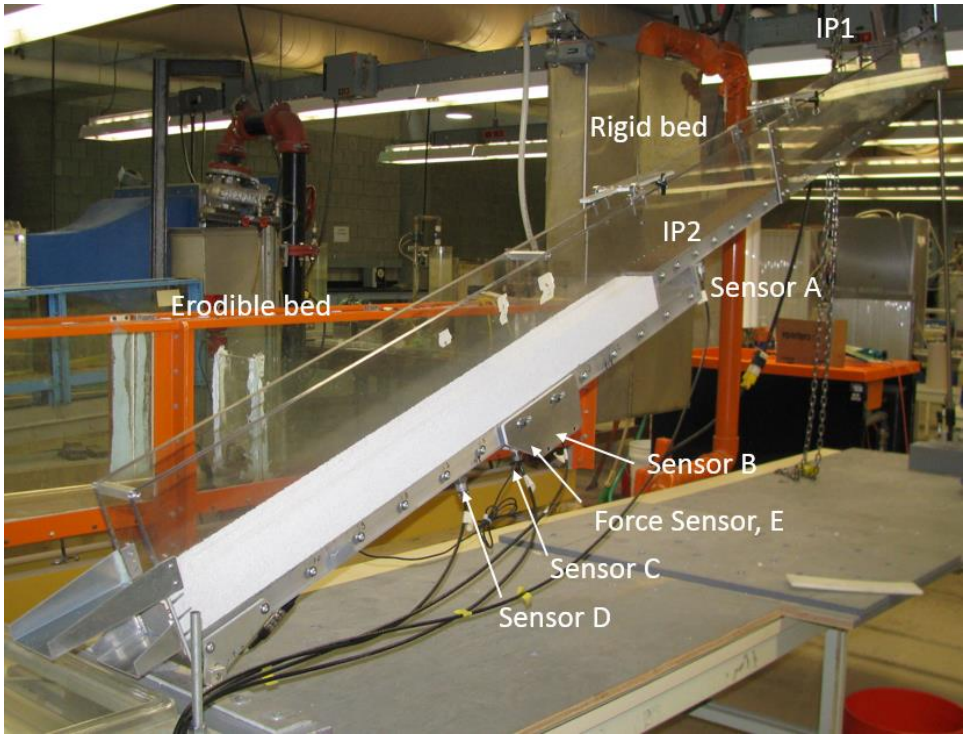

Figure 5: Example Setup of Experimental Flume

A digital level with accuracy of ±0.2^{o} was used to measure the angle of inclination of the flume. A digital scale with accuracy of ±0.05 grams was used to measure the amount of particles in the erodible section, mass of the debris flow supply, and the total mass exiting the flume from each debris flow experiment. The ambient air temperature and humidity was measured using a digital thermometer and hydrometer.

III. Experimental Procedures

III A. Preparation for Reproducibility

Before each experiment, we prepared the apparatus and the beads in such a way as to maximize reproducibility. Static electricity, variations in humidity, and bed aging were three issues in particular that we tried to minimize. The walls of the flume had a tendency to build up static electricity over time. To prevent this, we wiped down the sides of the flume with anti-static spray before each experiment. In the work done by Hill et al., 2013 it was found that the level of humidity had a large effect on the particles. When the

ambient humidity was lower, an experiment at a given angle would be more erosive than an otherwise identical run on a significantly more humid day. Therefore, we tried to minimize variations in humidity. In particular, in the cooler months of the year, when the humidity decreased, we used a humidifier to increase moisture in the air. Since the ambient humidity also affected remnant moisture on the particles, we placed particles in open containers next to the flume adjacent to the humidifier overnight to allow for absorption of the moisture. Another problem related to preparing an experiment discussed in the work by Hill et al. (2013) was bed "aging." After a run, it is common that not all of the material in the erodible bed will be eroded. If they simply recharged the bed, or added the particles needed to refill the erodible, and then ran another experiment, they saw that for each successive run with the same erodible bed the experiment would become more and more erosive, as seen below in Figure 6. However, when the entire bed is reset – that is, removed, or reworked in some way after each experiment – the total mass out does not vary with an increased number of experiments. As such, we reworked the bed after each experiment to prevent this aging effect.

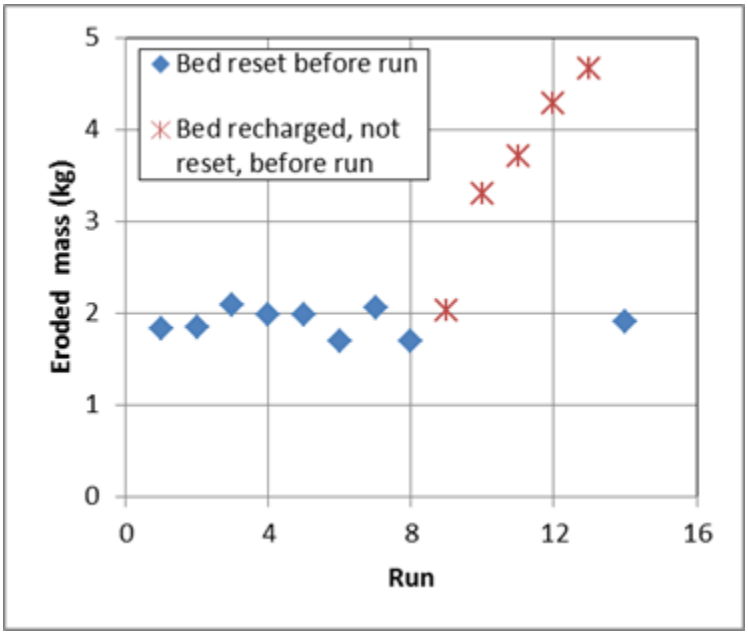

Figure 6: Bed Aging Results from Hill et al. (2013). "Bed" refers to the erodible bed. As described in the text, "recharged" refers to the refilling of the bed to the height H_b after an experiment and "reset" refers to a remixing of the bed materials.

III B. Run Procedure

Each run had four main phases of preparation: preparing the erodible bed, setting up the supply, adjusting the high-speed camera, and running the experiment. Once we sprayed the flume with anti-static spray and performed the other previously-mentioned steps to ensure reproducibility, the following steps were taken:

1) Erodible Bed Preparation
    a. Weigh particles for erodible bed using digital scale
    b. Pour particles into erodible bed
    c. Smooth surface of erodible bed with plastic scraper
    d. Place container at base of flume to catch effluent flow
2) Supply Preparation
    a. Weigh particle supply using digital scale
    b. Close gate and add particles to supply reservoir.

    c. Raise flume to desired angle of inclination as measured by digital level

3) High-Speed Camera Preparation
    a. Attach grid paper
    b. Turn off all lights other than high intensity spotlight
    c. Orient camera so flume appears horizontal, particles are sufficiently large to track, and the frame of the image is low enough to capture full depth of motion within the erodible bed
    d. Adjust spotlight to illuminate particles without any glare in the image
    e. Take snapshot of flume with grid paper
    f. Remove grid paper
4) Experimental Performance
    a. Remove pin holding gate in place
    b. Turn on pore pressure and basal force sensors
    c. Tap the side of the flume
    d. Release gate and supply of debris flow
    e. Begin recording with high-speed camera once the supply is in the camera viewing window.

We temporarily attached a piece of grid paper to the flume in the view of the camera to allow for a conversion between pixels and meters. We would take a snapshot of this grid, as seen in Figure 7, and then remove it prior to performing the experiment. The purpose of step 4c was to provide a distinct point that we could use to link the timing between the basal force plate and the pore pressures sensors.

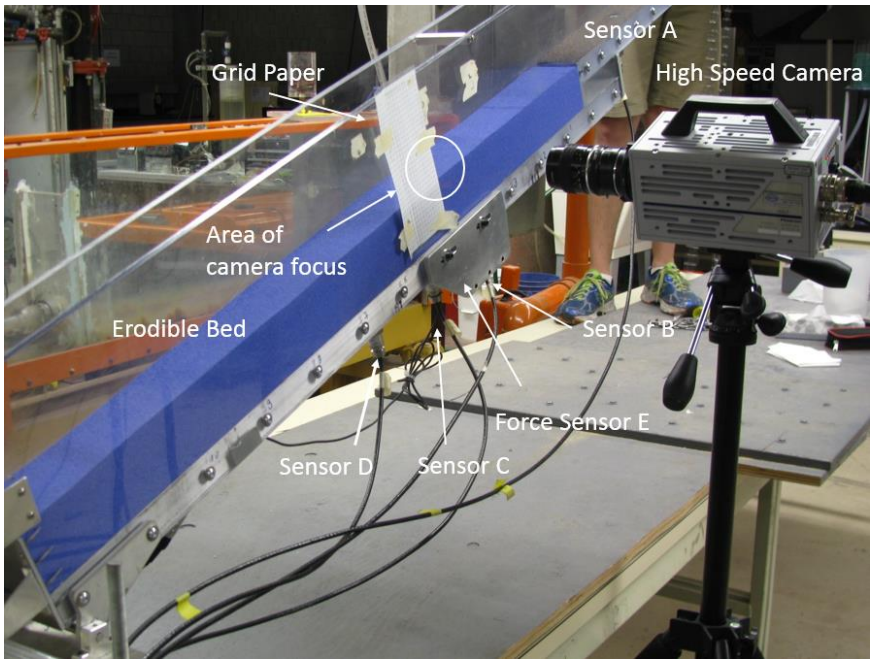

Figure 7: Close up of experimental setup with grid paper for unit conversion.

After the debris flow was complete, we turned off the basal force sensor. The pore pressure sensors and high-speed camera recorded for a pre-set amount of time. Then we would block the outlet from the flume to prevent any extraneous material from exiting due to other movements around the flume. We would then return the flume to the horizontal position and weigh and record the effluent mass. Appropriate masses for the supply and erodible bed would be returned to those sections to prepare for the next experiment.

IV. Experimental Conditions

We performed two sets of experiments to help us develop a mechanistic understanding of three primary sets of external conditions that influence the net entrainment and the entrainment rates in these experiments. These external controls were: (1) angle of inclination (relative to a “neutral angle”, e.g., Equation. 1); (2) the configuration of the supply; (3) the initial position of the supply relative to the erodible bed.

For the first set of experiments, summarized in Table 3, we focused on varying the angle of inclination of the bed for both bead sizes. The angles were determined by first performing some preliminary experiments to find the neutral angle, θ_n: about 23° for 2 mm particles and 23.5^o for 0.8 mm particles. We then chose angles that were greater and less than θ_n to examine the range of entrainment rate behavior. Otherwise, care was taken to prepare the bed and supply the same way from one run to the next. For these experiments, the particles were released from initial position one, *IP1*, to most closely resemble the effect of a thin layer of particles flowing over an erodible bed, similar to debris flows in the field. We were not concerned with the effect of varying the aspect ratio of the supply for the experiment group, since experiments were performed at *IP1* and we assumed that regardless of the initial configuration, the supply would become a thin layer of flowing particles before reaching the erodible bed.

For the second set of experiments, summarized in Table 4, we focused on understanding the effect of the initial preparation of the debris flow supply (with boundary conditions similar to Mangeney et al., 2010 and Farin et al., 2014), as well as the initial position of the supply relative to the erodible bed. In particular, we systematically varied the aspect ratio, A_r, or ratio of the height, H_s, to length, L_s, of supply (Figure 4) while keeping the volume per breadth of the supply, V/B [m^2], constant and varied V/B while keeping A_r constant. Volume was found using the following expression.

$$V = \frac{V_p}{1-\eta} = \frac{m_s/\rho_m}{1-\eta}, \qquad (3)$$

In this expression, $Vp = m_s/\rho_m$ was the volume of solid material of all particles in the supply [m^3], determined by weighing the particles put behind the gate for each experiment and dividing by materials density; m_s was the mass of the supply [kg], ρ_m [kg/m3] was the material density of the particles (table 2), and η was the porosity of the supply. As in Farin et al. (2014) and Mangeney et al. (2010) we approximate the porosity, η, by 0.375, similar to a random close-packed bed. We designed this second set of experiments to be comparable with those previously performed by Farin et al. (2014) and Mangeney et al. (2010) (Table 5). As such, we performed this set using primarily the

second position for the supply (*IP2*). This configuration is also helpful for comparing with related experiments in the granular physics community (e.g., Jop et al., 2007) where the flow speeds prior to initial erosion are negligible.

While these two sets of experiments were largely performed independently from one another, we also used a subset of each to understand the effect of the initial position of the supply on the outcome. Specifically, we performed two experiments where we only varied this initial position and held the rest of the variables constant (E2_27_34_1_I2 and E2_27_34_2_I1).

Table 3: Summary of Angle of Inclination Experiments

Experiment[1]	θ [°]	d [mm]	A_r [ ]	V/B [m^2]	IP [ ]
E1_2_21.5_I2	21.5	2	0.27	0.034	1
E1_2_22.0_I3	22.0	2	0.27	0.034	1
E1_2_22.5_I3	22.5	2	0.27	0.034	1
E1_2_23.0_I2	23.0	2	0.27	0.034	1
E1_2_23.5_I3	23.5	2	0.27	0.034	1
E1_2_24.0_I3	24.0	2	0.27	0.034	1
E1_0.8_22.5_I3	22.5	0.8	0.27	0.034	1
E1_0.8_23.0_I4	23.0	0.8	0.27	0.034	1
E1_0.8_23.5_I3	23.5	0.8	0.27	0.034	1
E1_0.8_24.0_I2	24.0	0.8	0.27	0.034	1
E1_0.8_24.5_I2	24.5	0.8	0.27	0.034	1

[1] Experiment name formatted as follows: E#_d_θ_I#, where E# refers to the "experiment group", d is the particle diameter in mm, θ is the angle of inclination in degrees, and I# indicated the number of duplicate experiments performed under those conditions

Table 4: Summary of Aspect Ratio Experiments[1]

Experiment[2]	*IP* [ ]	H_s [m]	L_s [m]	A_r [ ]	*V/B* [m^2]	θ [º]	*d* [mm]
E2_27_34_1_I2	1	0.095	0.353	0.27	0.034	23.5	0.8
E2_27_34_2_I1	2	0.095	0.353	0.27	0.034	23.5	0.8
E2_27_21_2_I1	2	0.081	0.298	0.27	0.021	23.5	0.8
E2_30_34_2_I2	2	0.101	0.335	0.30	0.034	23.5	0.8
E2_30_28_2_I1	2	0.092	0.305	0.30	0.028	23.5	0.8
E2_30_21_2_I1	2	0.085	0.283	0.30	0.021	23.5	0.8
E2_45_34_2_I1	2	0.123	0.274	0.45	0.034	23.5	0.8
E2_45_28_2_I1	2	0.104	0.231	0.45	0.028	23.5	0.8
E2_45_21_2_I1	2	0.112	0.249	0.45	0.021	23.5	0.8
E2_50_34_2_I1	2	0.130	0.260	0.50	0.034	23.5	0.8
E2_50_21_2_I1	2	0.110	0.219	0.50	0.021	23.5	0.8
E2_70_21_2_I1	2	0.130	0.185	0.70	0.021	23.5	0.8

[1] These experiments were performed in collaboration with Jared Mullenbach for his Undergraduate Research Opportunities Program (UROP) project.

[2]Experiment name formatted as follows: E#_A_r_V/B_I#, where E# refers to the "experiment group", A_r refers to the aspect ratio multiplied by 100, V/B refers to the volume per width in m^2 multiplied by 1000, and I# indicates the number of duplicate experiments performed under those conditions.

Table 5: Relevant parameters for experiments performed for this thesis for comparison with results described by Farin et al. (2014) and Mangeney et al. (2010)

Mangeney/Farin (f)				Moberly/Mullenbach (m)[1]				Comparison		
θ [º]	A_r [ ]	*V/B* [m^2]	H_b [m]	θ [º]	A_r [ ]	*V/B* [m^2]	H_b [m]	d_m/d_f [ ]	$V/B_m/V/B_f$ [ ]	ρ_m/ρ_f [ ]
25.4	0.70	0.028	0.005	23.5	0.27	0.034	0.076	1.14	1.214	1.64
22	0.70	0.028	0.005	23	0.30	0.028	0.049	1.14	1.000	1.64
23	0.30	0.028	0.049	23.5	0.45	0.034	0.076	1.14	1.214	1.64
23	0.30	0.028	0.049	23.5	0.50	0.034	0.076	1.14	1.214	1.64
				23.5	0.30	0.028	0.076	1.14	1.000	1.64
				23.5	0.45	0.021	0.076	1.14	0.750	1.64
				23.5	0.45	0.028	0.076	1.14	1.000	1.64
				23.5	0.45	0.034	0.076	1.14	1.214	1.64

[1] All cases for *IP2* gate unless otherwise indicated

V. Entrainment Mechanisms

While we recorded details like the net entrainment from the bed, the focus of this thesis is on the instantaneous entrainment of particles from the erodible bed. In particular, we were interested in the mechanics that govern this instantaneous entrainment that are relatively independent of angle of inclination, configuration of the supply, the initial supply position, and other external controls. Instead of external factors, these mechanisms are dependent on internal dynamics that arise naturally during the granular flow, for instance, the average stress associated with flow thickness and the stress associated with random kinetic energy such as what might be called “granular temperature” and “Reynolds stresses” associated with particle velocity fluctuation correlations.

To determine the instantaneous entrainment rate and potential governing parameters such as average stresses and granular temperatures, we developed methods of analyses built on results from particle tracking. We describe these and the associated dynamics in the next chapter.

Chapter 3: Digital Image Analysis of the Flow and Entrainment Processes

This chapter discusses the various digital analysis methods used to analyze the data collected. Once we had collected the data there were three main steps to analyzing that data: (1) processing the raw data into instantaneous velocities and positions, (2) processing the instantaneous velocities and positions into average Eulerian fields, and (3) using those average Eulerian fields to derive average quantities related to instantaneous entrainment and driving "forces" of entrainment. Here we describe the development of these techniques for the thesis. For the third step, we need to understand the Eulerian fields, such as velocity, velocity fluctuations, and densities, as they evolved throughout the experiments. Therefore, to describe the image analysis development, we also describe the kinematics of the flow and entrainment simultaneously in this chapter. In order to demonstrate the analysis methods, this chapter uses examples of experiments released from initial position one with aspect ratio of 0.27, volume/width of supply of 0.034 m^2 and all 0.8 mm particles (i.e. experiment E1_0.8_24.0_I2 in Table 3).

I. Raw Data Processing

Each experiment was filmed with a high-speed camera, typically with 30 pixels per particle, at 1000 frames per second. For the particle locating process, we used a MATLAB program published by the Georgetown Physics department (Blair and Dufresne, 2008), to filter each frame with a real-space bandpass filter to suppress pixel noise and locate all the particles based on the brightness of the particle (see Figure 8A). The location process occurs in two steps, first we find a rough location for each particle based on the local brightness maxima (Figure 8B). Then we take those initial locations as a rough guess to find a more exact location for the centroid of brightness of each particle (similar to a centroid of mass, but using the brightness of each pixel) (Figure 8C).

Once we used the Blair and Dufresne (2008) MATLAB macros to locate all particles in every image, we needed to track the particles from one image to the next, and then use this information for the dynamic variables involved in the entrainment process. For this we developed several MATLAB macros designed specifically for our application over the course of this master's degree work.

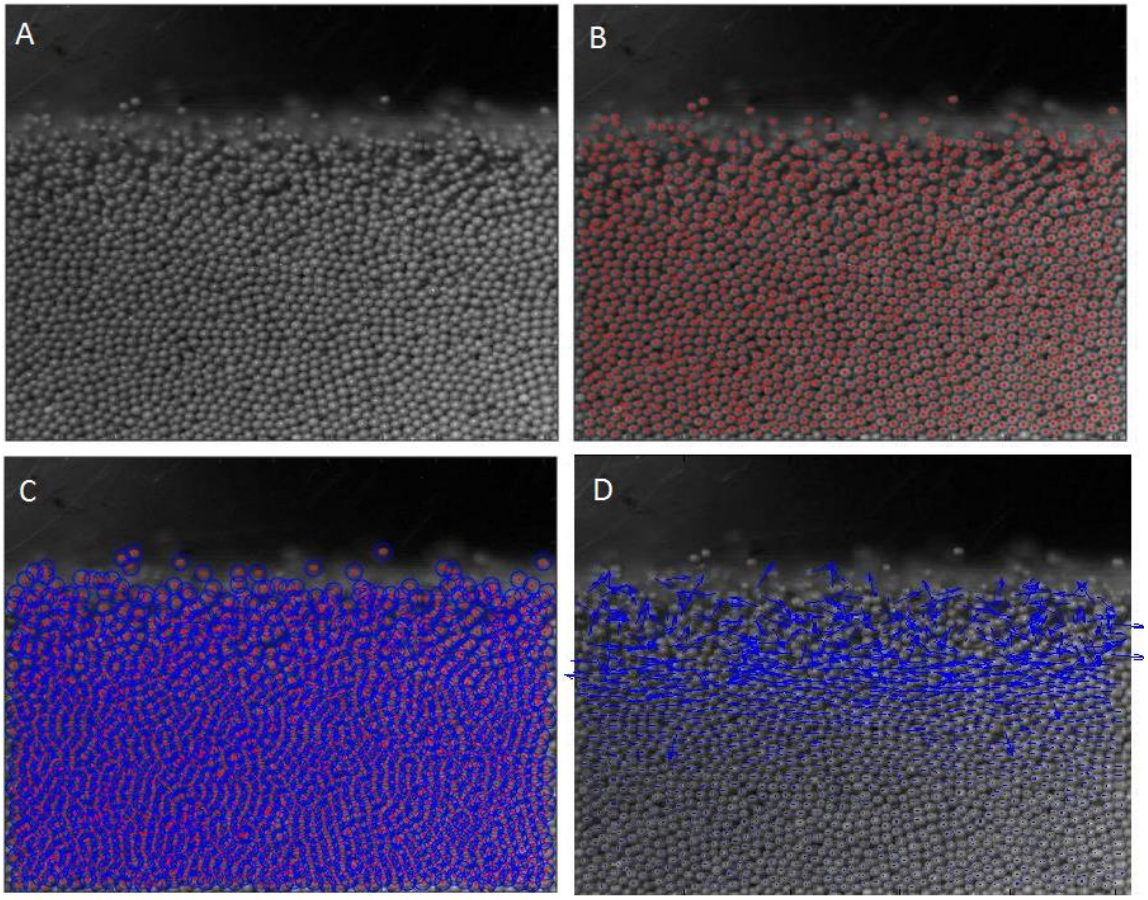

Figure 8: Raw Data Processing. A is the raw image at t=1s, B is the same image, with the initial particle locations (based on local maxima) indicated with red dots at the center of each located particle. C shows the final particle locations (based on centroid of brightness) indicated by the blue circles centered at the particle centers. D shows the instantaneous velocity vectors for each particle.

To track the particles from one image to the next, we developed a program that uses a distance minimization scheme with a user-defined maximum allowable distance for efficiency in the computational process. With these tracks, we are able to find the

horizontal and vertical displacement of each particle from each frame to the next (Figure 8D).

To obtain measures of average density, horizontal velocity, vertical velocity, and corresponding velocity fluctuations, we divided each image into horizontal bins such that we had a certain number of bins per particle diameter (e.g. 21 bins per particle). For each particle tracked over a user-specified time increment (e.g. 0.05 seconds), we found the bin associated with the center and determined the volume of particles within that bin as well as the horizontal and vertical velocity of said particle. We then calculated the volume and velocity for the other bins associated with that particle (e.g. if there are 21 bins per particle, there would be 10 bins above the center and 10 bins below to fill with the contribution from that particle). Once we repeated that process for all particles in the image, we found the average horizontal and vertical velocity for each bin. From there we could get the velocity fluctuations for each particle based on the difference between the instantaneous velocity and the average. Then we computed the average horizontal, vertical, and tangential velocity fluctuation for each bin, as well as the solid fraction, or the volume of particles per volume of bin. These calculations are similar to those performed for similar applications (e.g., Hill et al., 2003; Gioia et al., 2006) and are expressed below for horizontal velocity, *u*, solid fraction, *f*, Reynolds shear stress, τ_R, and Reynolds normal stress, σ_R, which we convert into a granular temperature in Equation 8.

$$\langle u(y)\rangle = \langle u\rangle_{By} = \sum_i \sum_b V_i^b u_i^b / \sum_i \sum_b V_i^b \tag{4}$$

$$\langle f(y)\rangle = \langle f\rangle_{By} = \sum_i \sum_b V_i^b u_i^b / 1024V \tag{5}$$

$$\tau_R(y) = \rho_m \overline{f u' v'}_{B_y} = \sum_i \sum_b V_i^b (u_i^b - \bar{u}_{B_y}) v_i^b / 1024V \tag{6}$$

$$\sigma_R(y) = \rho_m \overline{f v' v'}_{B_y} = \sum_i \sum_b V_i^b (v_i^b - \bar{v}_{B_y}) v_i^b / 1024V \tag{7}$$

$$T = \sigma_R(y) + \sigma_R(x) = \rho_m \times \left(\overline{f v' v'}_{B_y} + \overline{f u' u'}_{B_y}\right) = \rho_m \times \overline{f(v' v'_{B_y} + u' u'_{B_y})} =$$

$$\sum_i \sum_b V_i^b \left((v_i^b - \bar{v}_{B_y}) v_i^b + (u_i^b - \bar{u}_{B_y}) u_i^b\right) / 1024V \tag{8}$$

where the sum of i considered all images considered, the sum of b extends over all the particles in each image, u_i^b was the horizontal velocity of the bead *b*, v_i^b was the vertical velocity of bead *b*, and V_i^b was the volume of the portion of bead *b* within bin B_y, where *y* was defined as the center of bin B_y.

II. Eulerian Fields and Issues of Spatial/Temporal Resolution

Since our calculations for velocities and other quantities involved some averaging, it was important to verify that the results were not a function of the analysis, but were representative of what was actually occurring in the debris flows. In order to investigate the robustness of our analysis, a series of tests were performed on the spatial and temporal resolution of the data. Spatial resolution was tested by varying the number of horizontal segments each image was split into, which is defined by the number of bins per bead. The velocity fluctuations, horizontal and vertical velocity, and solid fraction at a given height in the image were found by taking an average over each of these horizontal segments.

As can be seen in Figure 9, the different spatial resolution did not make any significant changes to the results. A variation in number of bins per bead merely increased or decreased the number of data points, and did not affect the general trends or magnitude of the results. Based on these results, the resolution of 21 bins per bead was chosen to be used in all calculations thereafter. This was done since it gave enough detail without introducing excessive “noise” in the data.

A similar process was repeated for different temporal resolutions. In calculating the velocity fluctuations, horizontal and vertical velocity, and solid fraction, a temporal average was also taken over a series of frames. Temporal resolution was adjusted by varying the number of frames that these averages were taken over. Using the spatial resolution previously determined, the calculations were run averaging over 0.1, 0.05 and

0.01 seconds. As was seen in the spatial resolution testing, the various temporal resolutions did not affect the magnitudes or trends of the data. The temporal resolution of averaging over 0.05 seconds was chosen since it provided a fine enough resolution without being too “noisy”.

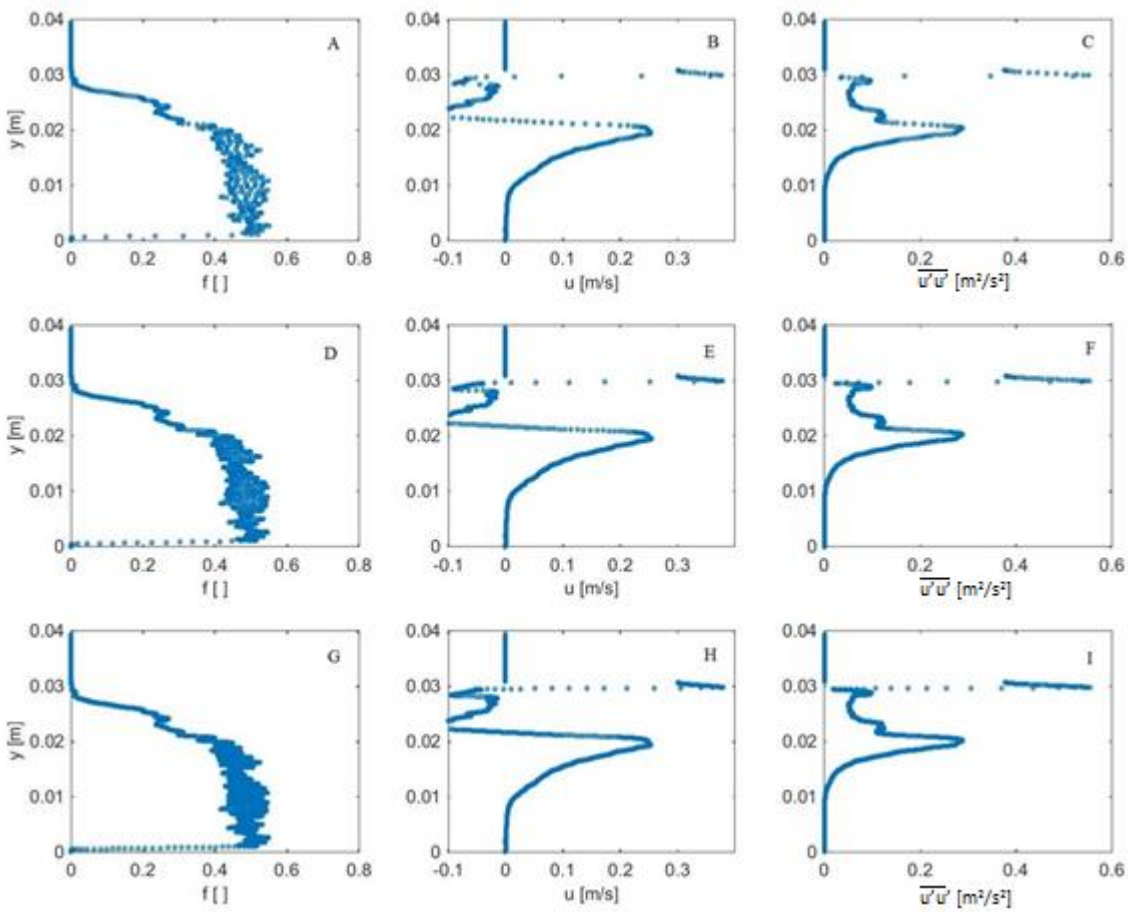

Figure 9: Spatial resolution testing. Solid fraction, f, horizontal velocity, u, and average horizontal velocity fluctuations $\overline{u'u'}$ at 11 bins per bead (A-C), 21 bins per bead (D-F), and 41 bins per bead (G-I). In the third column, $\overline{u'u'}$ refers to velocity fluctuations, such as those calculated in Equation 7.

III. General Behavior of Flow

The debris flows can be characterized based on a number of different attributes and how they vary spatially and temporally. In order to understand and characterize dynamics such

as entrainment, an understanding of the general progression of the flow behavior was first required. We see in Figure 10 an example experiment released from *IP1* progressing through time. Figure 11 demonstrates how the solid fraction and horizontal velocity change with respect to vertical distance y. The following series of figures illustrates the velocities, fluctuations, and other qualities at these same points.

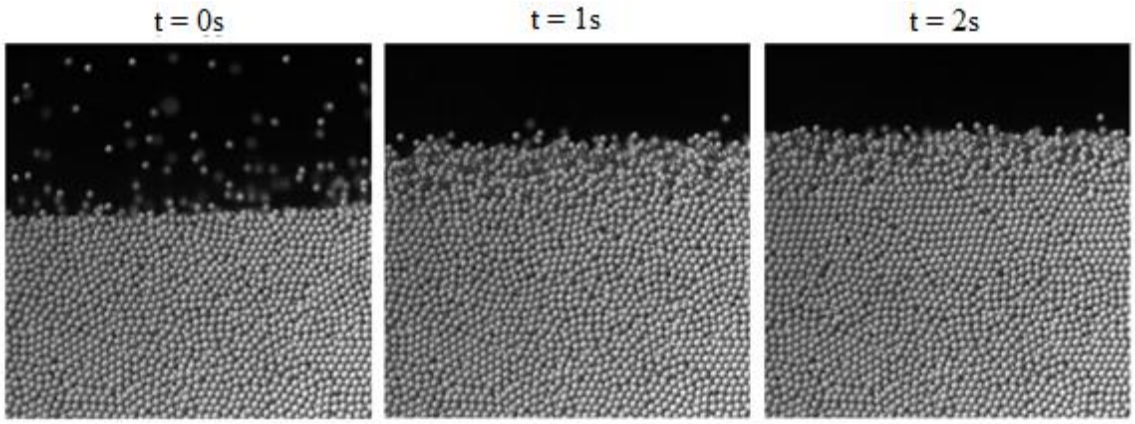

Figure 10: Example debris flow experiment at IP1, at 0, 1, and 2 seconds after recording begins. From experiment E1_0.8_24.0_I2 in Table 3

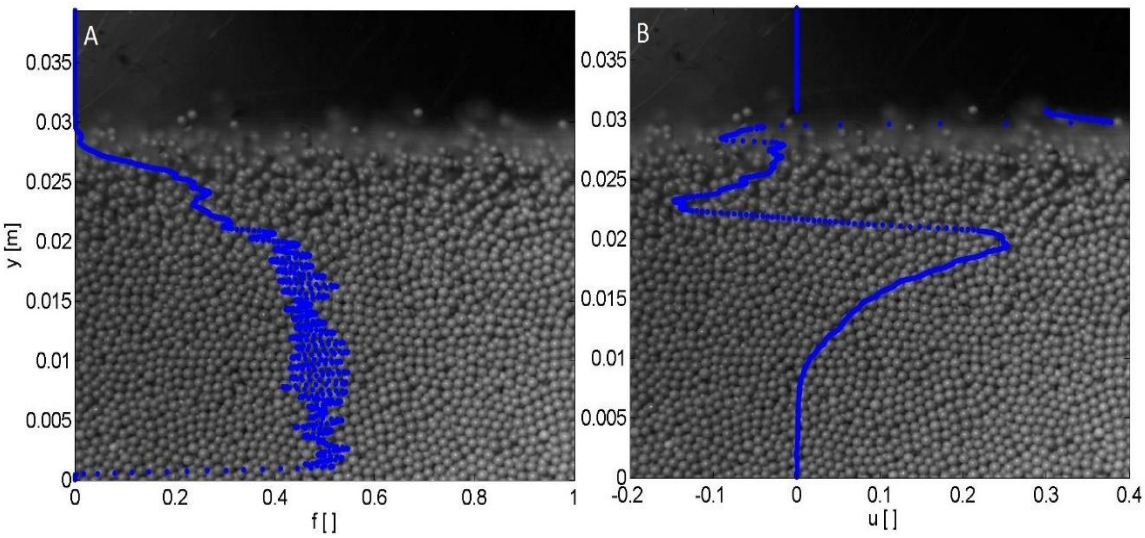

Figure 11:A solid fraction, f, versus vertical distance, y, and B horizontal velocity, u, versus y, 1 second into the experiment shown in Figure 10, E1_0.8_24.0_I2 in Table 3

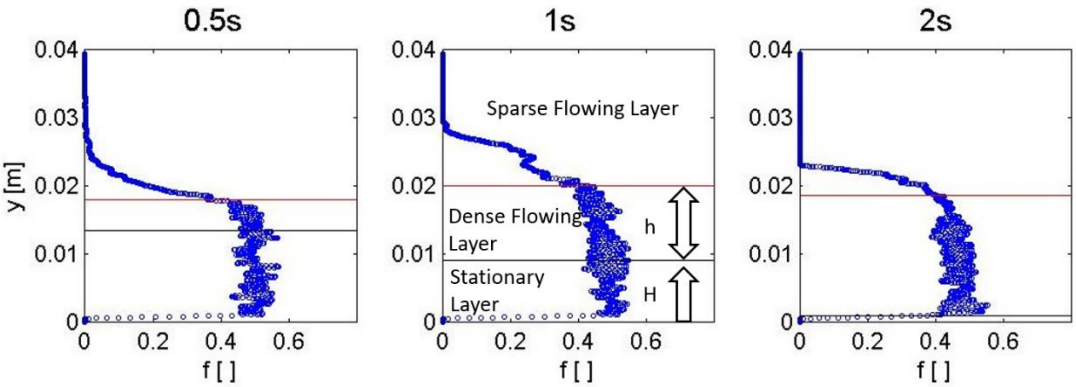

Figure 12: Solid fraction, f, at 0.5, 1, 2 seconds into the experiment shown in Figure 10, E1_0.8_24.0_I2 in Table 3. Upper red line indicates top of the dense flowing layer, lower black line indicates depth of entrainment at each time. At t=1s, we see the three layers of the debris flow, the sparse flowing layer, dense flowing layer, and stationary layer. The depth of entrainment, H, is shown measured from the bottom of the image, and the thickness of the dense flowing layer, h, is also shown.

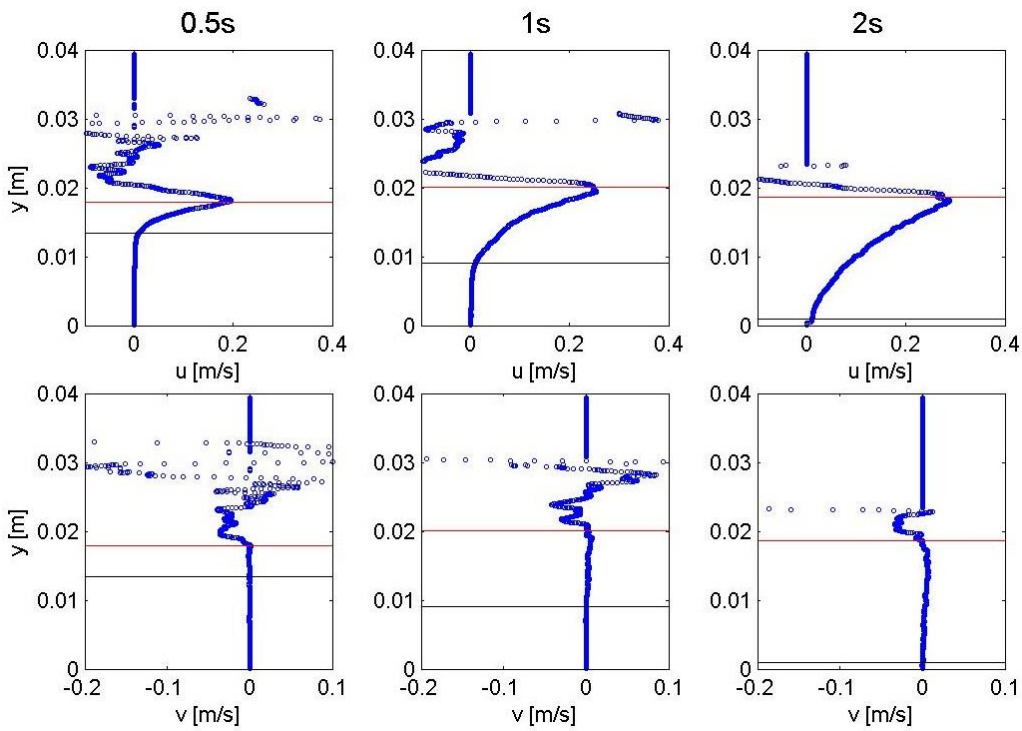

Figure 13: Horizontal, u, and vertical, v, velocity profile at 0.5, 1, 2 seconds into the flow. Upper red line indicates top of the dense flowing layer, lower black line indicates depth of entrainment at each time. Note positive velocities are defined as upwards for v, and in the direction of flow for u. The data are from the same shown in Figure 10, E1_0.8_24.0_I2 in Table 3.

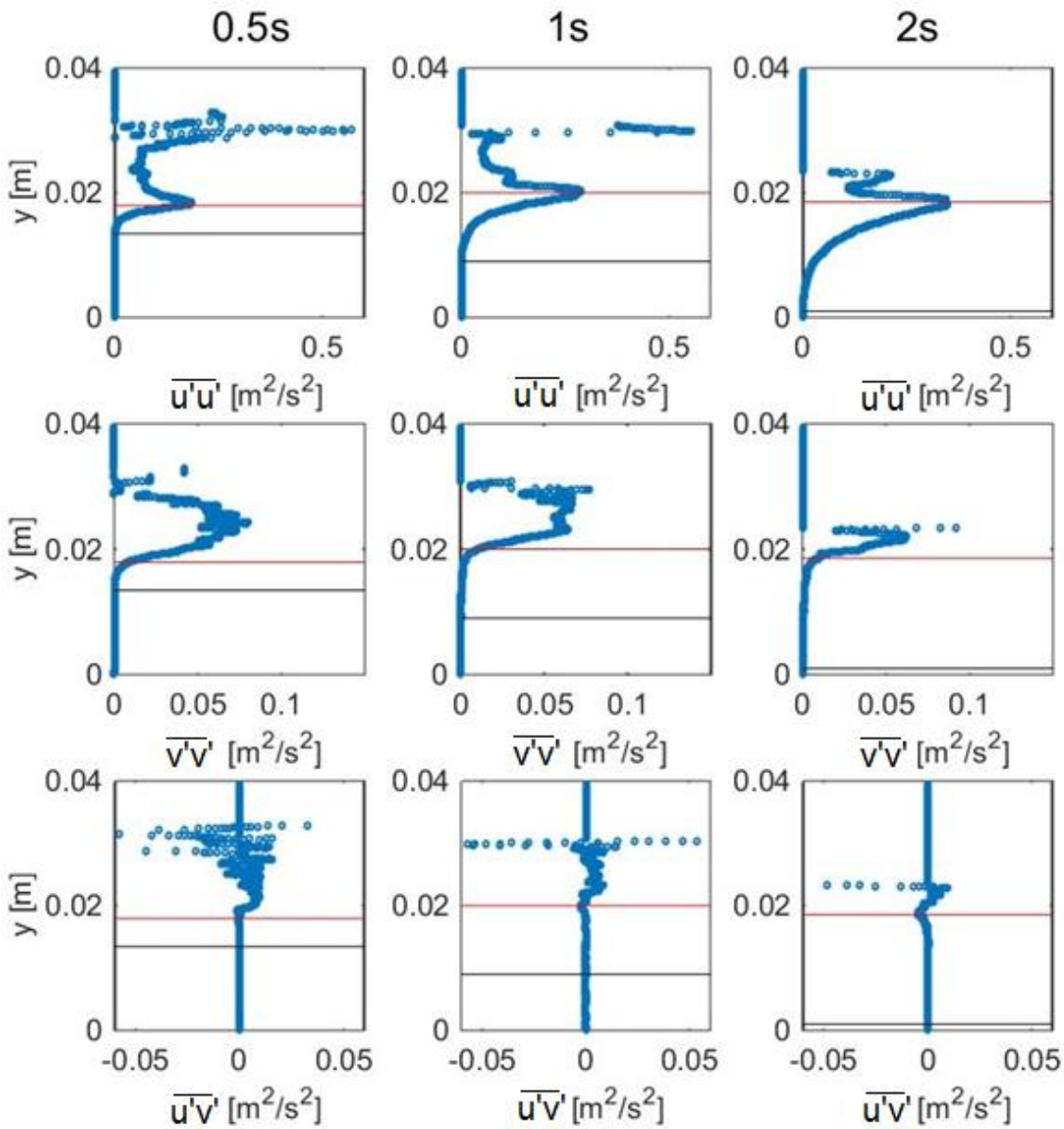

Figure 14: Horizontal, $\overline{u'u'}$, vertical, $\overline{v'v'}$, and cross correlated, $\overline{u'v'}$, velocity fluctuation profiles at 0.5, 1, 2 seconds into the flow. Upper red line indicates top of the dense flowing layer, lower black line indicates depth of entrainment at that time. The data are from the same shown in Figure 10, E1_0.8_24.0_I2 in Table 3.

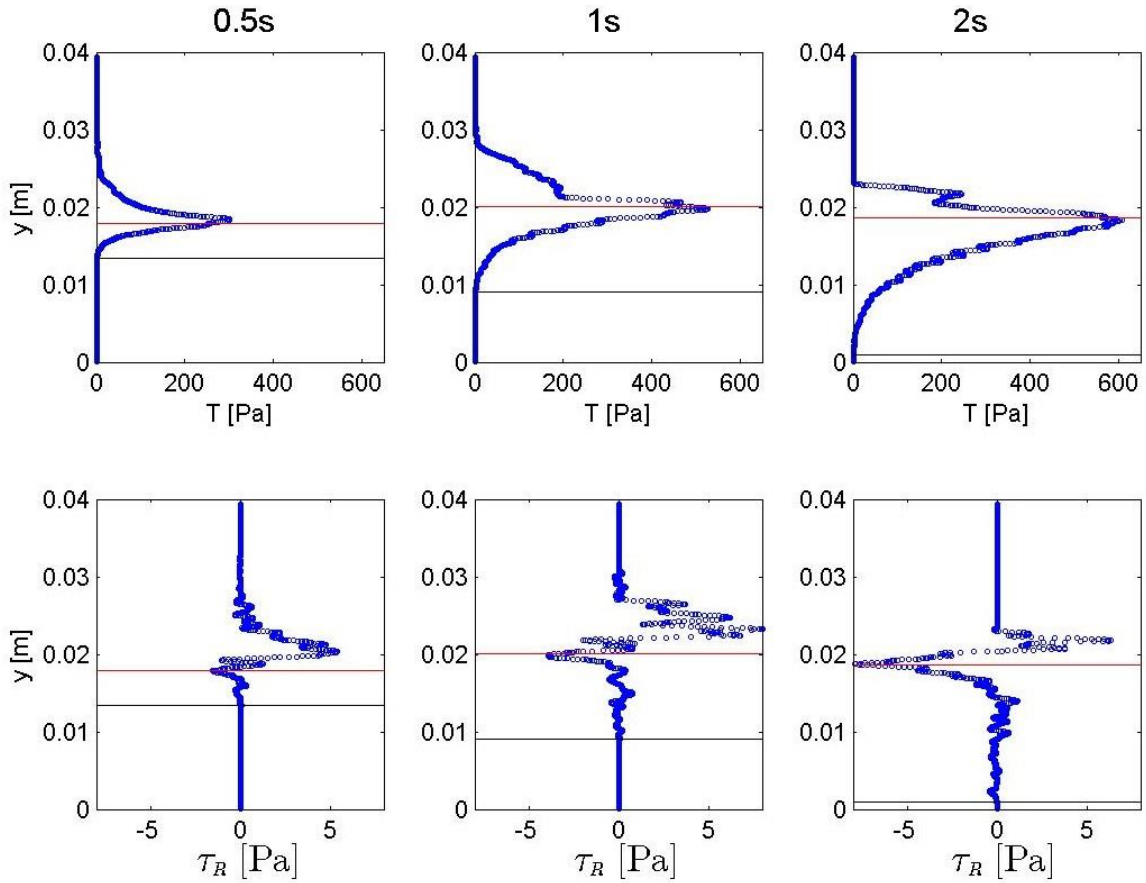

Figure 15: Granular temperature and Reynolds stress profile at 0.5, 1, 2 seconds into the flow. Upper red line indicates top of the dense flowing layer, lower black line indicates depth of entrainment at each time. The data are from the same shown in Figure 10, E1_0.8_24.0_I2 in Table 3.

As seen in Figure 12 through Figure 15, debris flows are not static with respect to time. In the early stages, the flow is very fast and chaotic, as seen with the increased velocity fluctuations at 0.5 seconds. Velocity profiles appear to have both fast moving and slower sections as well as particles moving upwards and in the opposite direction of the flow. The solid fraction at this time provides quantitative details for a more complete picture regarding these two regions. The sparse flowing layer (as indicated in Figure 12) has an almost negligible solid fraction, especially compared to the dense lower layer. This is where we have a sparse, chaotic flow, as the front of the debris flow is moving over the erodible bed. The top of the dense lower layer is indicated by the upper red horizontal

line. Details on how the top of this layer is determined are in Chapter 3, Section VI. Dense vs Full Flowing Layer. In the sparse flowing layer, we see that some particles have hit the erodible bed and are bounced up and sometimes backwards, as demonstrated with high velocity fluctuations. The erodible bed has begun to move, but only by a limited amount, as indicated by the lower black line in Figure 13 at 0.5 seconds. When the experiment begins, the supply of particles is released and the erodible bed is stationary. Experimental observations also indicate that, as the supply reaches the bed in experiments at initial position one, we see an initially sparse, energetic flow. Over the length of the rigid bed, the supply has spread out with a sparse front followed by a denser flowing layer.

As time progresses, significant erosion is seen in the bed and the horizontal velocity profile goes further and further down into the erodible bed (see lower black line in Figure 13). The solid fraction profile suggests this same conclusion, as the dense portion has increased in height and then decreased as a flow went over the bed, and, along with a portion of the bed, kept flowing. Velocity fluctuations above the denser flowing layer decrease, suggesting that the initially sparse energetic flow has become denser. The granular temperature and magnitude of the Reynolds stress also increase as the flow progresses.

IV. Entrainment

As the flow moves over the bed, there is a non-physical boundary between particles in motion and stationary particles, as indicated by the lower black line in Figure 12 through Figure 15. The rate change of this non-physical boundary with respect to time is the entrainment rate. In Figure 13, we can see that this interface moves down as the erodible bed is in motion at increasing depths as time progresses. To determine the entrainment rate, we first needed to determine the depth of motion at a given point in time. Other groups (Mangeney et al., 2007, Mangeney et al., 2010, Farin et al., 2014, Forterre and Pouliquen, 2008, Frey and Church, 2011) have shown that the horizontal velocity profile decreases exponentially near this interface of motion and no motion. By visual inspection

of the velocity profile, this exponential fit seemed to be reasonable based on our results, so we decided to model it as seen below.

$$y = m * ln(u) + b, \tag{9}$$

where y was the vertical position in the flow, measured from the bottom of the image u was the vertical velocity, and m and b were constants. Since the velocity profile has an exponential decay, finding where the velocity was exactly 0 would not be a reasonable representation of reality. Instead, we found at what height the velocity reached a critical level. We set this critical velocity as 0.01 m/s. The height was found by taking the natural logarithm of the velocity near critical velocity, and then using a least squares linear fit to solve for the constants m and b at each time step. In order to test how well this model fit the data, we plotted the fitted velocity and the data, as seen in Figure 16. The natural logarithmic fit was a good approximation of the data over the range of $-5 < \ln(u) < -3$. Since the natural logarithm of the critical velocity was -4.6052, this was determined to be a reliable method of determining the depth of entrainment. Figure 17 illustrates how this depth of flow relates to the rest of the flowing layer. The distance, h, is the thickness of the dense portion of the flowing layer. We can see that, in the dense portion of the flow, the horizontal velocity is monotonically increasing with y and following a fairly smooth profile. Above the dense portion, the solid fraction quickly drops off, and the horizontal velocity becomes much more sporadic. How the top of the flowing layer was determined is discussed with regards to the shear stress in Chapter 3, Section VI. Dense vs Full Flowing Layer.

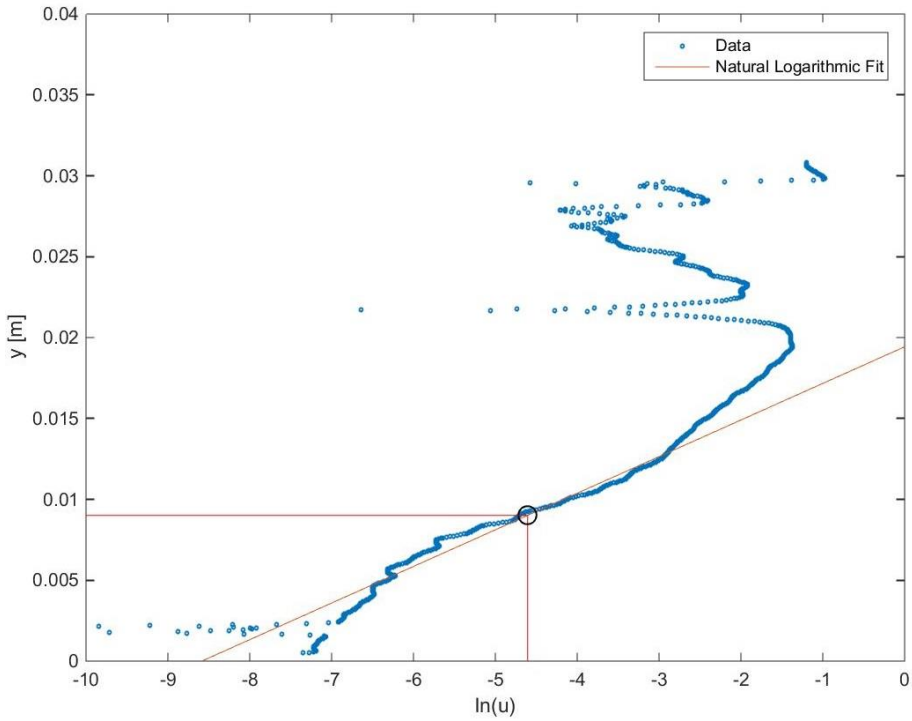

Figure 16: Linear-log plot of the horizontal velocity data and the natural logarithmic fit at 1 second into the flow. Lines indicate the location of the critical velocity

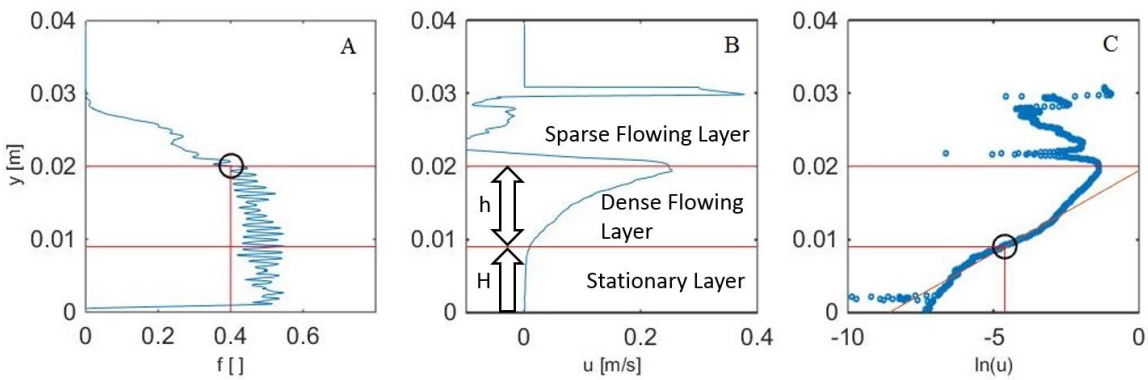

Figure 17: Relating the bottom of flowing layer with the top of the flowing layer. A is the solid fraction; f, profile; B is the horizontal velocity; u, profile; and C is a linear-log plot of the velocity data and the logarithmic fit. The top horizontal line is when f reaches a value of 0.4, and the bottom line is when u reaches the critical velocity 0.01 [m/s]. The three layers of flow are indicated in B, as well as the thickness of the dense flowing layer, h, and the depth of entrainment, H.

The entrainment rate is the rate of change of the entrainment depth with time. Using the natural logarithmic fit just described for the velocity, we found the height of entrainment at each time step as seen in Figure 18.

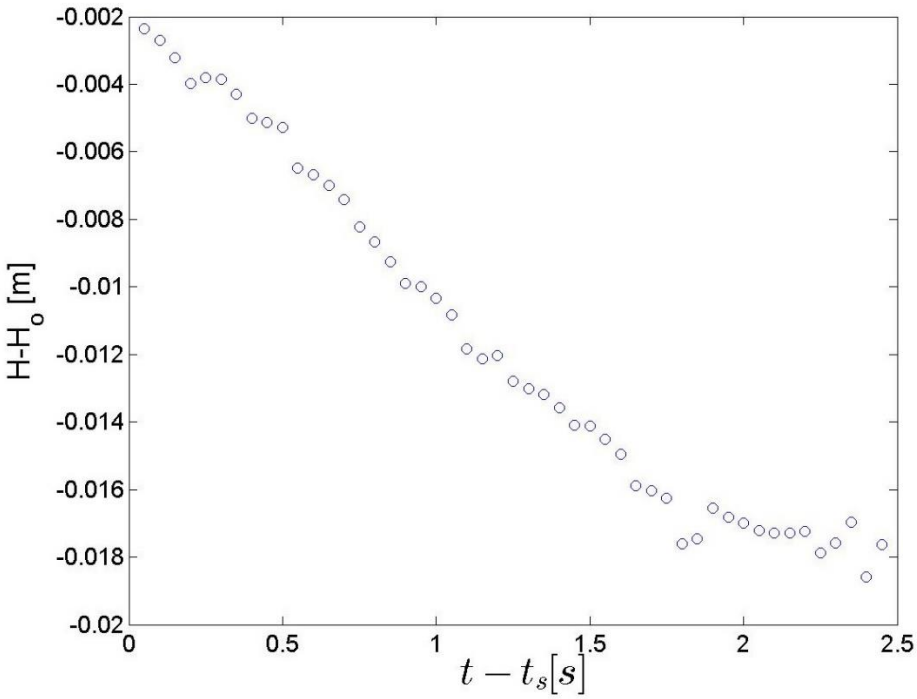

Figure 18: Normalized entrainment height, H-H$_o$, where H$_o$ is the initial depth, vs time after the start of the flow, t-t$_s$, for 0.8 mm beads at 24 degrees

From here, we found the slope of a linear fit over a user defined time step to find the rate of entrainment. It should be noted that entrainment rate was defined as positive when the depth of entrainment was decreasing.

$$\dot{e} = -\frac{\Delta H}{\Delta t}, \qquad (10)$$

where $\dot{e}$ was the entrainment rate [m/s], ΔH was the change in entrainment height [m], and Δt was the change in time [s]. Averages over different lengths of time were taken in order to determine how sensitive the entrainment rate was to the averaging. Most often we would begin recording experiments immediately before the supply was released. As such, there is almost always some lag between the beginning of the recording and the beginning of the debris flow. As we mentioned earlier in this chapter in Section III.

General Behavior of Flow, the very beginning of the flow for experiments released from *IP1* is quite sparse, and so we could not just use the point at which the first moving particle appears. Instead, based on visual inspection, we considered the "start" of the debris flow, or $t=t_s$ where t_s is the time when the debris flow "starts," to occur when the flowing layer was 0.002 m thick and began averaging from that time onward. It should be noted that in Figure 18 the initial depth of the bed, H_o, at the start of the flow is not exactly zero. While we do not consider the start of flow to begin until the flow is sufficiently dense to begin entrainment, the initial sparse flow can cause some entrainment of materials. However, this initial entrainment is typically negligible, as we see in Figure 18.

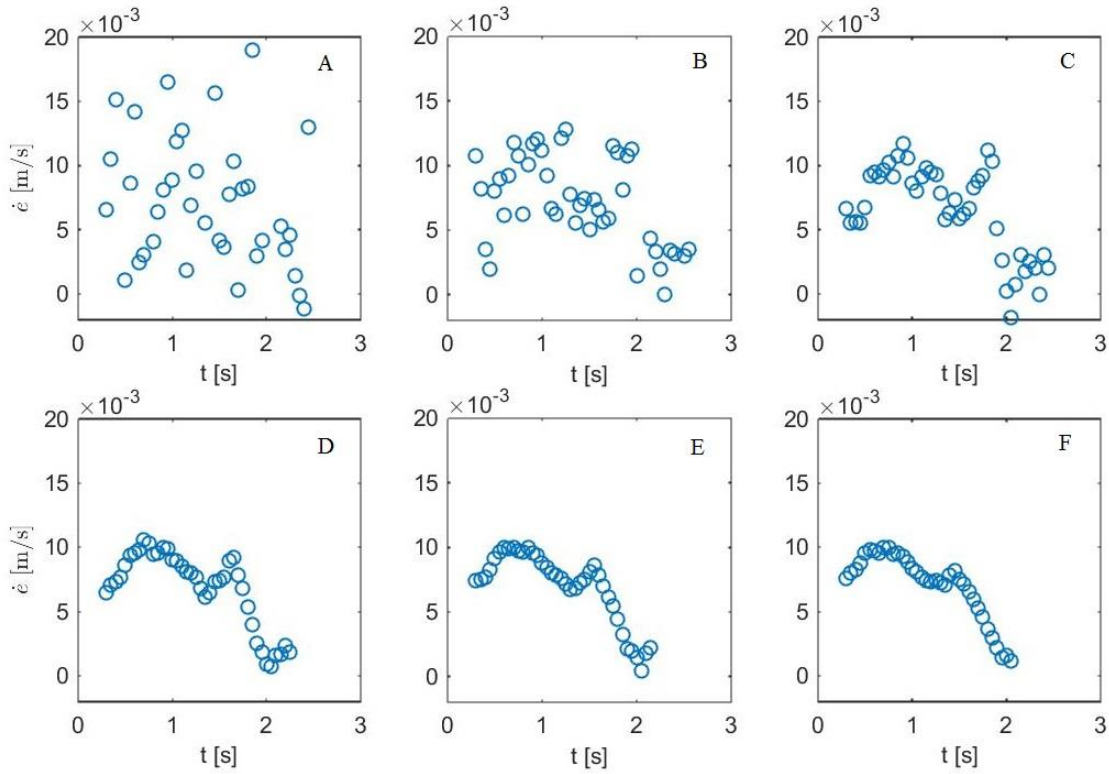

Figure 19: Various time averages for entrainment rate. A is averaged over 0.1 seconds, B 0.2 s, C 0.3 s, D 0.5s, E 0.6 s, and F 0.7 s.

Figure 19 demonstrates some of the results of these different averaging schemes. The final average chosen was 10 time steps, or Δt=0.5 seconds, since it captured changes in the entrainment rate without being overly sensitive to those changes.

V. Top of Flowing Layer

In determining quantities such as shear stress, the thickness of the flowing layer was required. This involved determining what portion of the debris flow was moving. Two sections of the flowing layer were identified. Right above the stationary portion of the bed is a dense flowing layer. Here, particles are closely packed together, typically with a solid fraction of approximately 0.5. The solid fraction was calculated for each bin, and is defined as the total volume taken up by particles per volume of the bin. As you move away from the interface of motion/no motion, the flow remains dense for a while and then suddenly becomes sparse, as seen in Figure 20. This sparse portion of the flowing layer begins slightly below the apparent surface of the flowing layer and contains particles that have been sent upwards over the rest of the flow as they sail over the main body and then fall back down.

The question at this point was what to consider as the flowing layer in calculating shear stress and velocity fluctuations. Initially, we thought to consider only the dense portion of the flow, since this was where the main bulk of the flow that would be affecting the system was. In order to consider just the dense flow, a threshold was needed to systematically define the top of the dense portion of the flowing layer. Based on visual inspection of the solid fraction profile, the solid fraction fluctuates between approximately 0.4 and 0.5 in the dense region. In order to capture the beginning of the dense region, 0.4 was chosen as the threshold for the dense portion of the flow. To begin, an exponential function was used to approximate the shape of the solid fraction profile near a value of 0.4 with the following form.

$$y = Ae^{Bf}, \tag{11}$$

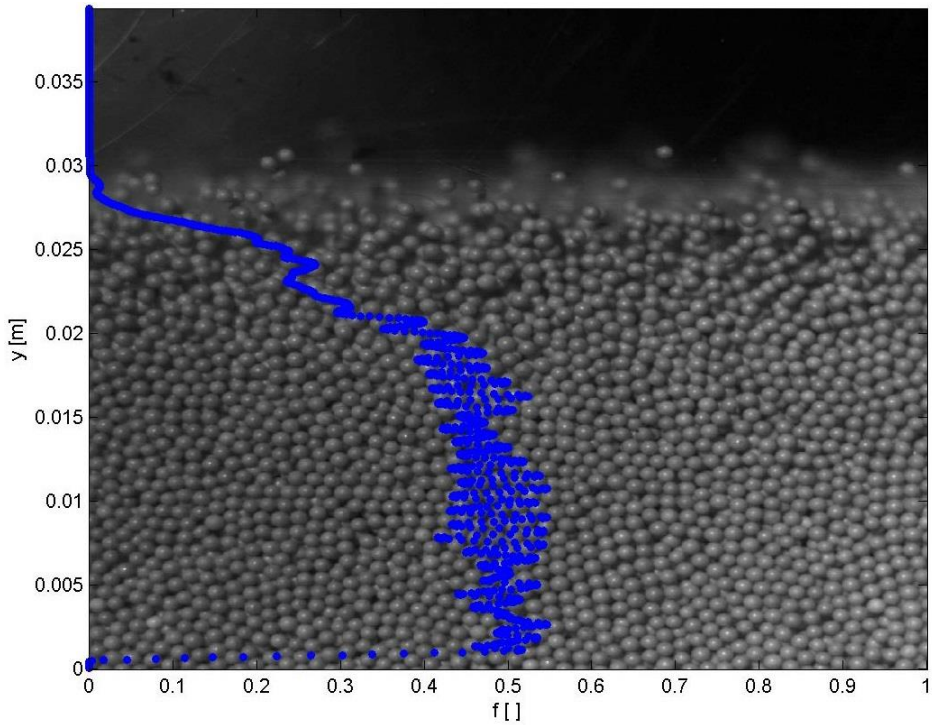

Figure 20: Solid Fraction, f, versus vertical distance, y, 1 s into the flow.

where *y* [m] was the vertical position, *f* [ ] was the solid fraction at that position, and *A* and *B* were constants. By taking the natural logarithm of both sides, the function became linear, and we found the constants A and B with least squares linear best fit as seen below.

$$ln(y) = ln(A) + Bf \tag{12}$$

With the constants, we determined the height at which the dense portion of the flowing layer begins. To see how well this exponential function fit the data, the linear-log plot in Figure 21A was created. As can be seen in Figure 21, the exponential fit is not perfect. However, near the threshold solid fraction, the data seemed fairly linear, so a linear fit was also used to approximate solid fraction at the top of the dense layer. This linear fit, while still an arbitrary choice, was a significantly better approximation of the solid fraction near the top of the dense layer as seen in Figure 21B.

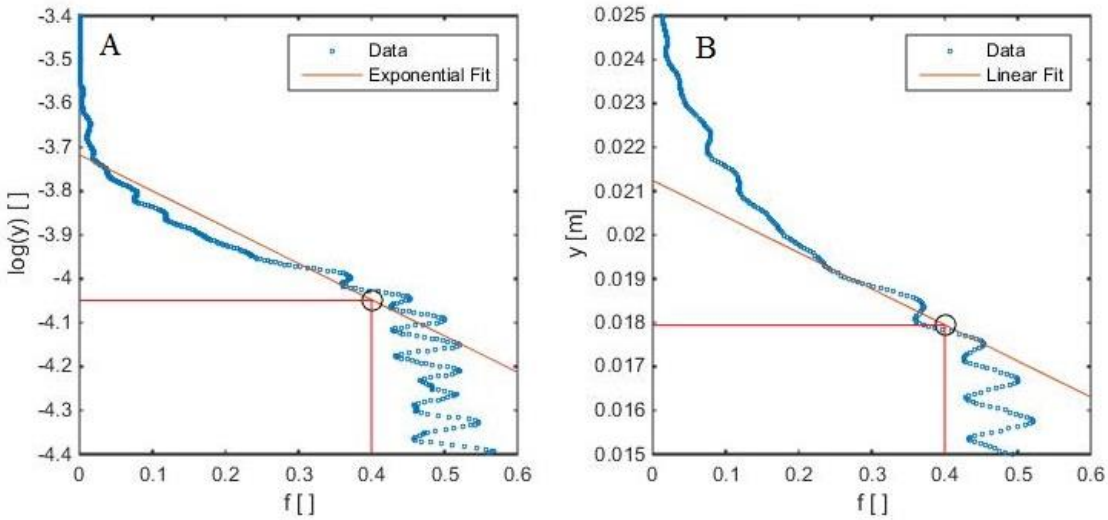

Figure 21: Exponential fit (A) and linear fit (B) of solid fraction profile.

Now, with a good approximation of the top and bottom of the flowing layer, we could begin analyzing factors suspected to correlate with entrainment rate using both the dense and full portions of the flowing layer.

VI. Dense vs Full Flowing Layer

In this section, we describe briefly how the stress associated with the particle weight, the particle temperature, and the downstream and vertical velocity fluctuations, the Reynolds stress, varied based on whether we considered just the dense flowing layer or the full flow depth. The first factor examined was shear stress. The shear stress along the bottom of the flowing layer, τ [N/m^2], was calculated using a basic depth slope equation, as seen below:

$$\tau = \rho g h S \ , \qquad (13)$$

where ρ [kg/m^3] was the density of the system, g [m/s^2] was acceleration due to gravity, h [m] was thickness of the flowing layer as seen in Figure 17 for a dense flow, and S [ ] was slope of the bed. Using $S = sin(\theta)$, where θ was the angle of inclination of the flume and $\rho = \rho_m \bar{f}$, where ρ_m [kg/m^3] was the material density, and $\bar{f}$ was the average

solid fraction over the section of flow considered, we have the following expression for shear stress at each time step.

$$\tau = \rho_m \bar{f} g h sin(\theta) \tag{14}$$

We also investigated the effects of granular temperature by taking the average over different thicknesses. The average granular temperature, $\langle T \rangle$ [Pa], over the thickness of the layer, was determined by summing from the bottom of the flowing layer, i_{bottom}, to the top "bin" of the layer, i_{top}.

$$\langle T \rangle = \frac{\sum_{i=i_{bottom}}^{i=i_{top}} \rho_m f_i (\overline{u'u_i'} + \overline{v'v_i'})}{i_{bottom} - i_{top}}, \tag{15}$$

where $\overline{u'u'}$ was the horizontal velocity fluctuation, and $\overline{v'v'}$ was the vertical velocity fluctuation. We also considered the average Reynolds shear stress, $\langle \tau_R \rangle$ [Pa], over the thickness of the layer, where $\overline{u'v'}$ was the tangential velocity fluctuations.

$$\langle \tau_R \rangle = \frac{\sum_{i=i_{bottom}}^{i=i_{top}} \rho_m f_i \overline{u'v_i'}}{i_{bottom} - i_{top}} \tag{16}$$

As illustrated in Figure 17, the dense portion of the flow was the area defined by the depth of the entrainment and the height at which the solid fraction reaches 0.4. Full thickness of flow was defined by the depth of the entrainment to the top of the image. Figure 22 shows the shear stress, granular temperature, and Reynolds stress considering both the dense and full flows.

As seen in Figure 22A, the main difference between the full flow and dense portion was the magnitude of the stress. Based on that information, we chose to consider the full flowing layer for the shear stress. For the granular temperature, $\langle T \rangle$, and Reynolds shear stress, $\langle \tau_R \rangle$, the difference between the full flowing layer and dense flowing layer was a little more complicated. Since those calculations were spatially averaged based on the thickness of the layer we were considering, we decided to look into how $\langle T \rangle$ and $\langle \tau_R \rangle$ varied when calculated over different length scales (see Figure 23). These length scales started at one bead diameter, *d*, and increased by whole bead diameters, up to

approximately the maximum thickness of the dense flowing layer. The example shown in Figure 23 has a dense layer maximum depth of approximately 20 bead diameters, or 0.016 m. Due to the added complexity for the behavior of $\langle T \rangle$ and $\langle \tau_R \rangle$, we discuss the details with the results in the next chapter.

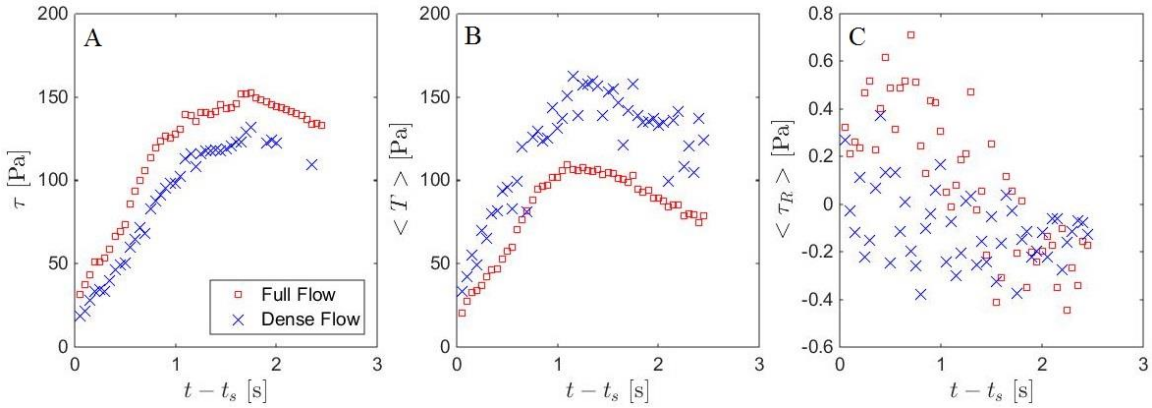

Figure 22: Comparison of the dense and full flowing layers of time after start of flow, t-t_s. A is shear stress, τ, B is average granular temperature/thickness of the layer considered, $\langle T \rangle$, and C is average Reynolds stress/thickness of the layer considered, $\langle \tau_R \rangle$.

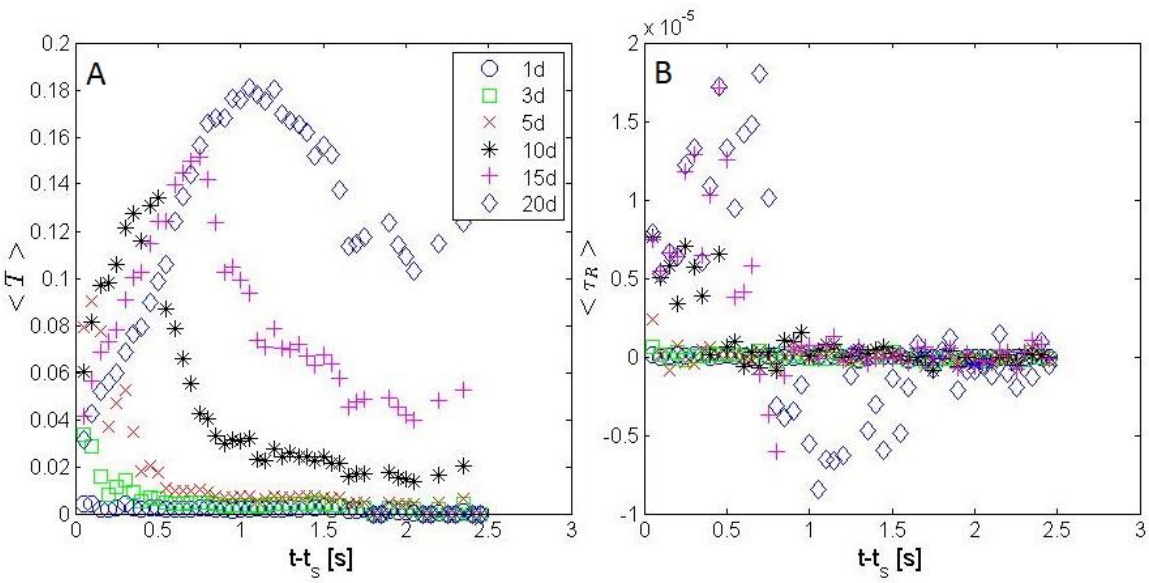

Figure 23: A average granular temperature, $\langle T \rangle$, and B average Reynolds shear stress, $\langle \tau_R \rangle$, over time after the start of the flow, t-t_s. Both $\langle T \rangle$ and $\langle \tau_R \rangle$ were calculated over length scales of 1, 3, 5, 10, 15, and 20 bead diameters, d.

Chapter 4: Experimental Results: Entrainment Rate and Associated Mechanisms

Using the image analysis methods discussed in Chapter 3, we were able to identify the entrainment depth and find an associated entrainment rate under a wide variety of boundary conditions for our experimental debris flows. In this chapter, we describe how we used the methods developed for measuring various quantities proposed to influence entrainment rates. Additionally, we examine which characteristics of the debris flow affect those quantities. We also discuss how certain boundary conditions affected the entrainment depth and rate. Then we discuss how parameters previously proposed responsible for setting the rate of entrainment, such as shear stress, granular temperature, and Reynolds stress, correlate with our measured entrainment rates. We first briefly discuss baseline and unambiguous measurements associated with entrainment, specifically, net erosion of particles from the bed over an entire experiment.

I. Net Erosion

To develop some baseline measure of entrainment for each experiment performed, we measured the net erosion due to the debris flow. Net erosion was determined using the following expression:

$$Net\ erosion = \frac{m_s - m_o}{m_s}, \qquad 17$$

where m_o was the mass out, and m_s was the mass of the debris flow supply. In Figure 24, we present these data from one set of experiments--those from set 1, Table 3--using particles of 0.8 mm. From these results, we can see how the net erosion changed as the angle of inclination, θ, increased. The typical duration for of an erosion event was approximately 15 s. As θ increased, so did the net erosion. We can also obtain the neutral

angle from Figure 24 based on when we had a net erosion of zero: in this case, the neutral angle was at 23.5°. With these data, we have also plotted information from the instantaneous entrainment rate. As detailed in Chapter 3, these data were obtained every 0.1 s of the experiment and are the result of averaging over 0.5 seconds of data. The trends are similar, that is, there was a modest increase in entrainment rate as the angle of inclination was increased. However, the range of entrainment rates for any particular angle was greater than the increase over all angles. Further, the average entrainment rate was not monotonically increasing for all time steps, as we discuss shortly.

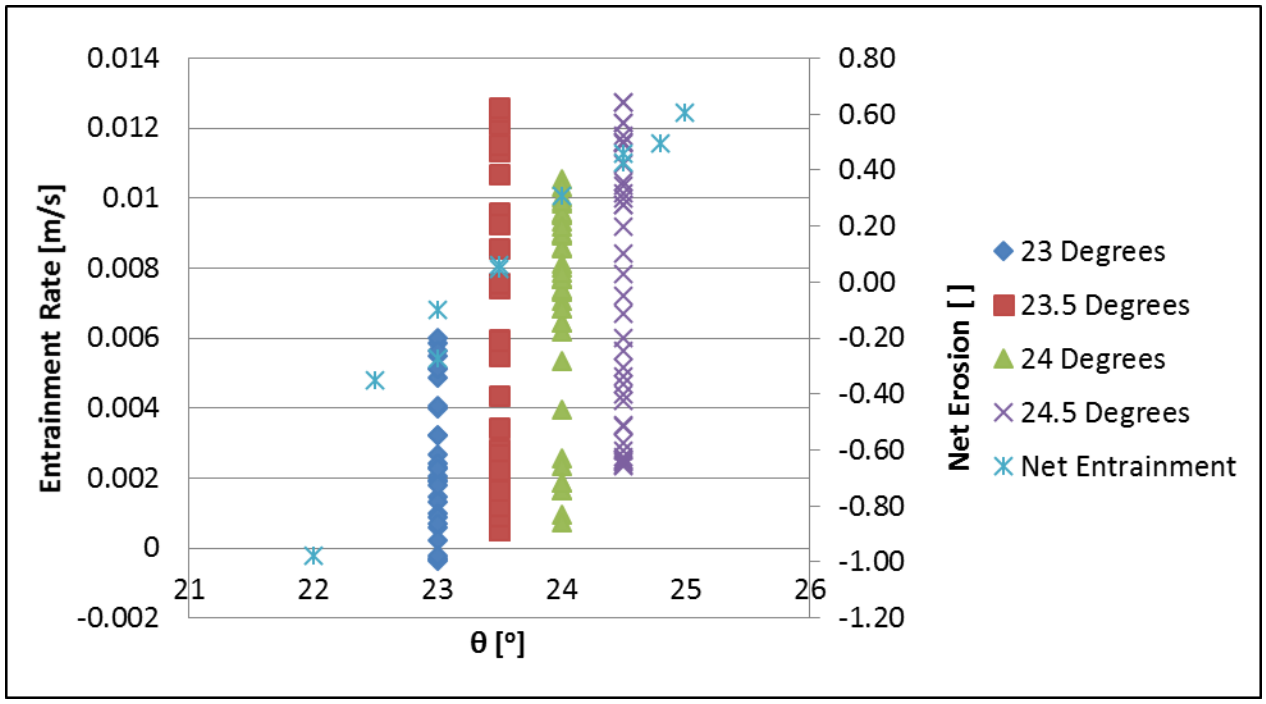

Figure 24: Instantaneous entrainment rate, $\dot{e}$, and net erosion for experiments at IP1 with 0.8 mm particles, A_r=0.27, V/B=0.034m^2. (Other details of the experimental conditions can be found in Table 3.) Each entrainment rate data point is time averaged over 0.5 seconds throughout the experiment; the erosion takes place over approximately 15 s. We can turn to Figure 26B to see how entrainment rate varies as a function of time.

II. Variability

We expect a certain amount of natural variability for experiments such as those for a debris flow. Due to the nature of a granular flow and the noisiness of these data, such

differences are to be anticipated. In this section, we briefly consider this variability to use as a baseline to compare trends in our results to differences that may be present due to natural variability from one experiment to the next. As indicated in Table 3 and Table 4, we performed duplicate experiments for most of the boundary conditions considered. In Figure 25, we see an example of the differences between two experiments performed under identical conditions. The general trends agree with one another, but we see minor differences in the instantaneous behavior. Therefore, any differences similar to the magnitude of those shown here cannot be assumed significant.

We also use this plot to note that at $t=t_s$, the depth of entrainment is less than zero. While there can be entrainment by the initial sparse portion of a debris flow, we consider the start of flow to occur once the debris flow itself is denser as defined in Chapter 3.

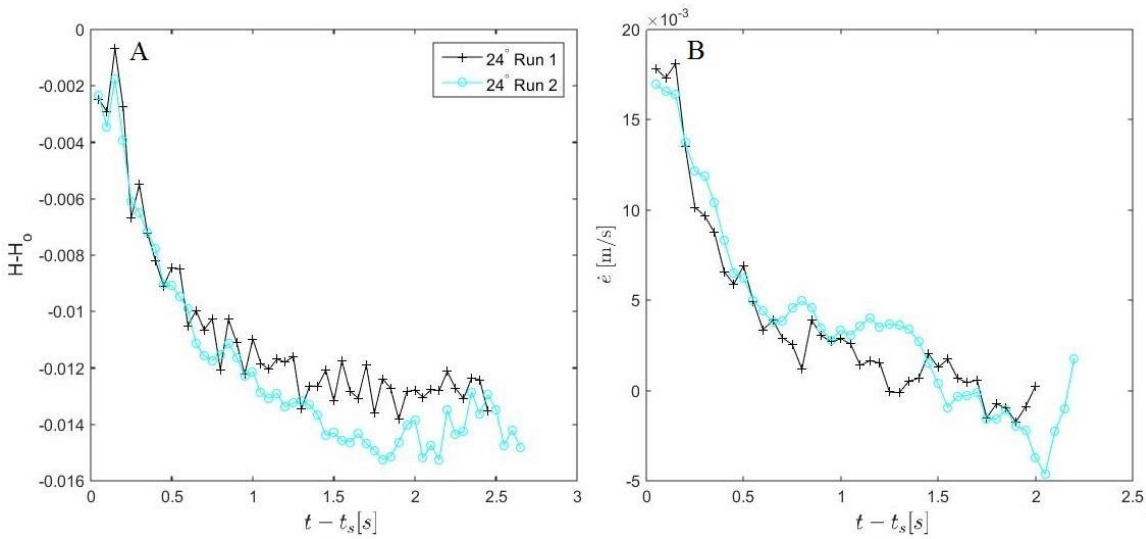

Figure 25: A entrainment depth normalized by the initial depth, $H-H_o$, versus time after the front arrival, $t-t_s$. B entrainment rate, $\dot{e}$, versus $t-t_s$. These experiments are referred to as E1_2_24.0_I3 in Table 3. Both were performed at IP1 with 2 mm particles, $A_r=0.027$, $V/B=0.034\ m^2$.

III. General Entrainment Results

We are primarily concerned in mechanisms associated with entrainment that are common across a wide variety of boundary conditions. To help determine this, we performed some

systematic variations of certain boundary conditions while others were held constant. By selecting one attribute at a time to vary while keeping all other conditions constant, we isolated each boundary condition and examined it. These boundary conditions are angle of inclination, θ; bead diameter, d; volume/breadth of the supply, V/B; aspect ratio of the supply, A_r; and the initial position of the supply, IP. While not of primary concern to us, it is useful to understand this variability. In this section, we consider how the different boundary conditions were correlated with entrainment depth and height.

III A. Angle Dependence and Bead Size

Among all our investigations, for a given set of conditions, we find that changing the angle of inclination or the particle diameter had the greatest effect on entrainment rate and depth out of all the boundary conditions we considered. In general, increasing the angle of inclination leads to deeper entrainment depths and higher entrainment rates (see Figure 26, Figure 27). In the context of a neutral angle, θ_n, this was exactly what we would expect; as the difference between the angle of inclination, θ, and θ_n increases, entrainment rate should increase, (see Equation 1). While this trend was not perfectly maintained, we did see the general trend holding for both the 0.8 mm and 2 mm experiments.

Since the dependence of particle size on entrainment rate was not one of our main focuses, only two bead sizes were used (to help ensure our analysis was not a function of one particular particle size).We did see that increasing the particle size led to reaching the maximum entrainment depths sooner but not necessarily to a deeper maximum depth. Figure 28B shows how this manifested in the entrainment rate profile, where for the 2mm particles we consistently saw entrainment rate decrease initially, recover to reach the maximum entrainment rate, and then decrease as the entrainment depth begins to level off. For the 0.8 mm case, we typically saw entrainment rate increase initially, as demonstrated in Figure 28B, until the maximum value was reached, at which point similar behavior to what was observed with the 2 mm case was seen with the decreasing entrainment rate.

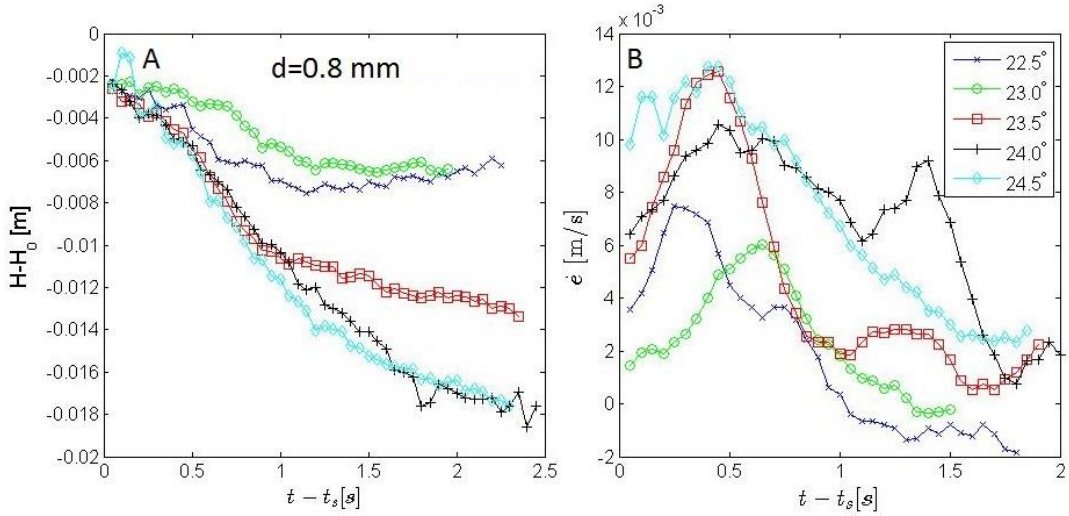

Figure 26: A, normalized depth of entrainment, H-H$_o$, where H$_o$ is the initial depth of bed, over time after front arrival, t-t$_s$. B, entrainment rate, $\dot{e}$, over t-t$_s$. Angle of inclination, θ, is varied as initial position, particle diameter, d, aspect ratio, A$_r$, and volume/width of supply, V/B, are kept constant at IP1, d=0.8 mm, A$_r$=0.27, V/B=0.034 m^2. (These represent all 0.8 mm experiments in Table 3).

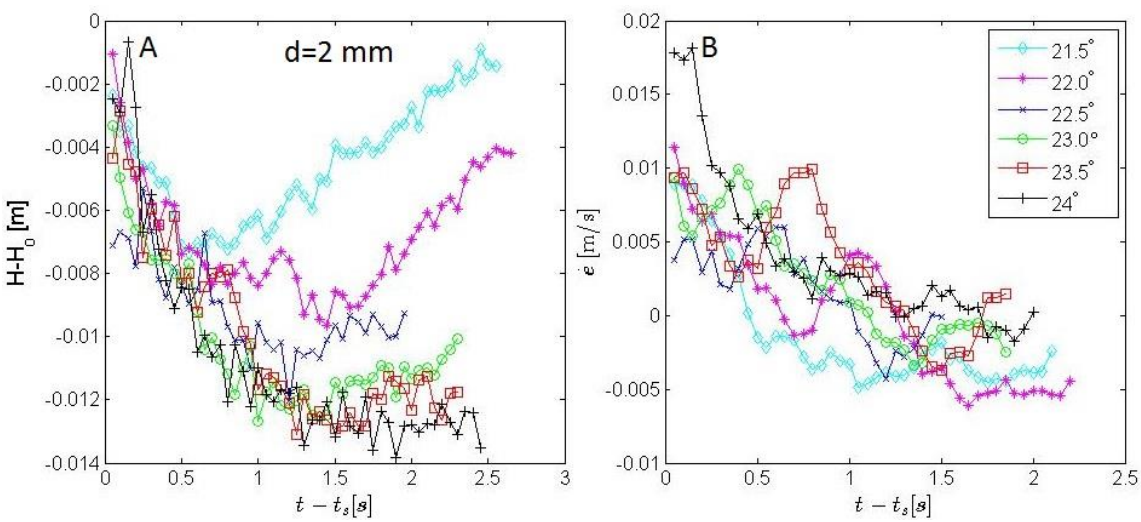

Figure 27: A, normalized depth of entrainment, H-H$_o$, where H$_o$ is the initial depth of bed, over time after front arrival, t-t$_s$. B, entrainment rate, $\dot{e}$, over t-t$_s$. Angle of inclination, θ, is varied as initial position, particle diameter, d, aspect ratio, A$_r$, and volume/width of supply, V/B, are kept constant at IP1, d=2 mm, A$_r$=0.27, V/B=0.034 m^2 (These represent all 2 mm experiments in Table 3).

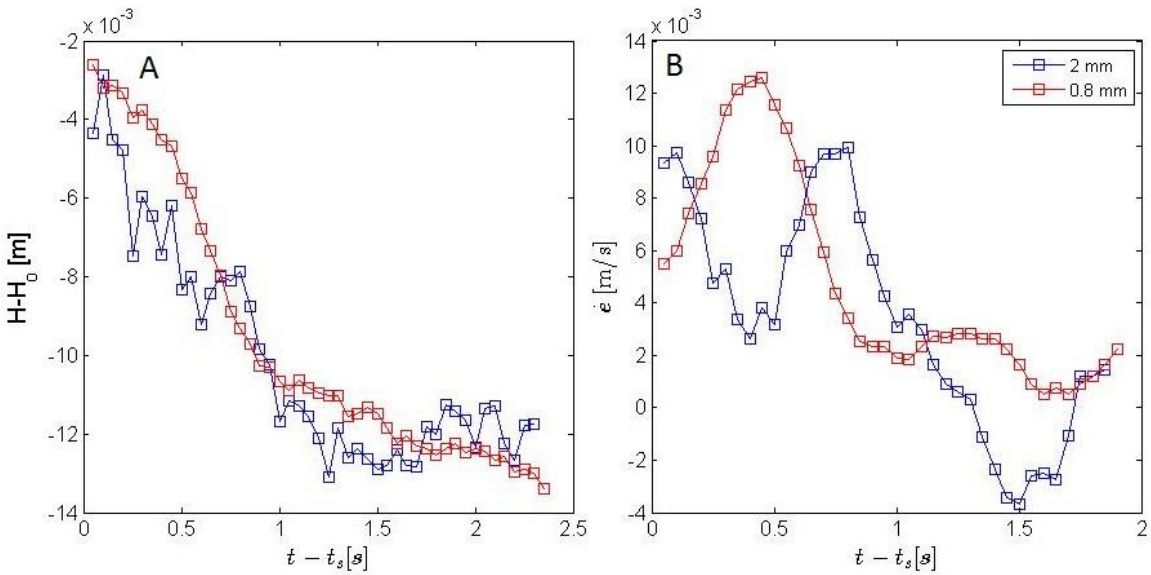

Figure 28: A, normalized depth of entrainment, H-H$_o$, where H$_o$ is the initial depth of bed over time after front arrival, t-t$_s$. B, entrainment rate, $\dot{e}$, over t-t$_s$. Particle diameter, d, is varied as initial position, θ, A$_r$, and V/B, are kept constant at IP1, 23.5^o, A$_r$=0.27, V/B=0.034 m^2 (These represent experiments E1_2_23.5_I3 and E1_0.8_23.5_I3 in Table 3).

III B. Volume/Breadth Dependence

In Figure 29 through Figure 32, we plotted data in such a way to easily investigate how the volume/breadth of the supply, V/B, affected entrainment rate. In each figure the aspect ratio, A_r, and all other boundary conditions was kept constant, and *V/B* was increased. With each subsequent figure (from Figure 29 to Figure 32), A_r increased from 0.27 to 0.50. In Figure 30 through Figure 32 we saw that as *V/B* increased, an initial drop in entrainment depth, common to most of our experiments, cut deeper into the erodible bed. We see the opposite behavior in Figure 29. We see that the entrainment rates fluctuated similarly as *V/B* varied, although in Figure 30 and Figure 31 we see that for different *V/B* the amplitude of the fluctuations changed.

While we do observe some limited trends, none of these behaviors extended to all cases. Therefore, we conclude that *V/B* of the debris flow supply does not have a strong control over the entrainment depth or rate. The results of Farin et al. (2014) also suggest that increasing the volume/width causes an increase in the time of erosion, but not necessarily

the depth of entrainment. We speculate the initial volume of a debris flow is not a major concern modeling entrainment rate in field scale debris flows, but more for experimental scale setups.

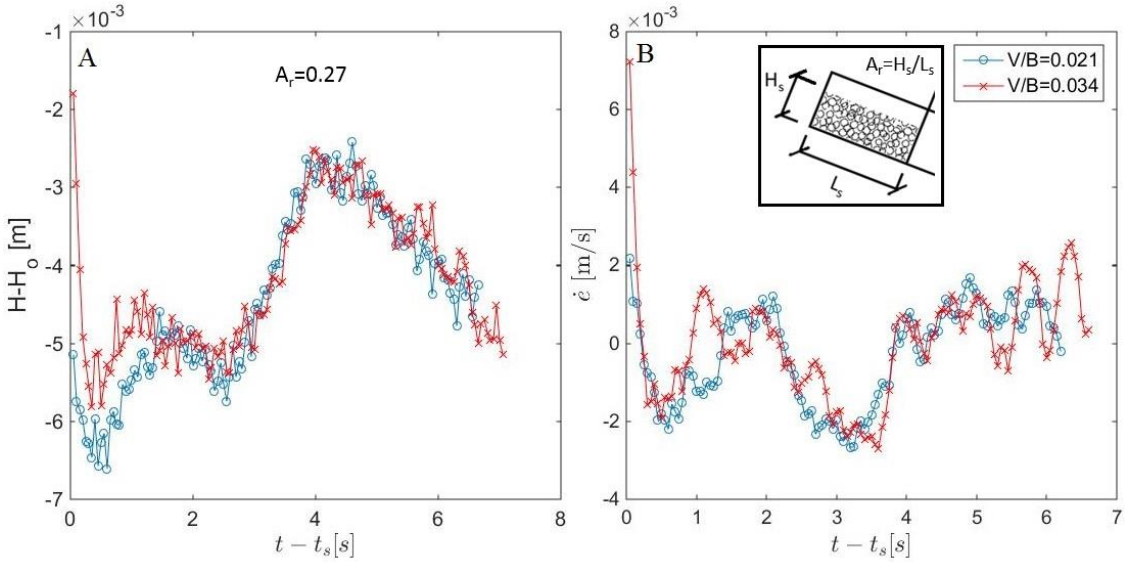

Figure 29: A, normalized depth of entrainment, H-H_o, where H_o is the initial depth of bed over time after front arrival, t-t_s. B, entrainment rate, $\dot{e}$, over t-t_s. Volume/width of supply, V/B, is varied as initial position, θ, d, and A_r, are kept constant at IP2, 23.5^o, d=0.8 mm, A_r=0.27. Inset shows the aspect ratio (These represent experiments with A_r=0.27 from Table 4).

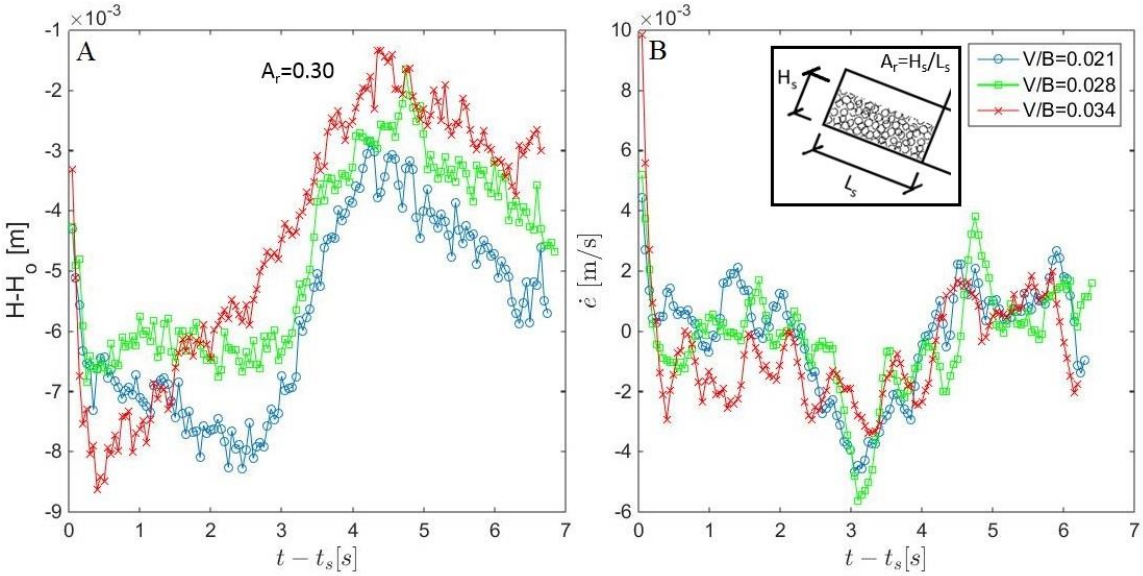

Figure 30: A, normalized depth of entrainment, H-H$_o$, where H$_o$ is the initial depth of bed over time after front arrival, t-t$_s$. B, entrainment rate, $\dot{e}$, over t-t$_s$. V/B, is varied as initial position, θ, d, and A$_r$, are kept constant at IP2, 23.5^o, d=0.8 mm, A$_r$=0.30. Inset shows aspect ratio (These represent experiments with A$_r$=0.30 from Table 4).

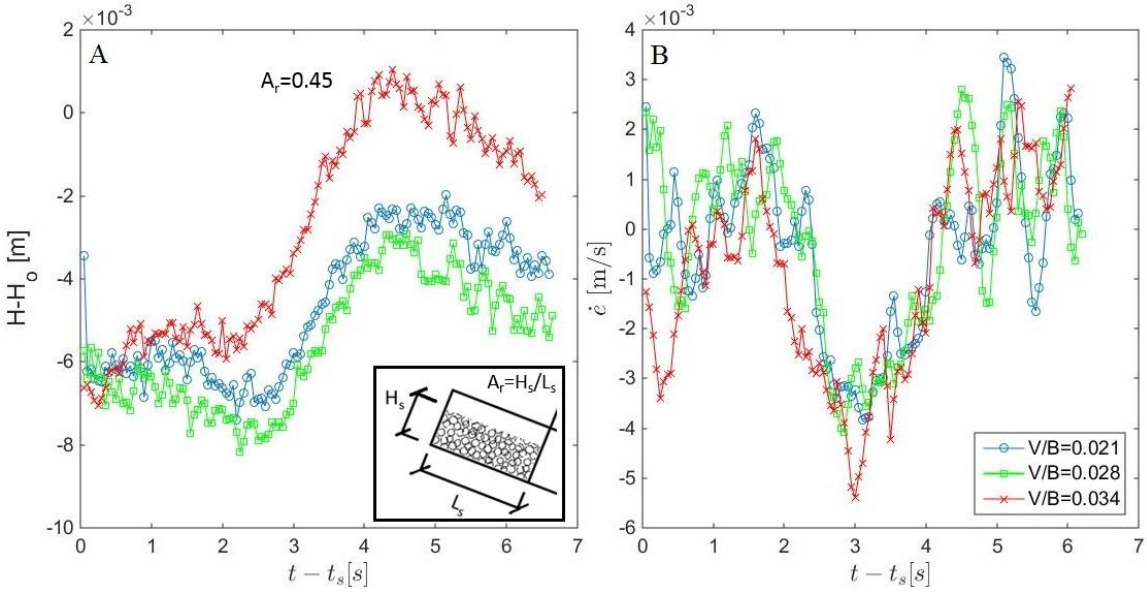

Figure 31: A, normalized depth of entrainment, H-H$_o$, where H$_o$ is the initial depth of bed over time after front arrival, t-t$_s$. B, entrainment rate, $\dot{e}$, over t-t$_s$. V/B, is varied as initial position, θ, d, and A$_r$, are kept constant at IP2, 23.5^o, d=0.8 mm, A$_r$=0.45. Inset shows aspect ratio (These represent experiments with A$_r$=0.45 from Table 4).

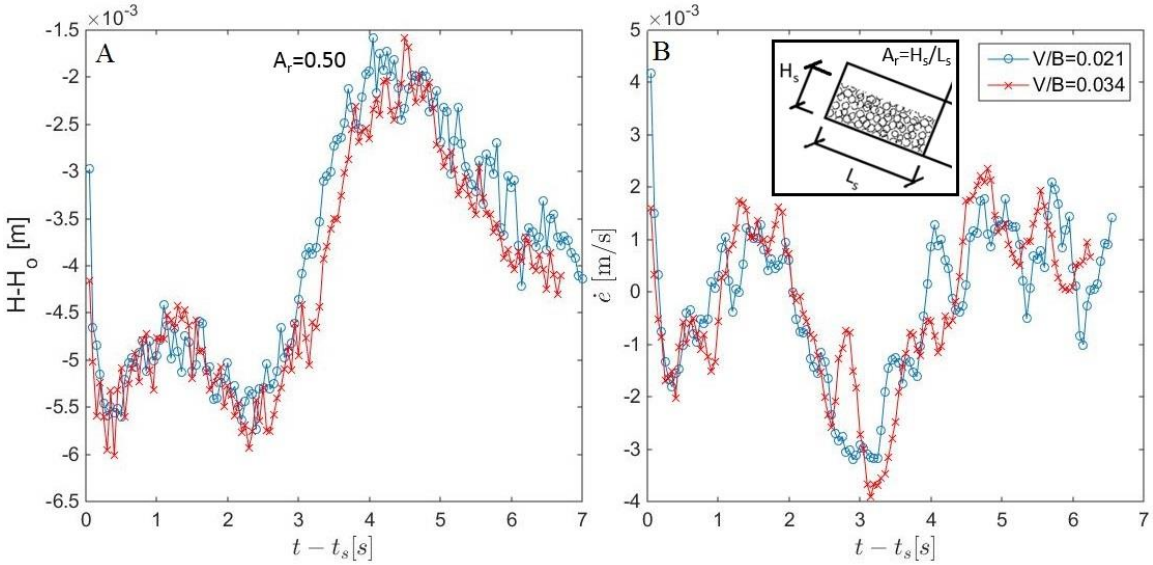

Figure 32: A, normalized depth of entrainment, H-H$_o$, where H$_o$ is the initial depth of bed over time after front arrival, t-t$_s$. B, entrainment rate, $\dot{e}$, over t-t$_s$. Volume/width of supply, V/B, is varied as initial position, θ, d, and A$_r$, are kept constant at IP2, 23.5^o, d=0.8 mm, A$_r$=0.50. Inset shows aspect ratio (These represent experiments with A$_r$=0.50 from Table 4).

III C. Aspect Ratio Dependence

Similarly to the volume/breadth discussion, we investigated how the aspect ratio, A_r, affected entrainment rate in Figure 33 through Figure 35. In each figure, *V/B* and all other boundary conditions were kept constant and A_r was increased. With each subsequent figure, *V/B* increased from 0.021 m^2 to 0.034 m^2. In Figure 33 through Figure 35, we saw that for all aspect ratios other than 0.27, as aspect ratio decreased, the initial drop in depth of entrainment increased. We saw a corresponding trend in those same figures where, as A_r decreased, entrainment rates were greater during the initial drop.

As was the case for volume/breadth, there was not a straightforward relationship between entrainment and aspect ratio. The results of Farin et al. (2014) also suggest that decreasing aspect ratio does not necessarily cause an increase in the depth of entrainment. Similar to the volume/breadth of supply, we suspect that the aspect ratio of the supply is not a major concern for field scale debris flows. We again speculate that while boundary conditions are important as the debris flow travels downslope, any memory of the aspect

ratio or influences of the initial volume are lost, and other dynamics are more important for debris flow entrainment.

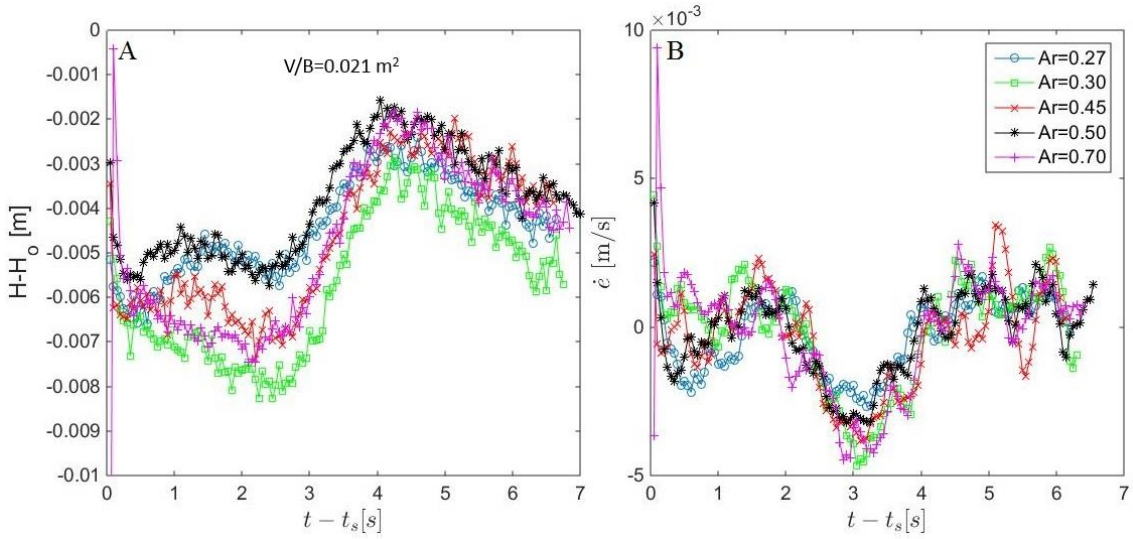

Figure 33: A, normalized depth of entrainment, H-H$_o$, where H$_o$ is the initial depth of bed over time after front arrival, t-t$_s$. B, entrainment rate, $\dot{e}$, over t-t$_s$. Aspect ratio, A$_r$, is varied as initial position, θ, d, and V/B, are kept constant at IP2, 23.5^o, d=0.08 mm, V/B=0.021 m^2 (These represent experiments with V/B=0.021 m^2 from Table 4).

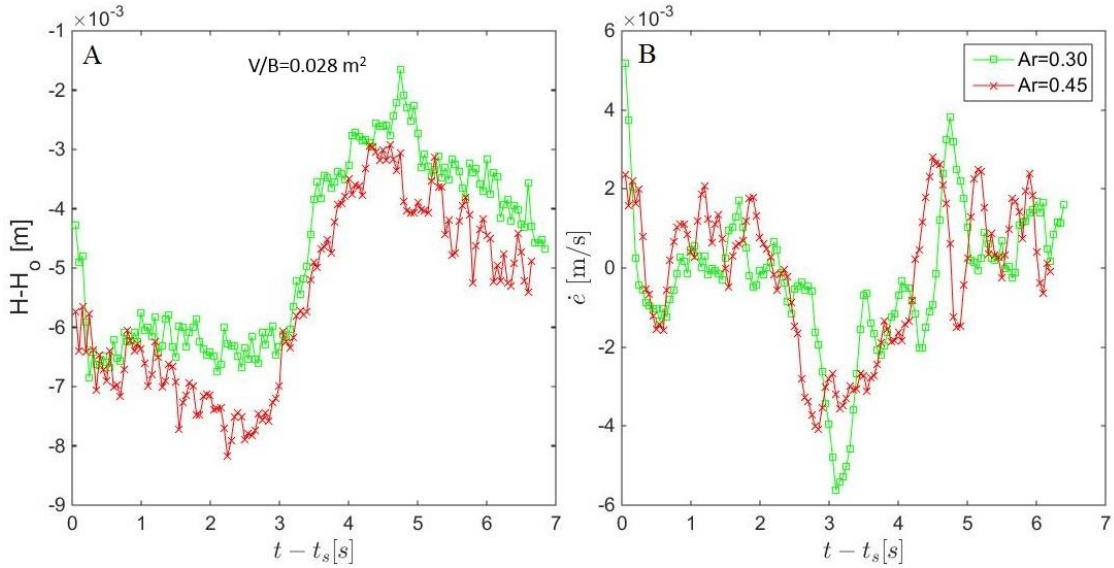

Figure 34: A, normalized depth of entrainment, H-H$_o$, where H$_o$ is the initial depth of bed over time after front arrival, t-t$_s$. B, entrainment rate, $\dot{e}$, over t-t$_s$. Aspect ratio, A$_r$, is varied as initial position, θ, d, and V/B, are kept constant at IP2, 23.5^o, d=0.08 mm, V/B=0.028 m^2 (These represent experiments with V/B=0.028 m^2 from Table 4).

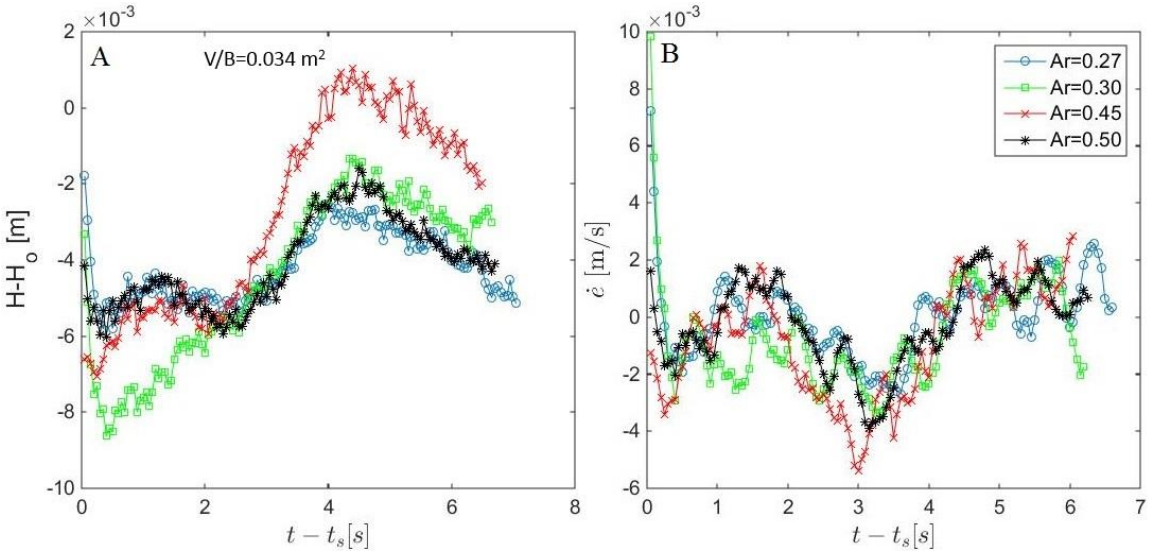

Figure 35: A, normalized depth of entrainment, H-H_o, where H_o is the initial depth of bed over time after front arrival, t-t_s. B, entrainment rate, $\dot{e}$, over t-t_s. Aspect ratio, A_r, is varied as initial position, θ, d, and V/B, are kept constant at IP2, 23.5^o, d=0.08 mm, V/B=0.034 m^2 (These represent experiments with V/B=0.034 m^2 from Table 4).

III D. Initial Position Dependence

While we performed primarily two sets of experiments – one from an upslope position where we systematically varied bed angle, and the second from a downslope position where we systematically varied supply dimensions – we also investigated to a limited extent how initial position influenced our measurements. We considered that starting our debris flows in the initial position one was somewhat more similar to the conditions of a real debris flow, in that the supply accelerated and thinned for some time before entraining any material (e.g. conditions in Stock and Dietrich, 2006; Iverson et al., 2010; McCoy et al., 2012, 2013). Initial position two was similar to the boundary conditions for a granular physics problem investigating the rheology of a granular flow. Both types of setups have been studied by various groups (e.g. Capart and Young, 1998; Papa et al., 2004), and have important applications in debris flows. However, considering the dichotomy between these two sets of boundary conditions, we wanted to study how these conditions affect entrainment. In Figure 36 we see how the entrainment depth varies with a change in the initial position. Using the data from experiments performed at *IP2*, we

could also compare our results with the extensive work done by Mangeney et al. (2010) and Farin et al. (2014). Their work was performed under boundary conditions similar to *IP2*, which also allowed us to investigate a subtly different condition.

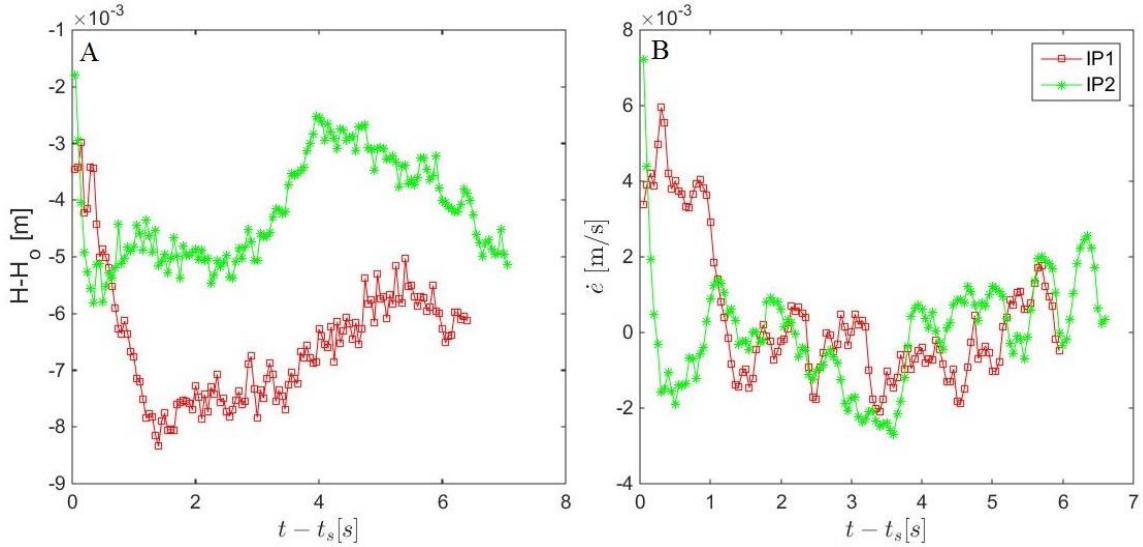

Figure 36: A, entrainment depth, H, normalized by the initial depth, H_o, as a function of time after the start of flow, t-t_s. B entrainment rate, $\dot{e}$, over t-t_s, for 0.8 mm experiments at 23.5^o, with A_r=0.27, V/B=0.034 m^2, at IP1 and IP2. These represent experiments E2_27_34_1_I2 and E2_27_34_2_I2 from Table 4).

We see that for *IP2*, when the supply was released much closer to the erodible bed, maximum entrainment depth occurred much sooner and was much shallower than a corresponding experiment at *IP1*. The initial behavior in *IP2* of quickly cutting down to the maximum entrainment depth was also seen in other experiments performed at that same initial position. It was also quite similar to the initial behaviors seen by Mangeney et al. (2010) in Figure 37. There we also see the quick initial cut down to the maximum entrainment depth. In both cases, the maximum entrainment depth was comparable, roughly 6mm and 4mm.

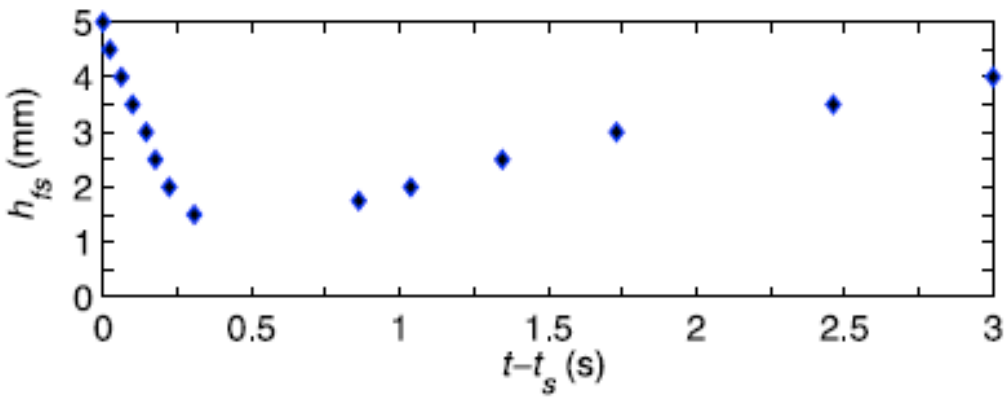

Figure 37: Mangeney et al. (2010) entrainment depth, h_{fs}, as a function of time after front arrival, t-t_s, measured at x=0.90m. A_r=0.70, V/B=0.028 m^2, θ=25.4°.

As we look at later times in the entrainment depth profile, the behavior of the Moberly/Mullenbach experiments diverges from the Mangeney et al. (2010) results. After the linear drop in entrainment depth, Mangeney et al. (2010) described the flowing/static interface as remaining at a roughly constant elevation for about 0.5s, then moving back upwards with an exponential relaxation. In the Moberly/Mullenbach experiment at *IP2* we see a similar drop in entrainment height, but, instead of remaining relatively constant, the interface moves upwards with an exponential-type profile for about 0.5s. It then gradually moves back downwards again for two seconds, turns upwards to begin depositing for approximately one second, and finally switched directions to seemingly begin to entrain material for the remaining time. We could not compare the full length of the two experiments since that data was not available, but there was a difference over the time scales that we could compare.

We considered the time period directly following the initial penetration of the static/flowing interface into the previously static bed. As mentioned, Mangeney et al. (2010) saw a period of relatively constant entrainment depth. The work by Farin et al. (2014) also profiled the entrainment depth, but at various points along the debris flow flume, as seen in Figure 38 below.

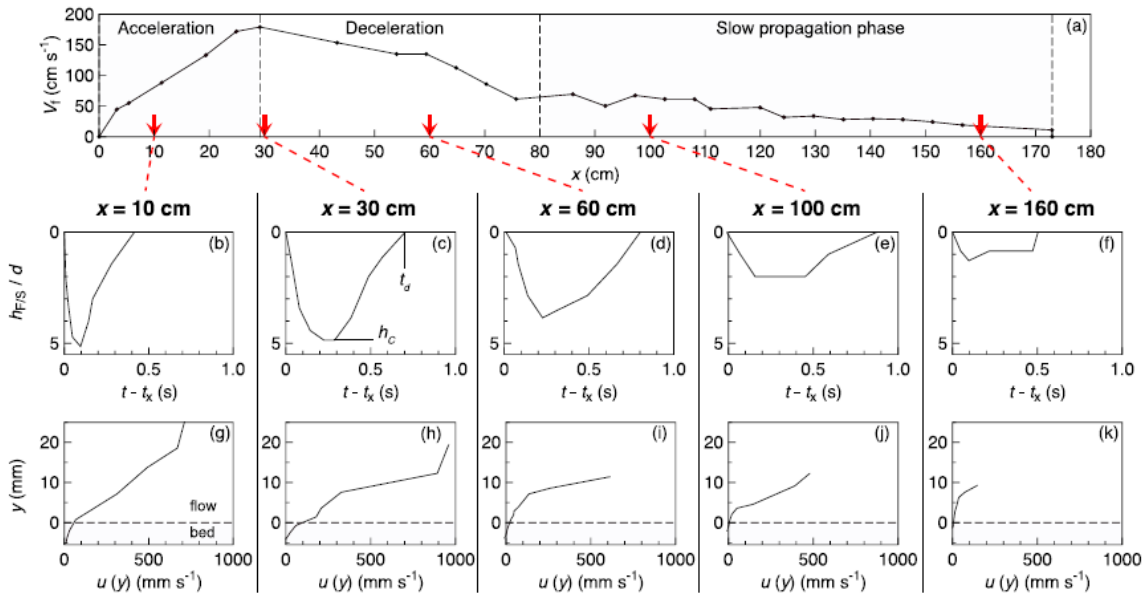

Figure 38: Farin et al. (2014) entrainment depth and velocity profiles at different points along the debris flow flume for the case of θ=23°, V/B=0.028 m^2, and A_r=0.30. Figure A shows the front velocity, V_f, in cm/s with respect to the distance downstream from the release point, x. Figures B-F are the entrainment depth, $h_{F/S}$, as a function of time after the front arrival, t-t_x. Figures G-K show the internal flow velocity u(y) as a function of elevation, y, above the channel base when the $h_{F/S}$ reaches its maximum depth, h_c.

Upon closer inspection of the different entrainment profiles, Figure 38E, at x=100 cm in the slow propagation phase exhibited similar behavior to the Mangeney et al. (2010) result. This was also at a similar distance downstream of the release point in Farin et al. (2014): 90 cm in the Mangeney et al. (2010) versus 100 cm in Farin et al. (2014). The Moberly/Mullenbach experiments were measured approximately 30 cm downstream of the release point for *IP2*, and seemed to share more features with the corresponding Farin et al. (2014) entrainment profile than the Mangeney et al. (2010). Both quickly moved down to the maximum entrainment depth and then promptly moved back upwards. This profile was similar for all of the Moberly/Mullenbach experiments, suggesting that the entrainment profile was dependent on the distance from the gate and that the difference in position was the main reason for the difference between the Moberly/Mullenbach and the Mangeney et al. (2010) entrainment depth profiles.

As we can see with experiments from the two initial positions, the shape of the entrainment depth profile can and does vary. Our main focus was on entrainment rate, however, and should be fairly independent of the specific shape of the entrainment depth. Regardless, it is informative to understand how different boundary conditions change the entrainment depth and rate. The following section will continue with an overview of the different boundary conditions tested.

IV. Representative Cases

To better understand entrainment rate, we will focus on experiments where we measured distinct differences in entrainment. We noticed that there was a definitive change with initial position, and we expected changes with different angles of inclination and particle diameters. We therefore chose four cases to represent these boundary conditions. The four cases were: 1) an experiment at *IP1* with 0.8 mm particles at 24.0^o, referred to as Case 1; 2) an experiment at *IP1* with 2 mm particles at 23.5^o, referred to as Case 2; 3) an experiment at *IP1* with 0.8 mm particles at 23.5^o, referred to as Case 3; and 4) an experiment at *IP2* with 0.8 mm particles at 23.5^o, referred to as Case 4 (see Table 6 below). Based on net mass out, experiments at 23.5^o with 2mm particles were erosional with approximately 23.0^o as the neutral angle, and experiments at 24.0^o with 0.8 mm particles were erosional with 23.5^o being the neutral angle. All four experiments had the same aspect ratio and volume/breadth. We did not vary these two boundary conditions since we did not see any strong trends between those boundary conditions and entrainment. Figure 39 shows how entrainment rate changes with time for the four cases.

Table 6: Summary of Experimental Conditions for four representative cases

	Experiment[1]	Initial Position	θ [^{o}]	d [mm]	A_r [ ]	V/B [m^2]
Case 1	E1_0.8_24_I2	IP1	24.0	0.8	0.27	0.034
Case 2	E1_2_23.5_I3	IP1	23.5	2	0.27	0.034
Case 3	E2_27_34_1_I2	IP1	23.5	0.8	0.27	0.034
Case 4	E2_27_34_2_I1	IP2	23.5	0.8	0.27	0.034

[1] Please note that only one data set is shown for each set of conditions, even though some experiments were run multiple times under the same set of conditions.

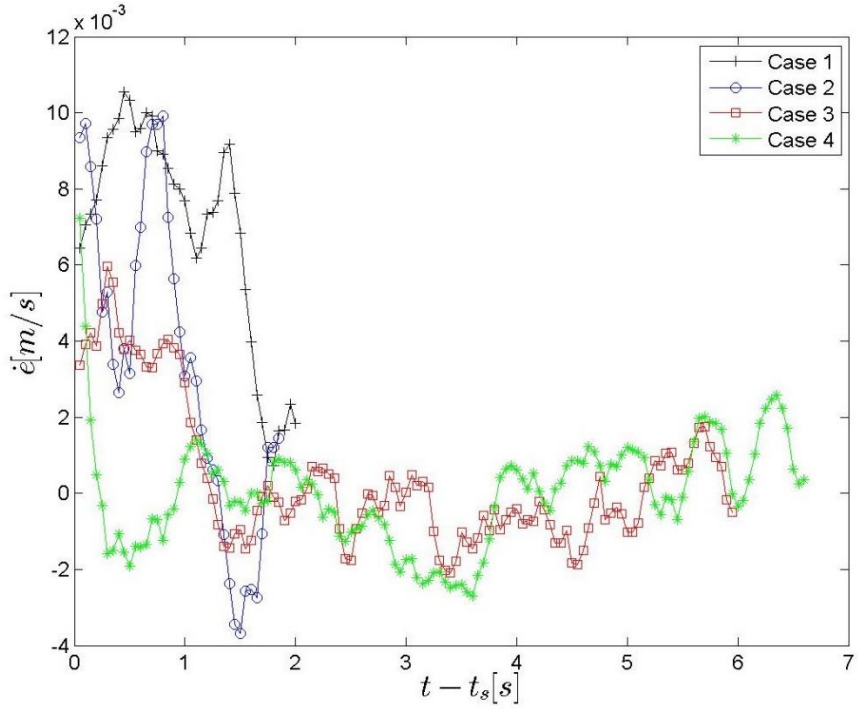

Figure 39: Entrainment rate, $\dot{e}$, as a function of time after start of flow, t-t_s, for four representative cases. Case 1 refers to the experiment with 0.8 mm particles at 24° at IP2, Case 2 refers to the experiment with 2mm particles at 23.5^o at IP1, Case 3 the experiment with 0.8 mm particles at 23.5^o at IP1, and Case 4 refers to the experiment with 0.8 mm particles at 23.5^o at IP1. These represent experiments from Table 6.

V. Shear Stress

Based on the findings of previous work (Fraccarollo and Capart 2002, Iverson 2012), we were initially interested in how shear stress related with the entrainment rate. As seen in Figure 40, shear stress increases to some maximum value and then begins to steadily decrease.

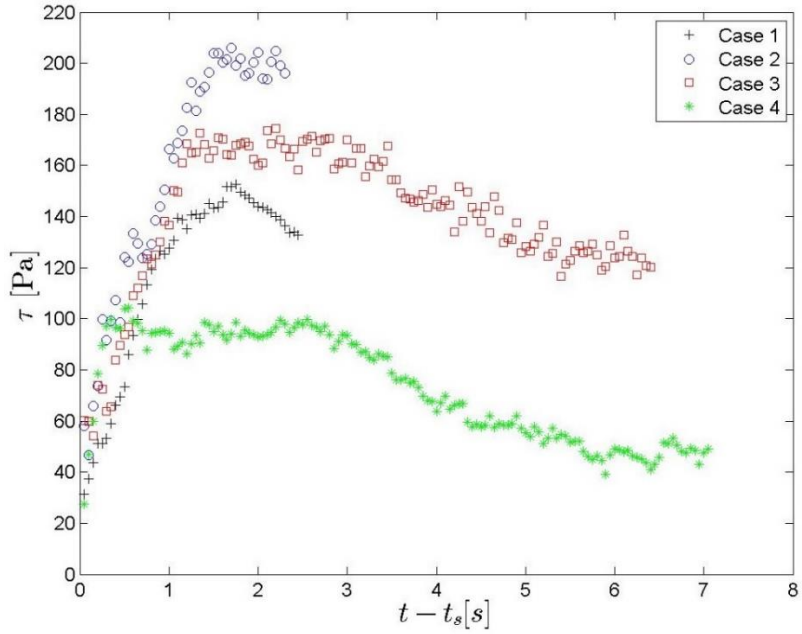

Figure 40: Shear stress, τ, versus time after front arrival, t-t_s. These represent experiments from Table 6.

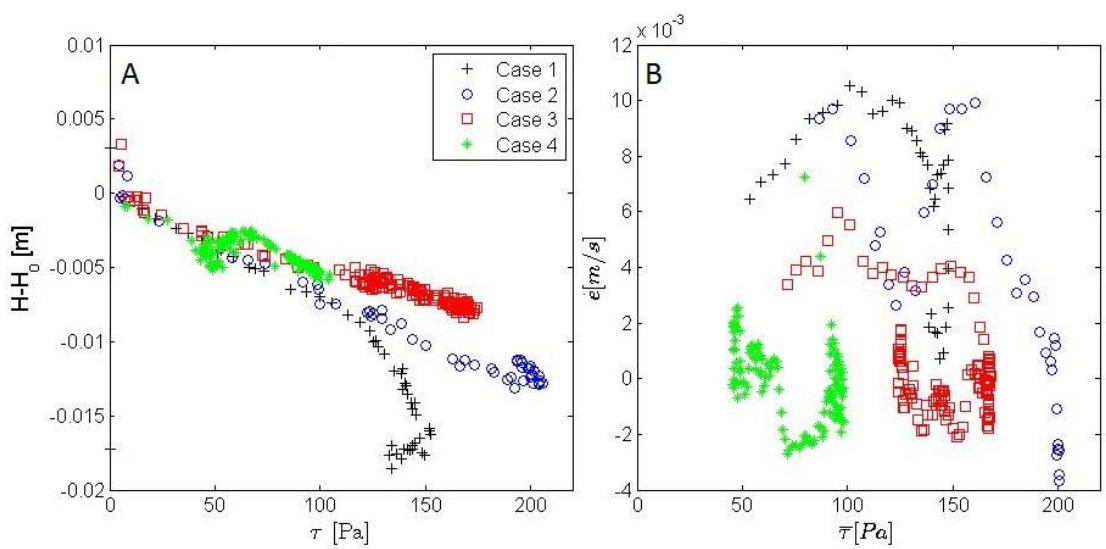

Figure 41: A normalized depth of entrainment, H-H_o, H_o is initial depth of flow, versus τ, B entrainment rate, $\dot{e}$, versus average shear stress, $\bar{\tau}$, for four representative cases. The circles highlight the early time τ values when it appears that $\dot{e}$ and τ are both increasing. These represent experiments from Table 6.

We see in Figure 41A that shear stress consistently scales negatively with depth of entrainment, which is what we might expect since a decreasing entrainment depth often

was accompanied by an increasing flow thickness, and flow thickness is directly proportional to shear stress. However, we were particularly interested in entrainment rate. In Figure 41B, we see how entrainment rate and the time-averaged shear stress related. Over the full course of the experiment, there was no clear relationship. Visual inspection suggested a clearer relationship in the first half-second after the dense flow begins, so we decided to focus in on that time period. We see in Figure 42, however, that there appeared to be a positive correlation between shear stress and entrainment for one of the cases, but not for the other experimental conditions.

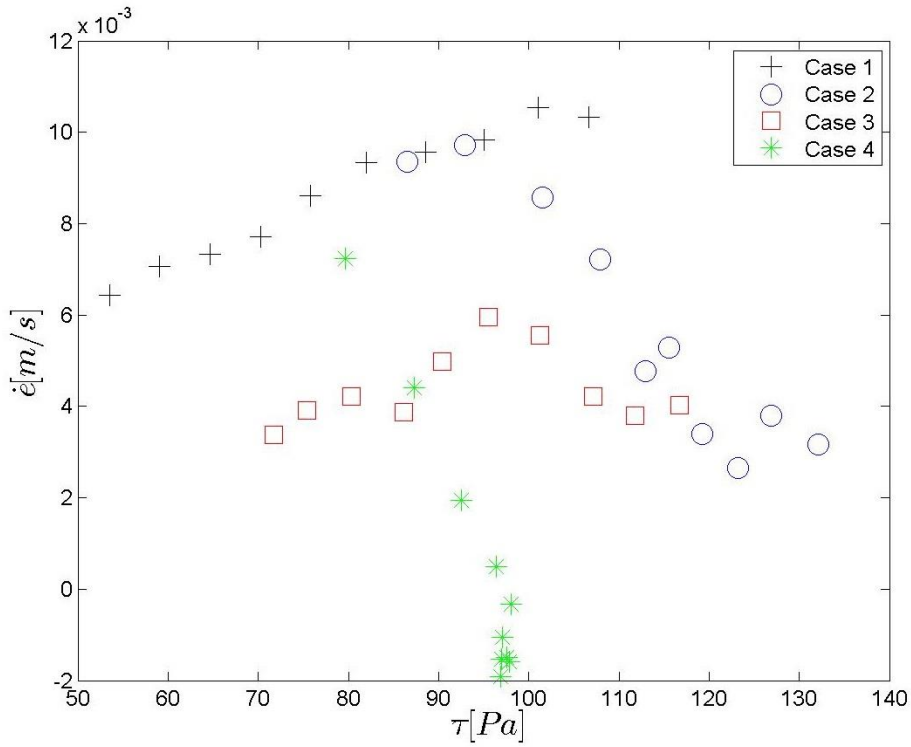

Figure 42: Entrainment rate versus average shear stress over the first half-second of the denser flow. These represent experiments from Table 6.

For the experiment at 24° (cases 1) shear stress and entrainment rate both increased, while for the other three cases shear stress increased as entrainment rate decreased or stayed roughly the same. We discuss our hypothesis as to why this behavior occurs in the discussion section.

VI. Velocity Fluctuations

In addition to shear stress, we also investigated how granular temperature and Reynolds stress varied with entrainment rate. As discussed in Chapter 3, these quantities were calculated over the full flowing layer and over just the dense portion. Figure 43 shows how these quantities vary over time. At first review, the granular temperature seemed to behave quite similarly to shear stress, with an initial increase to the maximum value, and then a steady decline. The Reynolds stress was messy, with no clear trend. The data from it are included for completion. However, we do not believe there is a relationship to dense flows, as previously suggested by Gioia et al., 2006.

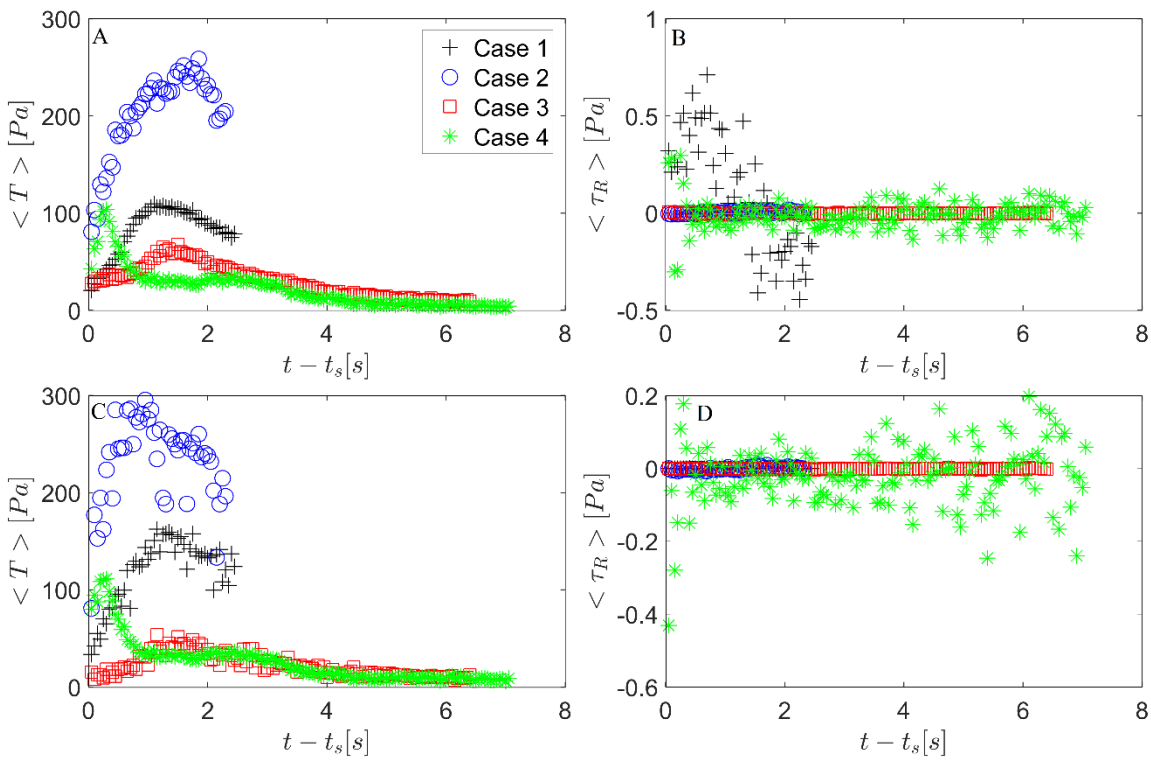

Figure 43: Granular temperature, $\langle T \rangle$, and Reynolds stress, $\langle \tau_R \rangle$, as they vary with time after the front arrival, t-t_s. A and B are considering the full flowing layer, while C and D considered just the dense portion. These represent experiments from Table 6.

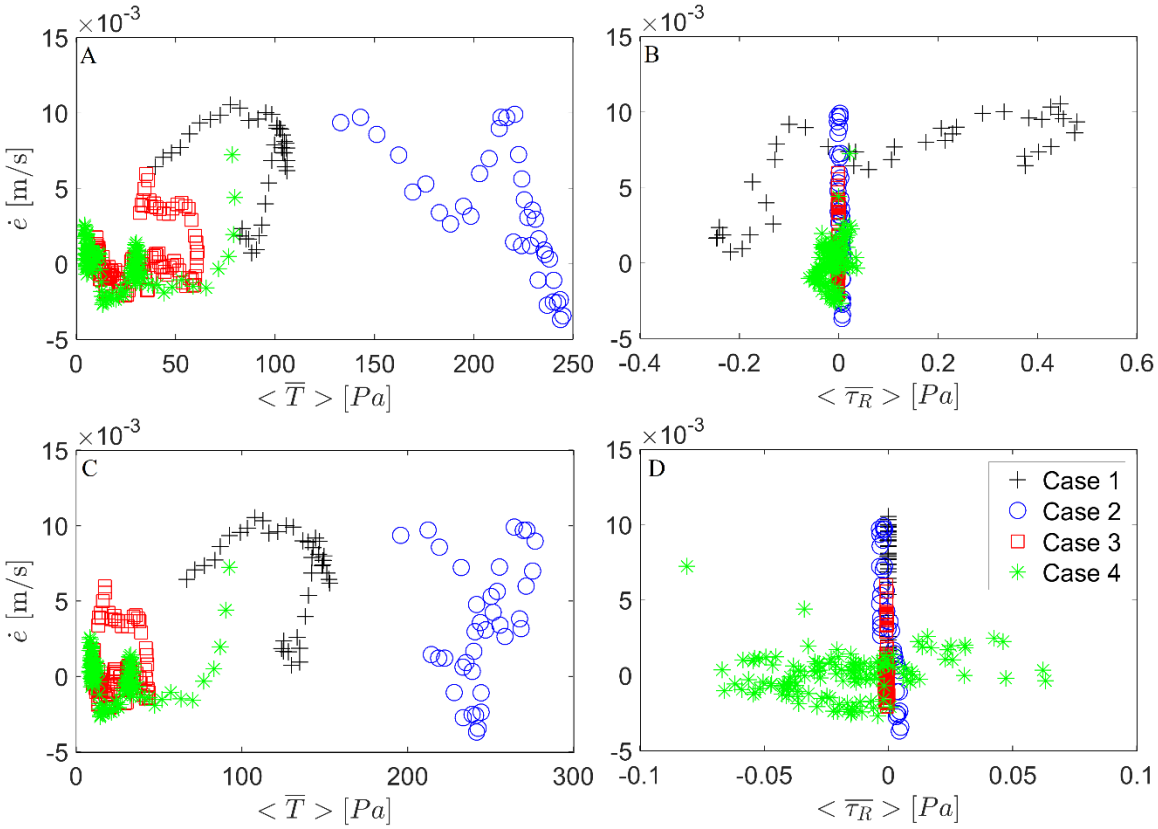

Figure 44: Parametric plots of entrainment rate, $\dot{e}$, versus A and C average granular temperature, $\langle \bar{T} \rangle$, B and D average Reynolds stress, $\langle \bar{\tau}_R \rangle$, A and B were calculated using the full flowing layer, while C and D considered just the dense portion. These represent experiments from Table 6.

In Figure 44, we see parametric plots of granular temperature and Reynolds stress with entrainment rate. When we considered the dense flowing and layer and the full flowing layer, it was difficult to make much sense of the data. Because there was not any correlation, we continued our analysis by examining the fluctuations near the interface of entrainment. As mentioned at the end of Chapter 3, we were interested in the dynamics near the interface and wanted to balance the dynamics at that interface with averaging over a sufficiently large region to minimize noise from the data. We balanced those two priorities by calculating the granular temperature and Reynolds stress over different length scales, as seen in Figure 45 for case 1. We started by looking in the region of 1 bead diameter, d, above the interface of entrainment, and increased by whole bead diameters up to approximately the maximum thickness of the dense flowing layer. For the

example shown in Figure 45, the maximum depth of the dense flowing layer was approximately 20 bead diameters or 0.016 m (see Figure 46).

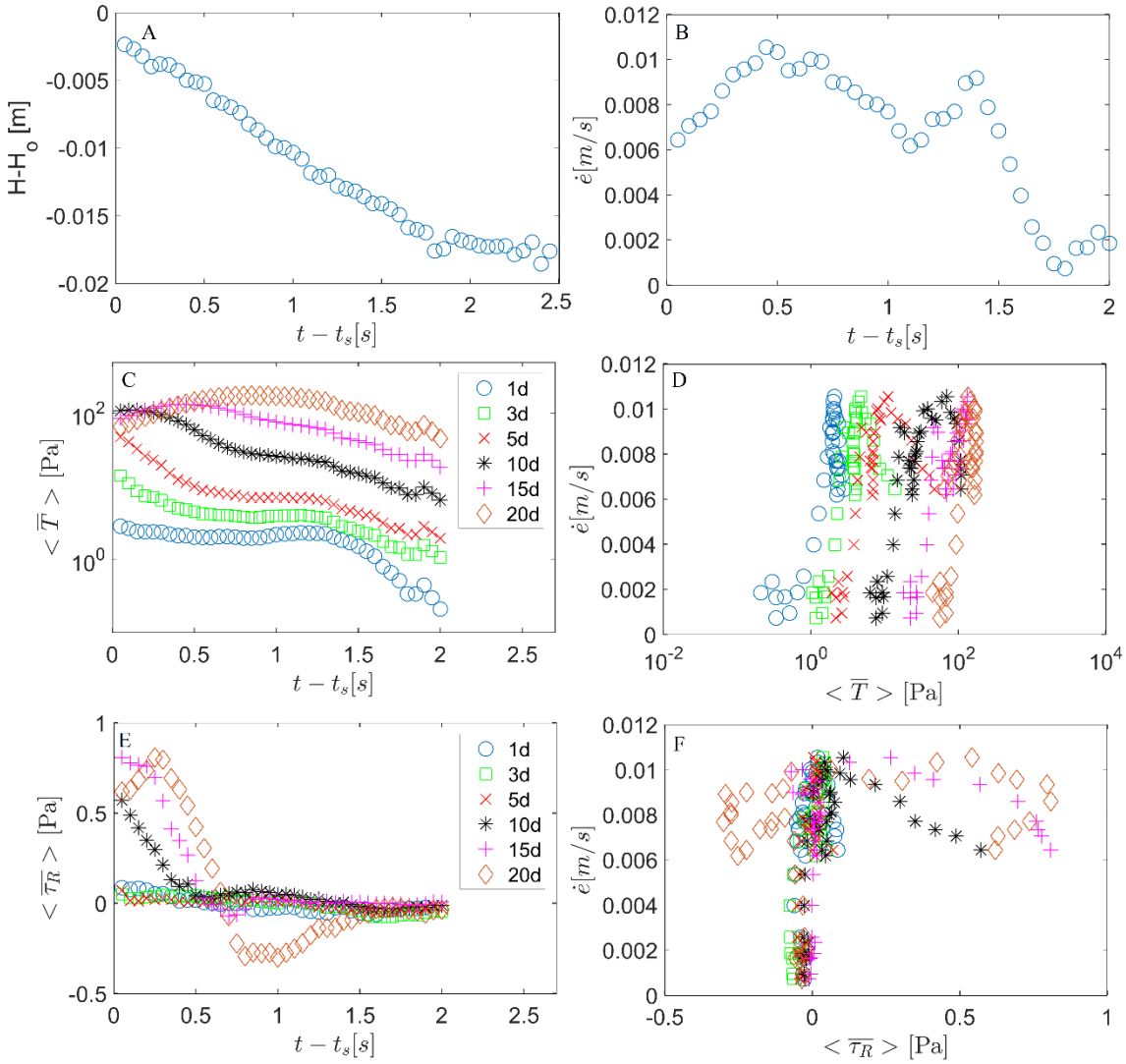

Figure 45: A normalized entrainment depth, H-H$_o$, where H$_o$ is the initial depth of the erodible bed, over time after front arrival, t-t$_s$. B entrainment rate, $\dot{e}$, over t-t$_s$. C average granular temperature, $\langle\overline{T}\rangle$, over t-t$_s$, for various length scales. D $\dot{e}$ versus $\langle\overline{T}\rangle$ for various length scales. E average Reynolds stress, $\langle\overline{\tau}_R\rangle$, over t-t$_s$, for various length scales, $\dot{e}$ versus $\langle\overline{\tau}_R\rangle$ for various length scales. Length scales are in terms number of bead diameters, d. This example is Case 1, at IP1 with 0.8 mm particles at 24°. This represents experiment E1_0.8_24_I2 from Table 6.

In Figure 45A, we see the normalized entrainment depth over time, in Figure 45B was the associated entrainment rate. Figure 45C and Figure 45E show the granular temperature

and Reynolds stress, respectively, as they varied with time over different length scales. In Figure 45D we see the parametric plots of the granular temperature over the length scales considered and entrainment rate; Figure 45F a similar parametric plot for Reynolds stress. The Reynolds stress over different length scales did not appear to scale with entrainment rate, as we expected. However, visual inspection suggested that there was a subsection of the granular temperature and entrainment rate plot (Figure 45D) that showed the possibility of a positive correlation between the two. As such, we began to look closer at how the debris flow behaved at different points in time. Particularly for experiments performed at *IP1*, we saw a sparse chaotic flow at the very beginning of an experiment. In all cases, there was a time when entrainment rate was positive, but decreasing (Figure 39). It was also observed in all cases that when the entrainment rate dropped precipitously, granular temperature was also decreasing precipitously. In Figure 47 through Figure 50, we focus in on that time frame.

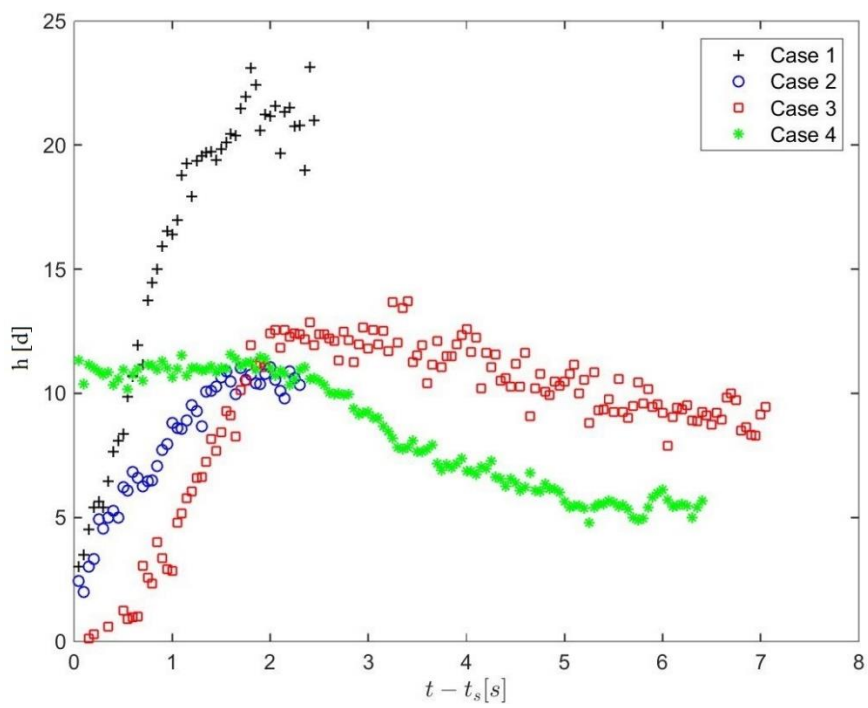

Figure 46: Thickness of dense flowing layer, h, in terms of number of bead diameters, d, from time after front arrival, t-t_s. These represent experiments from Table 6.

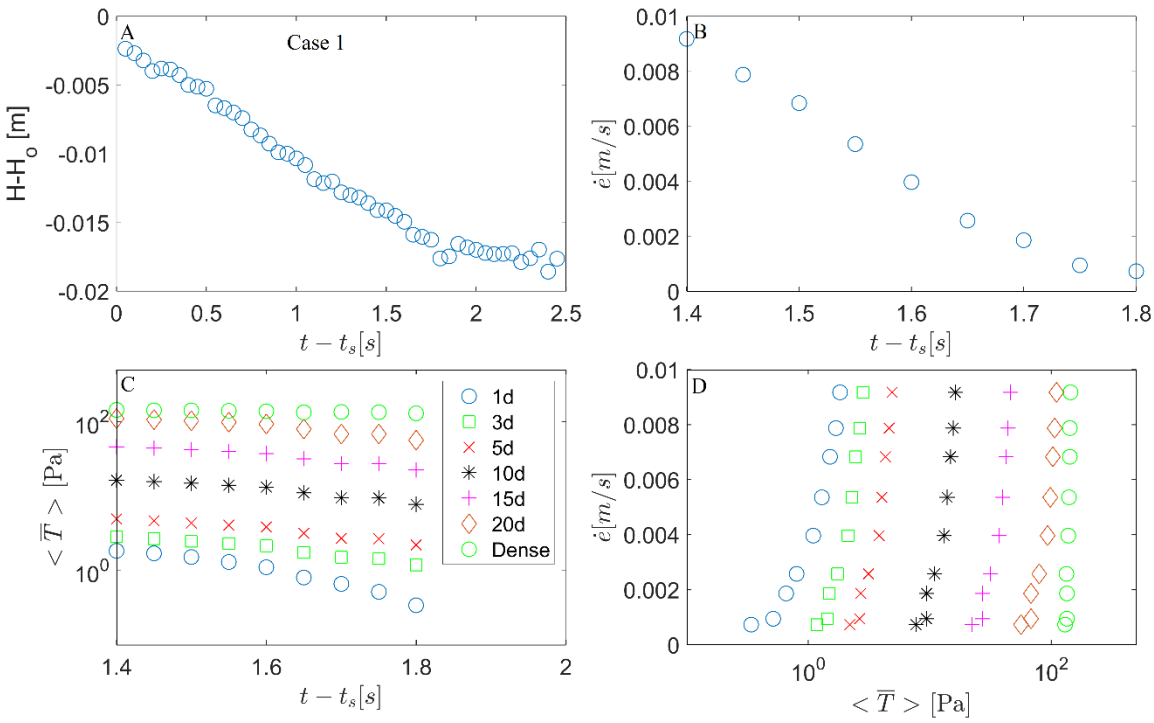

Figure 47: A normalized entrainment depth, H-H$_o$, over time after front arrival, t-t$_s$. B entrainment rate, $\dot{e}$, over time of decreasing $\dot{e}$, C average granular temperature, $\langle\overline{T}\rangle$, over time of decreasing $\dot{e}$ for various length scales. D $\dot{e}$ versus $\langle\overline{T}\rangle$ for various length scales over time of decreasing $\dot{e}$. Length scales are in terms number of bead diameters, d. Dense refers to the thickness of the dense flowing layer, which varies with time. This example is Case 1, at IP1 with 0.8 mm particles at 24°. This represents experiment E1_0.8_24_I2 from Table 6.

In Figure 47A we see the normalized entrainment depth over time. Figure 47B is the entrainment rate over the subset of time when we observed a precipitous decrease. Figure 47C shows how the granular temperature changed with time over that same subset of time. Then in Figure 47D we had the parametric plot of entrainment rate and granular temperature from the time outlined in Figures Figure 47B and Figure 47C. This same format is used for all four cases in Figure 47 through Figure 50.

There were a number of interesting details in Figure 47 through Figure 50, however our focus was on part D of each figure. This was where we saw a consistent, positive correlation for granular temperature averaged over intermediate thicknesses. We discuss

these trends in more detail in the discussion section, along with their strengths and limitations.

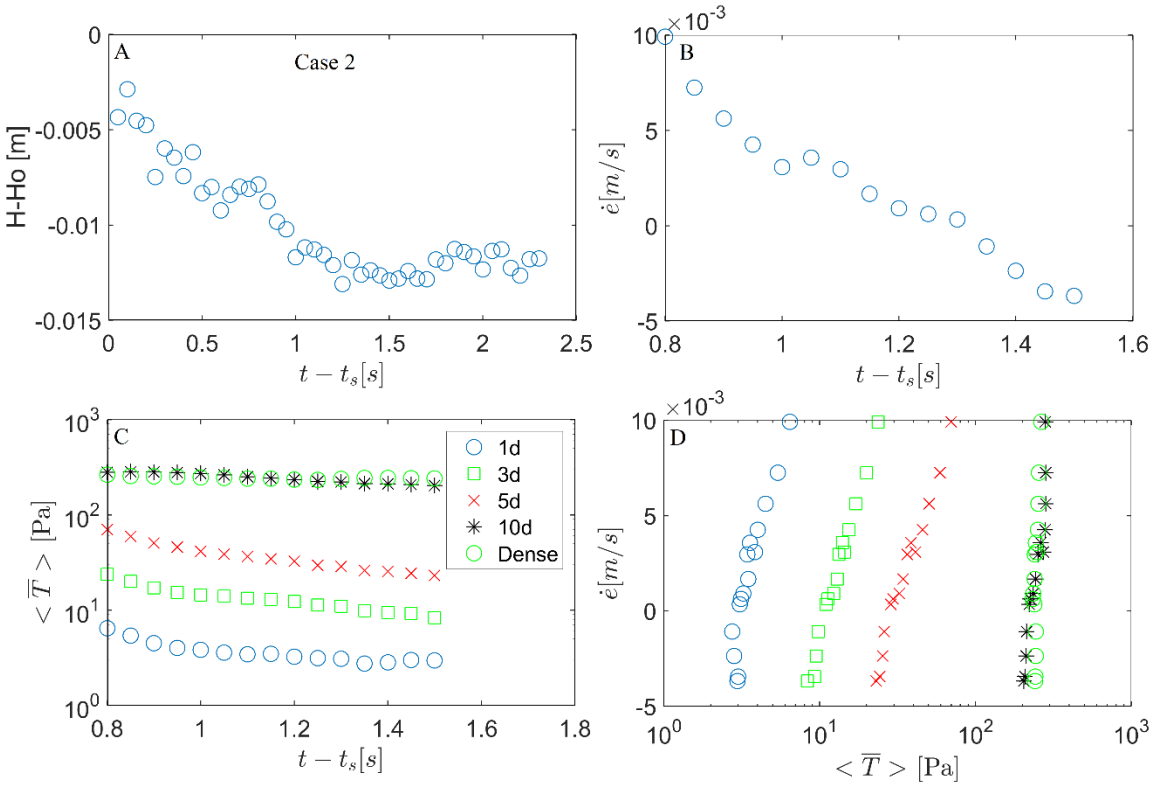

Figure 48: A normalized entrainment depth, H-H$_o$, over time after front arrival, t-t$_s$. B entrainment rate, $\dot{e}$, over time of decreasing $\dot{e}$. C average granular temperature, $\langle\overline{T}\rangle$, over time of decreasing $\dot{e}$ for various length scales. D $\dot{e}$ versus $\langle\overline{T}\rangle$ for various length scales over time of decreasing $\dot{e}$. Length scales are in terms of the number of bead diameters, d. Dense refers to the thickness of the dense flowing layer, which varies with time. This example is Case 2, at IP1 with 2 mm particles at 23.5^o. This represents experiment E1_2_23.5_I3 from Table 6.

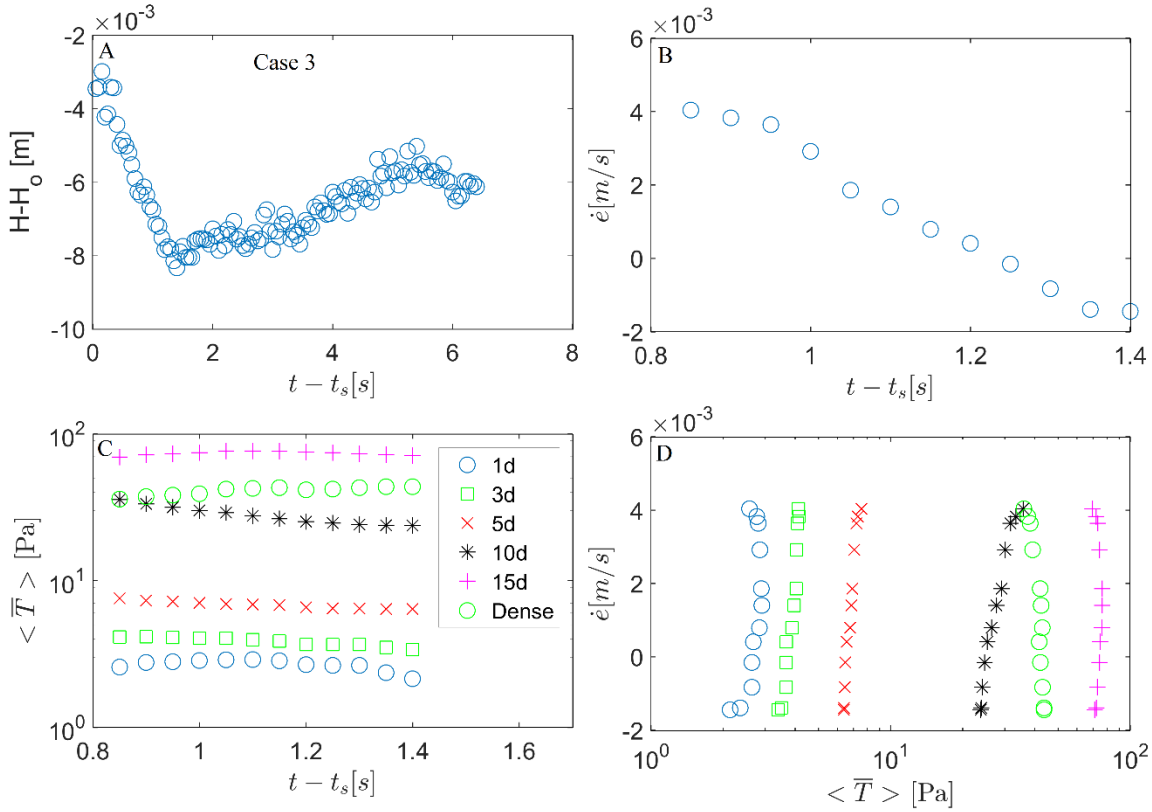

Figure 49: A normalized entrainment depth, H-H$_o$, over time after front arrival, t-t$_s$. B entrainment rate, $\dot{e}$, over time of decreasing $\dot{e}$. C average granular temperature, $\langle\overline{T}\rangle$, over time of decreasing $\dot{e}$ for various length scales. D $\dot{e}$ versus $\langle\overline{T}\rangle$ for various length scales over time of decreasing $\dot{e}$. Length scales are in terms of the number of bead diameters, d. Dense refers to the thickness of the dense flowing layer, which varies with time. This example is Case 3, at IP1 with 0.8 mm particles at 23.5^o. This represents experiment E2_27_34_1_I2 from Table 6.

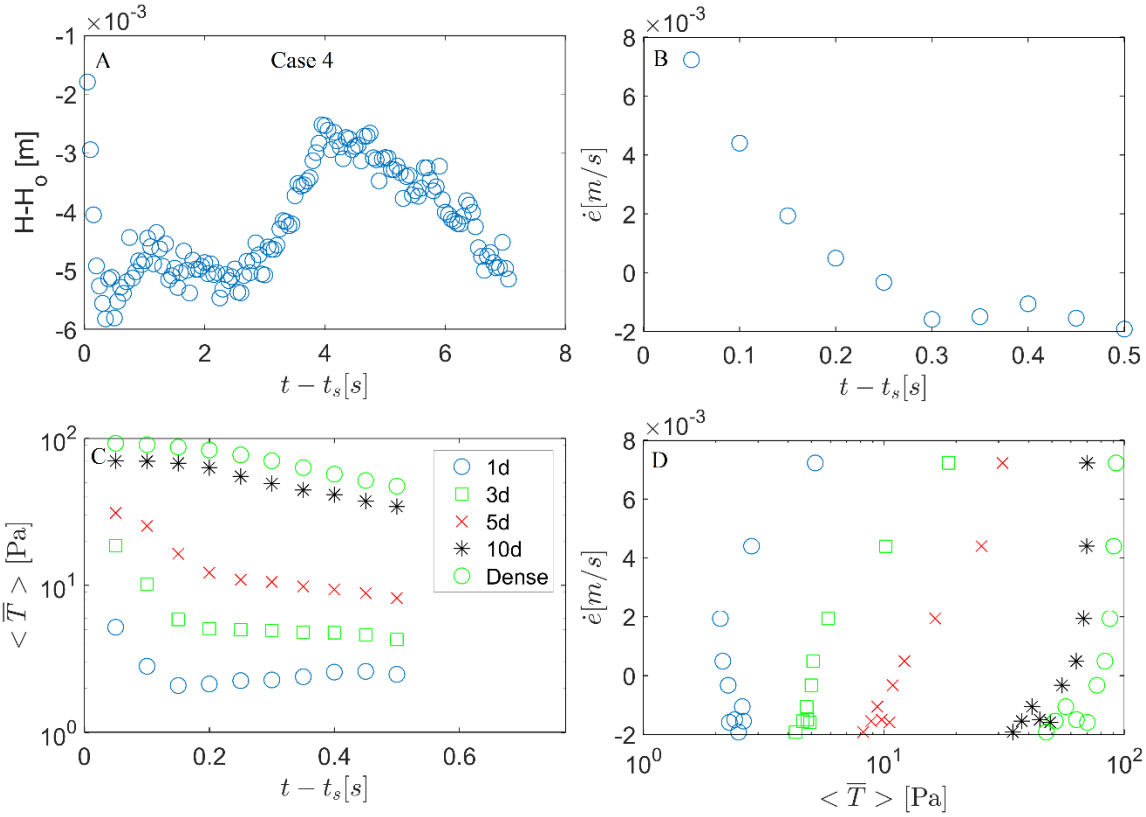

Figure 50: A normalized entrainment depth, H-H$_o$ over time after front arrival, t-t$_s$. B entrainment rate, $\dot{e}$, over time of decreasing $\dot{e}$. C average granular temperature, $\langle\overline{T}\rangle$, over time of decreasing $\dot{e}$ for various length scales. D $\dot{e}$ versus $\langle\overline{T}\rangle$ for various length scales over time of decreasing $\dot{e}$. Length scales are in terms of the number of bead diameters, d. Dense refers to the thickness of the dense flowing layer, which varies with time. This example is Case 4, at IP2 with 0.8 mm particles at 23.5^o. This represents experiment E2_27_34_2_I1 from Table 6.

VII. Discussion

We have discussed the various boundary conditions for experiments and the trends that we have seen in the data. We have examined the behavior of internal mechanisms, such as shear stress, for four example data sets that represent the variety of boundary conditions, and commented on the trends there. In this section, we will now discuss the robustness of these trends and review our primary conclusions.

VII A. Boundary Conditions

Of the various boundary conditions we used, the only external conditions that showed a strong and relatively consistent correlation with entrainment rate were the angle of inclination and initial position. We saw a general trend that as the angle of inclination increased, so did the net erosion, and instantaneous entrainment depth and entrainment rate. This was consistent with the framework proposed by Egashira et al. (2001) and Papa et al. (2004). Specifically, we found that there is a "neutral" angle. When debris flows occur at angles greater than the neutral angle, they will result in erosion to return the erodible bed neutral angle. Similarly, at angles below the neutral angle, debris flows will deposit to return the erodible bed to the neutral angle. However, there are limitations to this framework, for example even with slight changes in the angle of inclination; we see dramatic changes in entrainment rates. Still, it was important to note that there is clearly a trend between the angle of inclination and the entrainment rate.

The second boundary condition that played a role was the initial position, *IP*, of the debris flow. As previously mentioned, *IP1* had conditions similar to a real debris flow, while *IP2* was more similar to a granular physics problem. For experiments at *IP1*, when the supply was released upstream of a rigid rough section, we see the entrainment depth steadily decreasing to a maximum depth and then beginning to increase. At *IP2*, when the supply was released much closer to the erodible bed, maximum entrainment depth occurred much sooner, and was much shallower than the same experiment at *IP1*. We suspect this is associated with the manner in which flow evolved before reaching the

erodible bed. The duration of the erosion event was longer by necessity for the experiment at *IP1*, since the debris flow spreads out as it flows over the rigid section. Despite having very different maximum entrainment depths, both conditions seem to have comparable maximum entrainment rates.

We were interested in how our experimental results compared with those from other comparable experimental conditions, in particular the work by Mangeney et al. (2010) and Farin et al. (2014). In reviewing their work, we noticed differences in the entrainment depth profile, which were primarily a function of the distance downstream of the debris flow initiation point that we calculated the entrainment depth. Despite slightly different boundary conditions, we still see the same general behavior for the depth of entrainment.

Particle size, aspect ratio, and volume/breadth of the supply did not show any consistent trends. While aspect ratio and volume/breadth of the supply are important to consider for the experiment setup, in a natural debris flow setting, they will likely not play a significant role, since most natural debris flows begin over a rigid base and then reach erodible material (e.g. conditions in Stock and Dietrich, 2006; Iverson et al., 2010; McCoy et al., 2012, 2013).

VII B. Shear Stress

The first physical mechanics we investigated was shear stress. As we reviewed, a number of other studies suggested this was an underlying mechanism for entrainment. However, we did not see a consistent relationship between shear stress and entrainment rate. During the first half-second after the beginning of the dense flow, we saw a positive relationship between entrainment rate and shear stress for one of the cases, and negative for other three. When we tried to understand why this case was different from the others, we noticed that all conditions showed an increase in shear stress at the beginning. However, if we look back to Figure 39, for most cases the entrainment rate was not consistently increasing. This appears to suggest no real physical correlation between shear stress and entrainment, just a coincidence that both were increasing for case 1.

In this time frame, shear stress and the thickness of the dense layer is increasing for all cases, suggesting that many of the particle-particle interactions near the interface of entrainment were friction dominated. However, we do not see a consistent relationship between shear stress and entrainment rate over this time frame.

We see that, in the instance when we do see a positive relationship, it was for an experiment with 0.8 mm particles at *IP1*. We know that for experiments at initial position one, there was an initial sparse front as the debris flow supply travels down and spreads out along the rigid bed. This prolonged exposure to the energetic front could perhaps prepare the erodible bed for entrainment. We do know from the work by Hill et al. (2013) that the erodible bed became more susceptible to erosion as the bed became more organized. For the experiments at initial position two, this initial sparse phase was almost non-existent, and the lack of this energetic period could be part of the reason why we did not see increasing entrainment rates in the first half-second after the start of the dense flow. For experiments with the 2 mm particles, we also consistently see an initial decrease in entrainment rate, the reason for which is unknown. However, these results are not definitive, and require further investigation to understand the underlying mechanics.

To relate this to other works, we can look back at the relationship suggested by Iverson (2012). Based on the schematic in Figure 3, Iverson (2012) related entrainment rate, $\dot{e}$, at the interface of layers 1 and 2 with Equation 2. This expression suggests that entrainment rate is proportional to the excess shear stress, $\tau_{1_{bottom}} - \tau_{2_{top}}$. Our analysis focused on measuring the entrainment rate at that same location. For our system, we are making a similar assumption to that proposed by Savage and Hutter (1989) and used by Mangeney-Castelnau et al. (2005) in using the Saint-Venant equations in the context of a debris flow and assuming that a basal stress was dominating, making our expression for shear stress equivalent to Iverson's excess shear stress (2012). Since we do not see any discontinuity in the velocity profile, or any basal slip velocity, it is not immediately clear how to apply this expression by Iverson (2012). One possibility will be to set $v_{2_{top}}$ equal to zero, and

take an average velocity of the dense flowing layer, $\bar{u}_{dense}$, to be $v_{1_{bottom}}$, making Equation 2 the following:

$$\dot{e} = E = \frac{\tau}{\rho(\bar{u}_{dense})} \qquad 18$$

However, this will be sensitive to how we define the flowing layer and will require further parametric studies, and is therefore beyond the scope of this thesis.

VII C. Granular Temperature

The investigation of granular temperature shows that the strongest indicator of the underlying mechanics for part of the entrainment rate dynamics occurs after the initially strong entrainment rate begins to decrease perceptively. During this time, granular temperature is positively correlated with entrainment rate for all the cases we investigated. Admittedly, this is a limited time period. However, it is significant that this correlation occurred in different parts of the flow. In the case of experiments at initial position one, this happens a short time after the initially sparse front has passed, when the flow becomes denser and entrainment rate begins to steadily decrease. For the case at initial position two, 6almost immediately after the debris flow begins, the flow becomes denser, and the entrainment rate begins to steadily decrease.

This positive relationship varies over the different length scales, as seen in Figure 47 through Figure 50. To understand this, we needed to examine the length scales considered. The smallest length was one particle diameter, which might not be a large enough length scale to average over due to the noisy nature of our data. When we considered the full thickness of the dense layer, or thickness close to it, we sometimes saw a negative relationship between entrainment rate and granular temperature. Since the granular temperature was averaged, when we consider a thicker layer, details about the behavior close to the interface where entrainment is occurring may be lost. Because of this, we are most interested in the behavior of granular temperature averaged over a thickness of 3-5 particle diameters above that interface.

Upon further inspection of the relationship between entrainment rate and granular temperature, we observed that for many of the length scales in the four cases the curve seemed exponential. As such, we began investigating a functional relationship between the two, partially inspired by the format proposed by Iverson (2012), of entrainment rate scaling with a stress divided by velocity. This suggested the following relationship between entrainment rate and granular temperature:

$$\dot{e}_c = [\dot{e}_1 * exp(\langle\bar{T}\rangle/(\rho_m\langle V^2\rangle))] * h_c \ , \tag{19}$$

$$\langle V^2\rangle = \overline{u^2 + v^2}, \tag{20}$$

where $\dot{e}_c$ was the calculated entrainment rate, $\dot{e}_1$ was the measured entrainment rate when entrainment rate first begins to decrease, $\langle\bar{T}\rangle$ was the average granular temperature, ρ_m, the material density, V the average velocity, u was the horizontal velocity, v the vertical velocity, and h_c was the average thickness of the layer we are measuring granular temperature over normalized by the thickness of the dense layer. Using this expression, we compare the calculated entrainment rate with the entrainment rate we measured in our four representative cases over the length scales of three and five bead diameters (see Figure 51 through Figure 54).

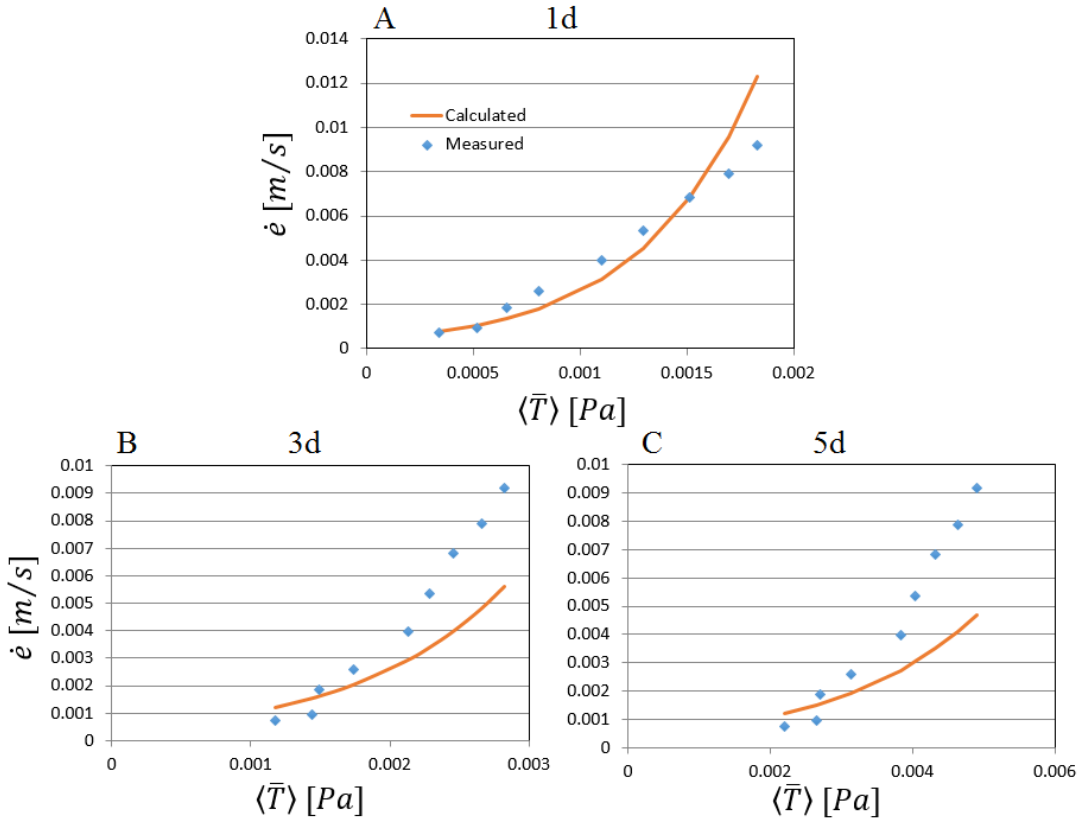

Figure 51: A, calculated and measured entrainment rate, $\dot{e}$, vs average granular temperature, $\langle \bar{T} \rangle$, for Case 1 averaged over one bead diameter, B averaged over three bead diameters, and C averaged over five bead diameters. This represents experiment E1_0.8_24_I2 from Table 6.

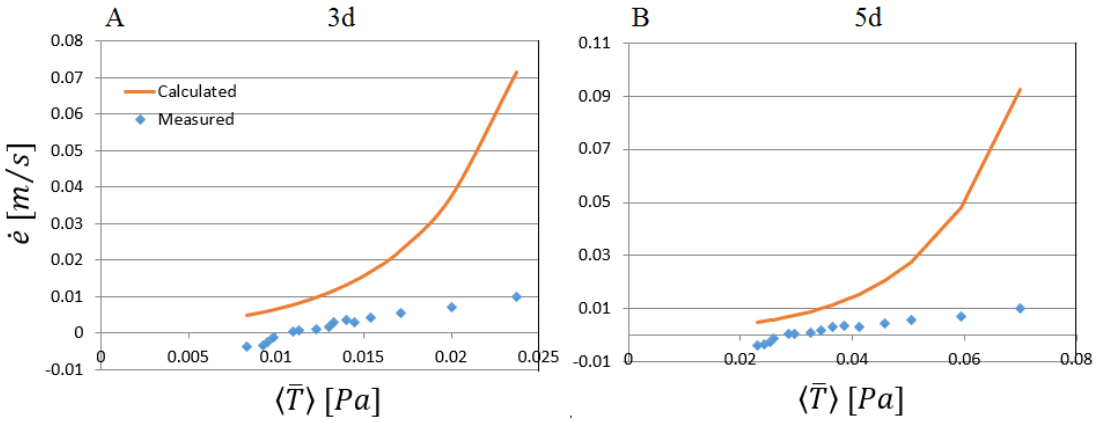

Figure 52: A, calculated and measured entrainment rate, $\dot{e}$, vs average granular temperature, $\langle \bar{T} \rangle$, for Case 2 averaged over three bead diameters, and B averaged over five bead diameters. This represents experiment E1_2_23.5_I3 from Table 6.

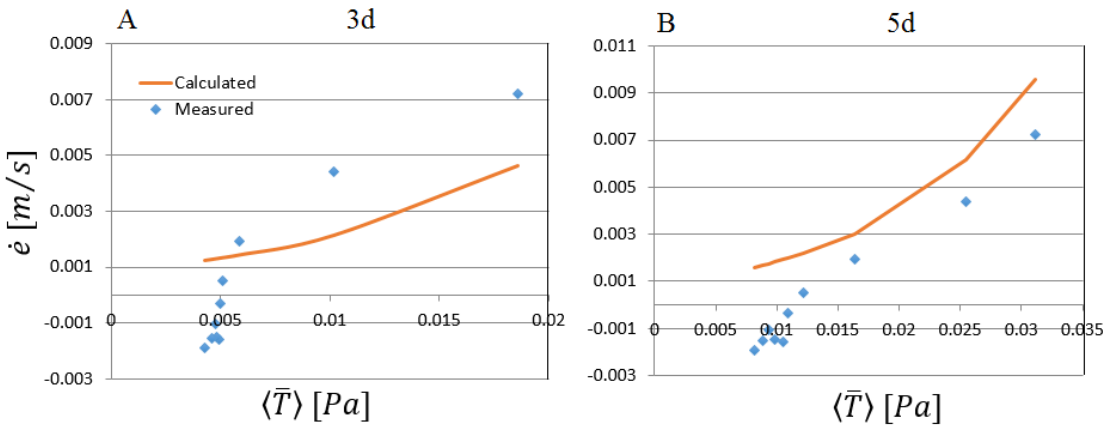

Figure 53: A, calculated and measured entrainment rate, $\dot{e}$, vs average granular temperature, $\langle\bar{T}\rangle$, for Case 3 averaged over three bead diameters, and B averaged over five bead diameters. This represents experiment E2_27_34_1_I2 from Table 6.

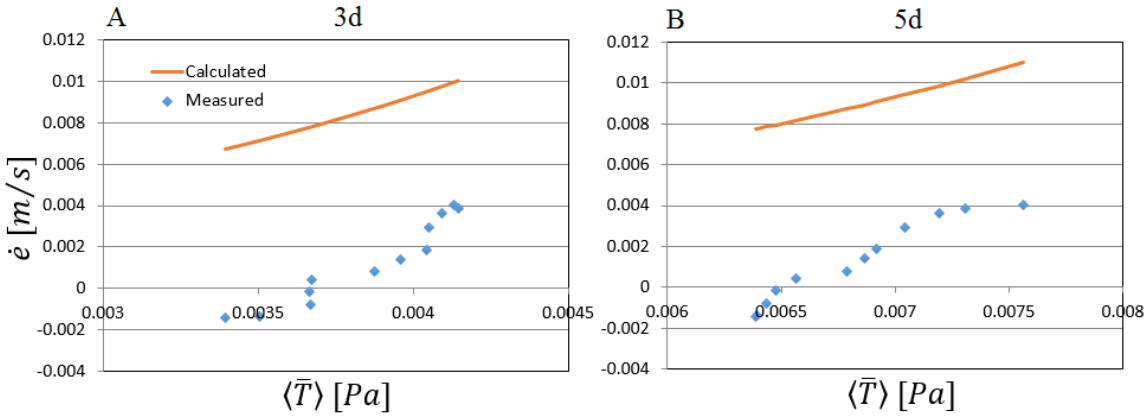

Figure 54: A, calculated and measured entrainment rate, $\dot{e}$, vs average granular temperature, $\langle\bar{T}\rangle$, for Case 4 averaged over three bead diameters, and B averaged over five bead diameters. This represents experiment E2_27_34_2_I1 from Table 6.

For the different cases, the match between data and the expression in Equation 19 varies. By visual inspection, Figure 51 and Figure 53 seem to have the strongest agreement between the data and expression from Equation 19. These are from cases 1 and 3, which are both experiments at initial position one, with 0.8 mm particles. The only difference is that case 1 is at an angle of 24°, while case 3 is at 23.5°. In Figure 52, we see case 2, the representative case for the 2 mm particles where the agreement was suboptimal,

particularly at higher granular temperatures. As granular temperature increases, entrainment rate increases for the data, but not as fast as Equation 19 predicted. There are a number of possible reasons for this. One possible reason for this could be that the correct scaling is not a ratio of granular temperature to the average velocity squared, $\langle \bar{T} \rangle / \rho_m \langle V^2 \rangle$. That is, 2mm particles typically have a considerably higher temperature relative to their average downstream velocity than 0.8mm particles (e.g., Hill et al., 2003; Gioia et al., 2005). Even if temperature is driving entrainment of these systems, perhaps the ratio $\langle \bar{T} \rangle / (\rho_m \langle V^2 \rangle)$ is not accounting for that difference in granular temperatures properly in the affect they have on entrainment. Instead, the appropriate scaling for temperature may be a different velocity (or energy or stress scale). Further work is needed to determine the exact scaling.

Another outlier involves case 4 data: we see in Figure 54 the calculated rate seemed to have roughly the correct shape for the entrainment rate, but Equation 19 gives values consistently larger than what we saw in the measured data. We should recall that case 4 was the example at the initial position two, where the initial sparse phase seen in the other three cases was almost non-existent. As suggested in our discussion about shear stress, the lack of this energetic period to “prepare” the erodible bed could be affecting the relationship for this case. Another effect of the release at initial position two is that the flow was denser than in experiments at initial position one. In a denser flow, frictional stress can play a more significant role than in the cases with sparser flows where we see Equation 19 having better agreement with measured data.

While it is unclear exactly the physical meaning behind this expression, the data do suggest that there is some consistent relationship between granular temperature and entrainment rate. It should also be noted that no additional fitting parameters were used beyond the expression suggested in Equation 19.

Chapter 5: Summary and Outlook

To summarize the primary activities described in this thesis:

We performed laboratory scale debris flow experiments under a select set of boundary conditions to investigate entrainment by debris flows and the underlying mechanics. These boundary conditions included the angle of inclination, particle diameter, initial position, and the dimensions of the supply (i.e., aspect ratio and volume/breadth). Using high-speed video and a series of programs compatible with MATLAB, we were able to analyze the flow and measure the depth and rate of entrainment, among other quantities of interest. These were the first experiments of their kind that used high-resolution images to relate dynamics commonly associated with debris flow entrainment to near-instantaneous entrainment rates.

We isolated each boundary condition to investigate its effect on entrainment depth and rate and found that the angle of inclination and the initial position were the most influential external conditions. Increasing the angle of inclination led to increasing entrainment depths and rates. Release of the debris flow from a position far upstream of an erodible bed (here, *IP1*) resulted in deeper entrainment depths and a longer entrainment duration than a debris flow released directly upstream of the erodible bed (here, *IP2*), but both had comparable entrainment rates.

To understand the mechanisms behind entrainment, we calculated the shear stress, granular temperature, and Reynolds shear stress in each experiment. We did not find any definitive relationships between shear stress and entrainment rate. Reynolds stress did not suggest any trends. Granular temperature had a positive relationship with entrainment rate when entrainment rate decreased after the beginning of the dense phase of the debris flow. Further investigation of that relationship led to a mathematical formulation of the correlation between entrainment rate and granular temperature. Our results suggested that, at different times, different dynamics dominate the debris flow process. Untangling these dynamics is a significant portion of the work moving forward. The work done in

this thesis is laying the groundwork for progressing forward with that process in the future.

In looking towards future work, there are a number of possible avenues of study. For this thesis, a considerable amount of data was collected, and one of the next major steps would be to do conditional averaging between experiments. As has been mentioned throughout this thesis, these data involve a lot noise, which in many instances is difficult to sort out and provides a challenge to understanding the mechanisms governing entrainment. With the data from duplicate experiments, conditional averaging would help to help reduce that noise and allow us to delve further and with more certainty into some of the relationships observed thus far.

Further work is needed to understand the relationship between granular temperature and entrainment rate. The expression proposed in Equation 19 sets forth a reasonable relationship between entrainment rate and granular temperature. However, as was brought up in Chapter 4, Section VII C. Granular Temperature, it is far from a perfect fit with the measured data for the four cases examined. Analysis to determine the appropriate scaling for the granular temperature and to investigate the reason for an exponential relationship are just two of many further undertakings needed.

More study is also needed to understand the relationship between shear stress and entrainment rate. The results collected thus far will provide a starting point to direct future investigation, particularly parametric studies to explore the expression proposed in Equation 18. Another aspect to analyze would be the pressure collected with the basal force plate. While we collected the data from both the pore pressure and basal force sensors in the debris flow flume for this thesis, we were not able to begin analyzing it. Many studies in the field have taken similar data to try to understand shear stress, and it could be important to see how the basal stress affects shear stress and, possibly, entrainment.

Going beyond the boundary conditions used in this thesis also offers other possible avenues of interest. One of the downsides of this particular flume is the width. The

narrowness of the flume is helpful in making the assumption of pseudo 2-dimensional flow; it restricts other behaviors due to lateral variation often seen in natural debris flows. A wider flume would allow for features such as fingering and to investigate scaling laws, which would be important for the application of theories to larger scales. Future experiments involving mixtures of particles and particles with fluids will also be important steps in understanding entrainment and debris flows.

Bibliography

Berger, C., B. W. McArdell, and F. Schlunegger (2011), Direct measurement of channel erosion by debris flows, Illgraben, Switzerland, *J. Geophys. Res. Earth Surf.*, *116*(1), 1–18, doi:10.1029/2010JF001722.

Berti, M., R. Genevois, R. Lahusen, A. Simoni, and P. R. Tecca (2000), Alps) in the Acquabona Watershed on the Dolomites (Italian, , *25*(9), 707–715.

Blair, D., and E. Dufresne (2008), MATLAB Particle Tracking, *Georg. Phys.* Available from: http://site.physics.georgetown.edu/matlab/ (Accessed 16 June 2015)

Bouchaud, J.-P., M. E. Cates, J. R. Prakash, and S. F. Edwards (1994), A model for the dynamics of sandpile surfaces, *J. Phys. I*, *4*(10), 1383–1410, doi:10.1051/jp1:1994195.

Capart, H., and D. L. Young (1998), Formation of a jump by the dam-break wave over a granular bed, *J. Fluid Mech.*, *372*, 165–187, doi:10.1017/S0022112098002250.

Egashira, S., N. Honda, and T. Itoh (2001), Experimental study on the Entrainement of bed material into debris flow, *Phys. Chem. Earth, Part C Solar-Terrestrial Planet. Sci.*, *26*(9), 645–650.

Farin, M., A. Mangeney, and O. Roche (2014), Fundamental changes of granular flow dynamics, deposition, and erosion processes at high slope angles: Insights from laboratory experiments, *J. Geophys. Res. Earth Surf.*, *119*(3), 504–532, doi:10.1002/2013JF002750.

Floris, M., a. D'Alpaos, C. Squarzoni, R. Genevois, and M. Marani (2010), Recent changes in rainfall characteristics and their influence on thresholds for debris flow triggering in the Dolomitic area of Cortina d'Ampezzo, north-eastern Italian Alps, *Nat. Hazards Earth Syst. Sci.*, *10*(3), 571–580, doi:10.5194/nhess-10-571-2010.

Forterre, Y., and O. Pouliquen (2008), Flows of Dense Granular Media, *Annu. Rev. Fluid Mech.*, *40*(1), 1–24, doi:10.1146/annurev.fluid.40.111406.102142.

Fraccarollo, L., and H. Capart (2002), Riemann wave description of erosional dam-break flows, *J. Fluid Mech.*, *461*, 183–228, doi:10.1017/S0022112002008455.

Frey, P., and M. Church (2011), Bedload: A granular phenomenon, *Earth Surf. Process. Landforms*, *36*(1), 58–69, doi:10.1002/esp.2103.

Gioia, G., S. E. Ott-Monsivais, and K. M. Hill (2006), Fluctuating velocity and momentum transfer in dense granular flows, *Phys. Rev. Lett.*, *96*(13), 7–10, doi:10.1103/PhysRevLett.96.138001.

Hill, K. M., G. Gioia, and V. V Tota (2003), Structure and kinematics in dense free-surface granular flow., *Phys. Rev. Lett.*, *91*(6), 064302, doi:10.1103/PhysRevLett.91.064302.

Hill, K. M., L. Maki, and R. Kaitna (2013), *Particle-Scale Controls on Entrainment and Deposition due to Debris Flows*.

Hungr, O., S. Mcdougall, and M. Bovis (2005), Entrainment of Material by Debris Flows, *Debris-Flow Hazards Relat. Phenom.*, 135–155.

Hürlimann, M., D. Rickenmann, and C. Graf (2003), Field and monitoring data of debris-flow events in the Swiss Alps, *Can. Geotech. J.*, *40*(1), 161–175, doi:10.1139/t02-087.

Hussin, H. Y., B. Quan Luna, C. J. Van Westen, M. Christen, J. P. Malet, and T. W. J. Van Asch (2012), Parameterization of a numerical 2-D debris flow model with entrainment: A case study of the Faucon catchment, Southern French Alps, *Nat. Hazards Earth Syst. Sci.*, *12*(10), 3075–3090, doi:10.5194/nhess-12-3075-2012.

Iverson, R. M. (1997), The physics of debris flows, *Rev. Geophys.*, *35*(3), 245, doi:10.1029/97RG00426.

Iverson, R. M. (2012), Elementary theory of bed-sediment entrainment by debris flows and avalanches, *J. Geophys. Res. Earth Surf.*, *117*(3), 1–17, doi:10.1029/2011JF002189.

Iverson, R. M., and J. W. Vallance (2001), New views of granular mass flows, *Geology*, *29*(2), 115–118, doi:10.1130/0091-7613(2001)029<0115:NVOGMF>2.0.CO.

Iverson, R. M., M. Logan, R. G. LaHusen, and M. Berti (2010), The perfect debris flow? Aggregated results from 28 large-scale experiments, *J. Geophys. Res.*, *115*(F3), doi:10.1029/2009JF001514.

Iverson, R. M., M. E. Reid, M. Logan, R. G. LaHusen, J. W. Godt, and J. P. Griswold (2011), Positive feedback and momentum growth during debris-flow entrainment of wet bed sediment, *Nat. Geosci.*, *4*(2), 116–121, doi:10.1038/ngeo1040.

Jakob, M., and P. Friele (2010), Frequency and magnitude of debris flows on Cheekye River, British Columbia, *Geomorphology*, *114*(3), 382–395, doi:10.1016/j.geomorph.2009.08.013.

Jomelli, V., D. Brunstein, M. Déqué, M. Vrac, and D. Grancher (2009), Impacts of future climatic change (2070-2099) on the potential occurrence of debris flows: A case study in the Massif des Ecrins (French Alps), *Clim. Change*, *97*(1), 171–191, doi:10.1007/s10584-009-9616-0.

Jop, P., Y. Forterre, and O. Pouliquen (2007), Initiation of granular surface flows in a narrow channel, *Phys. Fluids*, *19*(8), doi:10.1063/1.2753111.

King, J. (1996), Tsing Shan debris flow, *Spec. Proj. Rep. SPR*.

Mangeney, a., O. Roche, O. Hungr, N. Mangold, G. Faccanoni, and a. Lucas (2010), Erosion and mobility in granular collapse over sloping beds, *J. Geophys. Res. Earth Surf.*, *115*(3), 1–21, doi:10.1029/2009JF001462.

Mangeney, A. (2011), Geomorphology: Landslide boost from entrainment, *Nat. Geosci.*, *4*(2), 77–78, doi:10.1038/ngeo1077.

Mangeney, A., L. S. Tsimring, D. Volfson, I. S. Aranson, and F. Bouchut (2007), Avalanche mobility induced by the presence of an erodible bed and associated entrainment, *Geophys. Res. Lett.*, *34*(22), 1–5, doi:10.1029/2007GL031348.

Mangeney-Castelnau, a., F. Bouchut, J. P. Vilotte, E. Lajeunesse, a. Aubertin, and M. Pirulli (2005), On the use of Saint Venant equations to simulate the spreading of a granular mass, *J. Geophys. Res. B Solid Earth*, *110*(9), 1–17, doi:10.1029/2004JB003161.

McCoy, S. W., J. W. Kean, J. a. Coe, G. E. Tucker, D. M. Staley, and T. a. Wasklewicz (2012), Sediment entrainment by debris flows: In situ measurements from the headwaters of a steep catchment, *J. Geophys. Res. Earth Surf.*, *117*(3), 1–25, doi:10.1029/2011JF002278.

McCoy, S. W., G. E. Tucker, J. W. Kean, and J. a. Coe (2013), Field measurement of basal forces generated by erosive debris flows, *J. Geophys. Res. Earth Surf.*, *118*(2), 589–602, doi:10.1002/jgrf.20041.

Papa, M., S. Egashira, and T. Itoh (2004), Critical conditions of bed sediment entrainment due to debris flow, *Nat. Hazards Earth Syst. Sci.*, *4*(3), 469–474, doi:10.5194/nhess-4-469-2004.

Pierce, J. L., G. a Meyer, and a J. T. Jull (2004), Fire-induced erosion and millennial-scale climate change in northern ponderosa pine forests, *Nature*, *432*(November), 87–90, doi:10.1038/nature03028.Published.

Pouliquen, O. (1999), Scaling laws in granular flows down a rough plane, *Phys. Fluids*, *11*(3), 542–548, doi:10.1063/1.1416884.

Rickenmann, D., D. Weber, and B. Stepanov (2003), Erosion by debris flows in field and laboratory experiments, *Debris-Flow Hazards Mitig. Mech. Predict. Assess.*, 883–894.

Savage, S. B., and K. Hutter (1989), The motion of a finite mass of granular material down a rough incline, *J. Fluid Mech.*, *199*(-1), 177, doi:10.1017/S0022112089000340.

Stock, J. D., and W. E. Dietrich (2006), Erosion of steepland valleys by debris flows, *Bull. Geol. Soc. Am.*, *118*(9-10), 1125–1148, doi:10.1130/B25902.1.

Stoffel, M., and M. Beniston (2006), On the incidence of debris flows from the early Little Ice Age to a future greenhouse climate: A case study from the Swiss Alps, *Geophys. Res. Lett.*, *33*(16), 2–5, doi:10.1029/2006GL026805.

Tai, Y. C., and C. Y. Kuo (2008), A new model of granular flows over general topography with erosion and deposition, *Acta Mech.*, *199*(1-4), 71–96, doi:10.1007/s00707-007-0560-7.

Takagi, D., J. N. McElwaine, and H. E. Huppert (2011), Shallow granular flows, *Phys. Rev. E - Stat. Nonlinear, Soft Matter Phys.*, *83*(3), 1–10, doi:10.1103/PhysRevE.83.031306.

Takahashi, T. (2007), *Debris Flow: Mechanics, Prediction and Countermeasures, 2nd edition*, CRC Press.

Yohannes, B., L. Hsu, W. E. Dietrich, and K. M. Hill (2012), Boundary stresses due to impacts from dry granular flows, *J. Geophys. Res. Earth Surf.*, *117*(2), 1–21, doi:10.1029/2011JF002150.

Appendix

I. Definition of Symbols

θ = Angle of inclination

θ_n = Neutral angle

θ_R = Angle of repose

A_r = Aspect ratio

B = Breadth of flume

d = Particle diameter

$\dot{e}$ = Entrainment rate

$\dot{e}_c$ = Calculated entrainment rate

f = Solid fraction

g = Acceleration of gravity

h = Thickness of dense flowing layer

h_b = Height of a bin

h_c = Calculated normalized average thickness of a layer

H = Entrainment height/depth

H_o = Initial depth/position of bed

H_s = Height of supply

IP = Initial position

L = Thickness of a generic flowing section

$L_{erodible}$ = Length of erodible channel

L_{rough} = Length of rough channel

L_s = Length of supply

m_S = Mass of supply

m_o= Effluent mass

η = Porosity

ρ = Density of mixture

ρ_m = Density of material

s = Seconds

σ_R= Reynolds normal stress

S = Slope of bed

t = Time

T = Granular temperature

$\overline{T}$ = Average granular temperature

τ = Shear stress

τ_R = Reynolds stress

$\overline{\tau_R}$ = Average Reynolds stress

t_s = time when debris flow begins

u = Horizontal velocity

$\bar{u}_{dense}$ = Average horizontal velocity in the dense flowing layer

$\overline{u'u'}$ = Horizontal velocity fluctuations

$\overline{u'v'}$ = Tangential velocity fluctuations

v = Vertical velocity

V = Volume of supply

$\overline{v'v'}$ = Vertical velocity fluctuations

y = Vertical position